ABSTRACT

KANGARA MUDIYANSELAGE, JAYAMPATHI CHAMILA BANDARA. Atom Pairing in Optical Superlattices. (Under the direction of John Thomas).

This dissertation provides a complete study of two-atom pairing in a 1D optical superlattice potential. First, I describe the detailed derivation of a multi-band model to evaluate two-atom pairing energies and states in a 1D optical superlattice potential with finite radial confinement. Next, I provided the quantitative measurements of radio-frequency spectra of atom pair states in a 1D bichromatic optical superlattice that creates a series of double-well potentials, revealing the co-existance of two types of pairing states with different symmetries. I find the described multi-band model to be in excellent agreement with our observed spectral structure for different symmeteries of the double-well potential providing the first understanding of how elementary two-body pairng works in 1D optical superlattices.

Atom Pairing in Optical Superlattices

by

Jayampathi Chamila Bandara Kangara Mudiyanselage

A dissertation submitted to the Graduate Faculty of
North Carolina State University
in partial fulfillment of the
requirements for the Degree of
Doctor of Philosophy

Physics

Raleigh, North Carolina

2019

APPROVED BY:

Lubos Mitas	Dean Lee
Linyou Cao	John Thomas Chair of Advisory Committee

DEDICATION

To my parents.

BIOGRAPHY

Jayampathi Kangara was born on February 25, 1984 in Kurunegala, Sri Lanka. He attended St. Anne's College in Kurunegala and graduated in 2003. After entering University of Colombo in Colombo, Sri Lanka to pursue a degree in physics, he graduated in 2009. In 2010, he enrolled in a Master of Science degree program in physics at Miami University, Ohio. After graduating in 2012, he then enrolled in a PhD program at North Carolina State University in pursuit of a Doctor of Philosophy in Physics. He earned his PhD in physics in 2019.

ACKNOWLEDGEMENTS

First, I would like to thank my advisor Dr. John Thomas for his enormous support and supervision. Without his constant encouragement (especially during these last few months) this work would not have been possible. John is an outstanding physicist. But more importantly I admire him as a wonderful human being. His kind, caring nature and down to earth attitude have made my life as a PhD student certainly a very enjoyable one. John, I am forever grateful for everything you have done for me.

Next, I want to express my heartful gratitude to my post-doc Ilya. His knowledge about every piece of equipment in the lab always fascinates me. To him I owe everything I know about our lab. Ilya, I consider myself very fortunate to have worked with you for all these years. I also want to thank my senior student Chingyun for the enormous effort that she put into building the optical lattice setup and letting me take a part of it. The countless late nights we spent in the lab taking data, aligning the beams or sometimes even arguing about things while starving to death, will always be rememberd. Chingyun, the careful work you did in building and maintaining the optical lattice setup made my life an easier one as your successor.

Finally, I want to thank my junior student Saeed for his support given to me during the final days of my experiment. I admire your dedication and enthusiasm in the lab and thoroughly enjoyed my time working with you, teaching you and sometimes even learning from you.

TABLE OF CONTENTS

LIST OF FIGURES . . . . . **vii**

Chapter 1 Introduction **1**
1.1 Ultracold Atoms in Optical Superlattices. 2
1.2 Layered Systems 3
1.3 Thesis Overview 3

Chapter 2 Background **5**
2.1 Optical Dipole Traps 5
2.2 Optical Lattices 7
2.3 Review of Band Theory 8
2.4 Optical Superlattice Potential 10
2.5 Tunable Interactions 12

Chapter 3 Multi-Band Model **15**
3.1 Two Interacting Atoms in a 1D Optical Lattice 15
3.1.1 Green's Function Solution 17
3.1.2 Evaluating the Kernel $K_E(Z, Z')$ 19
3.1.3 Evaluating $M_{GG'}(E, Q)$ 22
3.1.4 Evaluating the Kernel $K_{E_0}^{s=0}(Z, Z')$ and matrix element $M_{GG'}^0(E_0, Q)$ . . . 23
3.2 Numerical Implementation 25
3.2.1 Positive Energy States 28
3.3 Two-Particle Wavefunction 30
3.3.1 Axial Probabilty Distribution 32
3.4 Transition Strengths 37

Chapter 4 Experimental Methods **40**
4.1 Preparation of the atomic sample 40
4.2 Bichromatic Optical Lattice 41
4.3 Lattice Loading 43
4.4 Lattice Beam Alignment 44
4.5 Lattice Depth Calibration 47
4.6 Relative Phase Calibration 47
4.7 Radio Frequency Spectroscopy 49

Chapter 5 Experimental Results and Comparison with Theory **52**
5.1 Finding Zero Phase 52
5.2 Measured RF Spectra for a Symmetric Double Well Potential 53
5.2.1 Evaluation of Spectra 54
5.3 Measured RF Spectra for an Asymmetric Double Well Potential 59
5.4 Tuning from a Double Well to a Single Well Potential 63

5.4.1 Q-dependence of the Spectra 64

Chapter 6 Conclusion 66
6.1 Summary of the Dissertation 66
6.2 Outook 66

References 68

Appendix 71
Appendix A Matlab Program for Evaluating
the Eigenstates and Energies in a Bichromatic Superlattice. 72
A.1 Evaluating Single Particle Band Energies 72
A.2 Evaluating Two Particle Energies 74
A.3 Evaluating $\left(\frac{d}{a}\right)_{ref}$ 78

LIST OF FIGURES

Figure 1.1 A 1D optical superlattice, formed by crossed 1064/532 nm laser beams, traps atoms along z-axis, while a 10.6 μm CO_2 laser provides radial confinement. Here d the period and ϕ the relative phase set by a Soleil-Babinet compensator (SB), which determines the separation $2\,b$ and a tilt 2Δ between the double-well minima. In the double-well potentials, atoms form two types of pairs with similar total energies, which can be thermally populated and probed by radio-frequency spectroscopy. 1

Figure 2.1 Potential created by a focused laser beam propagating in z direction. Here $V_0 = 2\pi\alpha I_0/c$. 6

Figure 2.2 Potential created by two counter propagating focused laser beams moving in z direction. 7

Figure 2.3 Energies of three lowest energy bands for different lattice depths. From left to right the depth varies as, $s = 2, 4, 8$. Note that all the energies are expressed in terms of the recoil energy, $E_R = \frac{\hbar^2 k^2}{2m}$ of the lattice beams with $k = \frac{\pi}{d}$. Lattice spacing is given by d. 9

Figure 2.4 Variation of the bichromatic lattice potential (solid black) with z for $\phi = 0$ (top figure) and for $\phi = \pi$ (bottom figure). $s_1 = 8$ (solid red) and $s_2 = 8$ (solid green). Note a double-well is created at $z = 0$ for $\phi = 0$ (top), and a single-well at $z = 0$ for $\phi = \pi$ (bottom). 10

Figure 2.5 Variation of energies of the three lowest energy bands of the bichromatic potential. (a) $s_1 = 7$, $s_2 = 0$, $\phi = 0$. (b) $s_1 = 7$, $s_2 = 3.5$, $\phi = \pi$. (a) $s_1 = 7$, $s_2 = 16.5$, $\phi = 0$. 11

Figure 2.6 Tuning of energy of the lowest six hyperfine states with an externally applied magnetic field. a_0 is the Bohr radius. 12

Figure 2.7 Variation of the s-wave scattering length in Bohr units (a_0 is the Bohr radius) of states $|1\rangle$ and $|2\rangle$ as a function of applied magnetic field, B. 13

Figure 3.1 Binding energy versus d/a for zero lattice depth. Curves for $\beta = \hbar\omega_\perp/E_R = 0.5$(upper) and $\beta = 0.01$(lower) . Black dots/diamonds: Full diagonalization of eq. 3.23 for $s = 0$ (see text). Solid curves: Exact integral, eq. 3.50. 25

Figure 3.2 Total energy, E of two interacting atoms relative to the energy of two noninteracting atoms in ground band for dirfferent interaction strengths quantified by d/a where d is the lattice spacing and a is the s-wave scattering length. The lowest two d/a solutions (Green dots: 1^{st} sol. & blue dots: 2^{nd} sol.) are shown here. Dashed black lines represent the energy asymptots (see text). Red dots represent the third d/a solution. 26

Figure 3.3 Binding energy versus d/a for different lattice depths: from top to bottom, $s_1 = 0, 5, 10, 20$ ($s_2 = 0$). 27

Figure 3.4 Green dots: Energy versus d/a for $s1 = 40$ with $\beta = \hbar\omega_\perp/E_R = 0.2$. Dashed lines: energy of two free particles in different radial states (equally spaced by $2\hbar\omega_\perp$ in E_R units).Note here $E = 0$ is taken as the total energy of two free particles in their ground bands with $q = 0$ and their ground radial harmonic oscillator states. 29
Figure 3.5 Expanded energy E versus d/a view of fig. 3.2 for $-0.05 < E < 0.25$. Horizontal black dashed lines are the energy asymptotes of two free particles in different q states in their ground band and ground radial harmonic oscillator states. Note that here 30
Figure 3.6 Value of $|A_{partial}|^2$ for different values of m_r^{max}. Calculation is done for a pair state with a total energy of $E = -2.37\,E_R$. Note that $\beta = 0.0166$, $s_1 = 8$, $s_2 = 16$. 32
Figure 3.7 CM probability density (solid line) in the axial direction of a pair with total energy, $E = -1.8$. Dashed line shows the lattice potential for a lattice of $s_1 = 8$ and $\beta = 0.0166$. 33
Figure 3.8 Total energy, E of two particles for a lattice of double-well potentials ($s_1 = 8$, $s_2 = 16$ and $\phi = 0$) versus d/a. A and B show the pairing states with $d/a = 1.28$. Note again that $E = 0$ reperent the energy of two free atoms in their graound band (at $q = 0$) and ground radial harmonic oscillator states. . 34
Figure 3.9 CM probability density in the axial direction of atom pair state A (Top/-Green) and B (Bottom/Blue). Dashed line shows the lattice potential for a lattice of $s_1 = 8$, $s_2 = 16$, $\phi = 0$ and $\beta = 0.0166$. 35
Figure 3.10 Relative probability density in the axial direction of atom pair state A (Top/-Green) and B (Bottom/Blue) of Fig. 3.8. Note the CM co-ordinate, $Z = 0.22$ for both states (see text) 35
Figure 3.11 CM probability density in the axial direction of atom pair state A (Top/-Green) and B (Bottom/Blue). Dashed line shows the lattice potential for a lattice of $s_1 = 8$, $s_2 = 16$, $\phi = \pi/8$ and $\beta = 0.0166$. 36
Figure 3.12 Relative probability density in the axial direction of atom pair state A (Top/-Green) and B (Bottom/Blue). For state A the CM coordinate, $Z = 0.2$ and for state B, $Z = -0.25$ (see text) 37
Figure 3.13 Solid Line: CM probability density in the axial direction of atom pair state A (Green) for $z = 0$ in Fig. 3.8 with $\phi = 0$. Magenta circles represents $|f^Q_{E_A}(Z)|^2$. 39
Figure 3.14 Solid Line: CM probability density in the axial direction of atom pair state A (Green) for $z = 0$ in Fig. 3.8 with $\phi = \pi/8$. Magenta circles represent $|f^Q_{E_A}(Z)|^2$. 39

Figure 4.1 Bichromatic optical lattice beam grnerator. $\simeq$5 W of power from 1064 nm beam (generated by a fiber laser) is frequency doubled using a second harmonic generator (SHG) to generate the 532 nm beam. The beams then go through phase-locked acousto optic modulators (AOM) and are coupled in to two high power fibers. At the output side close to the vacuum chamber, two beams are then combined on a dichroic combiner to co-propagate. After exiting the chamber, two beams are propagated through a Soleil-Babinet compensator, which controls the relative phase between the lattices. 42

Figure 4.2 Bichromatic optical lattice beam arrangement. Note that all three beams (CO_2, 1^{st} and 2^{nd} lattice beams) lie on the same plane. α and β are carefully measured experimentally [Cheng, 2016]. The angle between the two beams that make up the lattice is $\theta = \pi - (\alpha - \beta) = 91°$, which determines the lattice periods. 43
Figure 4.3 A typiclal timing sequence for the experiment. Solid purple, red and green curves shows the variation of the potential depth of the CO_2 laser beam trap, red lattice (denoted as 1064 nm) and the green lattice (denoted as 532 nm) consecutively. The bias magnetic field is also tuned from 834 G to a final field of interest (here to 800 G) to set the desired scattering lenght a. 20 ms radio frequency (RF) pulse is applied to probe tha binding energy of the atom pairs, prior to taking an absorbtion image using a 5 μs resonance optical pulse to measure the atom number in a chosen hyperfien state. 44
Figure 4.4 Lattice beam setup close to the vacuum chamber. RL1 and GL1 are the lenses that facus red and green beams into the vacuum chamber. Cam1 and Cam2 are used to align the red and green beams with each other. FL1 and FL2 denote flipper mirrors that can be flipped in and out of the beam path. . 45
Figure 4.5 Lattice beams and CMOS camera arrangement. The two CMOS cameras are used to take absorption image of the atom cloud in two orthogonal directions. The red arrow represents the 1^{st} lattice beam (refer back to Fig. 4.2). The blue arrow represents the propagation direction of the CO_2 laser beam. . . . 46
Figure 4.6 Construction of the Babinet compensator. E_1 and E_2 are two cross polarized optical fields. n_o and n_e are the refractive indices along the ordinary and extra-ordinary axes of the wedges and of the slab. Note that the top wedge can be translated perpendicular to the propagation direction of the optical fields (solid red line) to vary d using an attached micrometer actuator. d is the total thickness of the two wedges. 48
Figure 4.7 Left: RF transition between energy levels of a single component system. Right: Corrensponding spectra of state $|2\rangle$ atom loss as a function of the input RF frequency. ν_{32}^0 is the resonance frequency. 50
Figure 4.8 Left: RF transition between energy levels of an interacting system of $|1\rangle$ and $|2\rangle$. $E^1 2_b$ and $E^1 3_b$ are the binding energies of $|12\rangle$ and $|13\rangle$ atom pairs. Right: Corrensponding RF spectra with a shifted pairing peak at $\nu_{bb}^0 = E_b^{12} - E_b^{13}$. . 50

Figure 5.1 Radio-frequency $|12\rangle \rightarrow |13\rangle$ dimer transition spectra (black dots) versus predictions (red curves) for $B = 834.6$ G. Spectrum for (from left to right) $\phi = -2\pi/35$; $\phi = 0$; $\phi = +2\pi/35$. Error bars denote the standard deviation of the mean of 5 runs. 53
Figure 5.2 Radio-frequency $|12\rangle \rightarrow |13\rangle$ dimer transition spectra (blue dots). Here $s_1 = 7$, $s_2 = 16.5$ and $\phi = 0$. $\Delta\nu_{RF} = \nu_{RF} - \nu_{32}^0$ is the input radio frequency relative to the bare atomic frequency ν_{32}^0. Error bars denote the standard deviation of the mean of 5 runs. 54

Figure 5.3 Dimer energies E for a lattice of double-well potentials versus d/a for $\phi = 0$. For each E, green and blue denote the two smallest d/a values. A and B show the initially populated $|12\rangle$ dimer states with $d/a_{12} = 1.28$. Crossings with the dashed black line at $d/a_{13} = -3.78$ determine final $|13\rangle$ dimer states. The energy asymptotes, shown as red horizontal lines, denote the lowest energy for two noninteracting atoms in the first band (lower red line) and for one in each of the first two bands (upper red line). Insets show typical structure for states above $E = 0$. 55

Figure 5.4 (b) Eigenstates $f_E(Z)$ (see eq. 3.55) versus CM coordinate Z are A symmetric or B antisymmetric with respect to the site center. (a) Cartoons depict delocalized symmetric (A) orantisymmetric (B) dimer CM states. 56

Figure 5.5 (a) Energies of $|13\rangle$ final states for $\phi = 0$ are determined from the crossings of the energy versus d/a curves with the $d/a_{13} = -3.78$ vertical dashed black line. Panels (b) and (c) show the final state energies and corresponding Franck-Condon factors for transitions from the initial states A (green bars) and B (blue bars). Only the final states with Franck-Condon factors larger than 10^{-3} are shown. 57

Figure 5.6 (a) Calculated Franck-Condon factors (log scale) for symmetric double-well potentials, $\phi = 0$ as a function of transition frequency. (b) Radio-frequency $|12\rangle \rightarrow |13\rangle$ dimer transition spectra (black dots) versus predictions (red curves). Green and blue denote contributions from states A and B of Fig. 5.3. Error bars denote the standard deviation of the mean of 5 runs. 58

Figure 5.7 Dimer energies E for a lattice of tilted double-well potentials versus d/a for $\phi = \pi/35$. For each E, green and blue denote the two smallest d/a values. A and B show the initially populated $|12\rangle$ dimer states with $d/a_{12} = 1.28$. Crossings with the dashed black line at $d/a_{13} = -3.78$ determine final $|13\rangle$ dimer states. The energy asymptotes, shown as red horizontal lines, denote the lowest energy for two noninteracting atoms in the first band (lower red line) and for one in each of the first two bands (upper red line). Insets show typical structure for states above $E = 0$. 60

Figure 5.8 (a) Cartoons depict localized right (A) or left (B) dimer states. (b) Eigenstates $f_E(Z)$ (see eq. 3.55) versus CM coordinate Z are A symmetric or B antisymmetric with respect to the site center. 61

Figure 5.9 (a) Energies of $|13\rangle$ final states for $\phi = 0$ are determined from the crossings of the energy versus d/a curves with the $d/a_{13} = -3.78$ vertical dashed black line. Panels (b) and (c) show the final state energies and corresponding Franck-Condon factors for transitions from the initial states A (green bars) and B (blue bars). Only the final states with Franck-Condon factors larger than 10^{-3} are shown. 61

Figure 5.10 Bottom: Radio-frequency $|12\rangle \rightarrow |13\rangle$ dimer transition spectra (black dots) versus predictions (red curves). Green and blue denote contributions from states A and B of Fig. 5.7. Top: Calculated Franck-Condon factors (log scale) for symmetric double-well potentials, $\phi = 0$ as a function of transition frequency. Error bars denote the standard deviation of the mean of 5 runs. . . . 62

Figure 5.11 Radio-frequency $|12\rangle \rightarrow |13\rangle$ dimer transition spectra (black dots) versus predictions (red curves) for $B = 800.6$ G, $s_1 = 7$, $s_2 = 16.5$. Calculated Franck-Condon factors (log scale) versus transition frequency and spectrum for (a) $\phi = 0$; (b) $\phi = \pi/35$; (c) $\phi = 2\pi/35$. Error bars denote the standard deviation of the mean of 5 runs. 63
Figure 5.12 Spectra for $B = 800.6$ G calculated for $Q = 0$ only (blue) versus spectra for Boltzmann-factor-weighted sum over Q (red) compared to data (gray dots). (a) $\phi = 0$; (b) $\phi = \pi/35$. 64

Figure 6.1 Added Electro-optic modulator(EOM) allows the dynamical variation of the relaitve phase ϕ. Phase can be changed from symmetric dpuble-well to an asymmetric double-well potential by changing the voltage applied to the EOM. 67

Chapter 1

Introduction

In this dissertation I present the complete theory and experimental observations of pairing of interacting Fermions in a tunable 1D bichromatic optical superlattice potential with nonzero harmonic radial confinement. The bichromatic superlattice potential creates an array of periodic double well potentials, Fig. 1.1, and is created by combining on a beam splitter two optical fields of wavelengths $\lambda_1 = 1064$ nm and $\lambda_2 = 532$ nm, with the second field obtained by frequency doubling of the first. The combined beams are split into two beam pairs, which intersect at an angle $\theta = 91.0^o$ to create a fundamental lattice, denoted "red," with a period $d = 0.75\,\mu$m

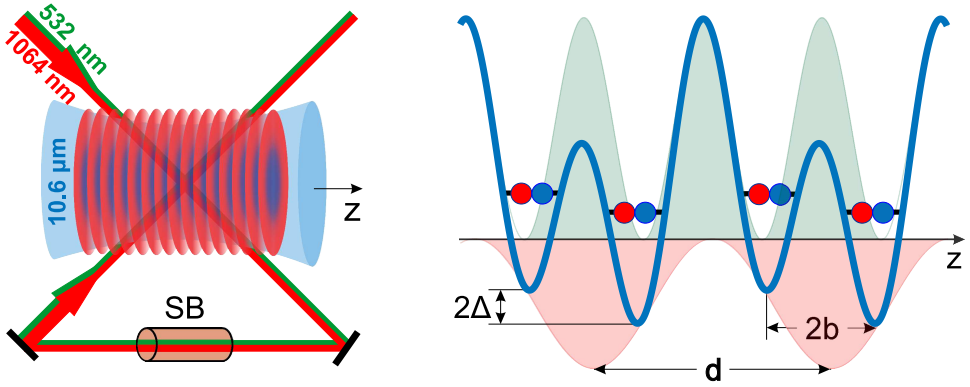

Figure 1.1: A 1D optical superlattice, formed by crossed 1064/532 nm laser beams, traps atoms along z-axis, while a 10.6 μm CO_2 laser provides radial confinement. Here d the period and ϕ the relative phase set by a Soleil-Babinet compensator (SB), which determines the separation $2\,b$ and a tilt 2Δ between the double-well minima. In the double-well potentials, atoms form two types of pairs with similar total energies, which can be thermally populated and probed by radio-frequency spectroscopy.

and a secondary lattice, denoted "green," with period $d/2$. The relative phase ϕ between the standing waves is manually tunable using a calibrated Soleil-Babinet compensator placed in the path of the second beam pair, to control the symmetry of the periodic double-well potential. An ultracold gas of fermionic atoms with tunable interations is loaded in to this superlattice potential confining the atoms in a series of bi-layered pancake like structure. A 50-50 mixture of the two lowest hyperfine states (denoted $|1\rangle$, $|2\rangle$) of fermionic ^{6}Li atoms is loaded in to the lattice. The trapped cloud is then magentically tuned near the broad collisional (Feshbach) resonance at 832.2 G [Bartenstein et al., 2005, Zürn et al., 2013] to control the s-wave scattering length a_{12}. Measured radio frequency spectra which probes the binding energy of atom pair states, exhibit a rich, relative-phase dependent structure. As the primary work of this thesis, observation of the co-existence of two types of atom pair states in a bichromatic superlattice potential is quantitatively explained using a multiband model, implemented by extending the rigorous Green's function method of Orso et al., [Orso et al., 2005] to a 1D superlattice with non-zero harmonic radial confinement.

1.1 Ultracold Atoms in Optical Superlattices.

Over many years ultracold quantum gases trapped in optical lattice potentials have become a perfect candidate to investigate and study the fundamental questions asked in many fields such as modern solid state physics, atomic and molecular and even in quantum information. Created by interfering two or more laser fields forming a periodically varying intensity pattern traps neutral atoms by means of optical dipole forces. These artificial crystals of light, used to mimic even most complicated crystal structures in condense matter physics, provide a wide control of internal parameters of the system which cannot be realized in a real solid state system. Optical superlattices, comprising two or more standing waves of light, provide an additional degree of freedom allowing one to control the dispersion of the trapped atoms.

Ground breaking experiments with bosonic atoms in superlattices have simulated Dirac dynamics, such as Klein tunneling [Salger et al., 2011, Witthaut et al., 2011], by producing linear dispersion. A relative phase near zero creates periodic, double-well potentials with controllable asymmetry. Single atoms in the right or left states of tilted double-well potentials have been employed to study non-equilibrium dynamics [Pertot et al., 2014] to provide an effective spin-orbit interaction with negligible optical scattering [Li et al., 2016]. This has enabled the observation of antiferromagnetic spin textures [Li et al., 2016]. Cyclic variation of the phase and corresponding double-well symmetry has been used to observe topological (Thouless) pumping for weakly interacting bosons [Lohse et al., 2016] and fermions [Nakajima et al., 2016].

1.2 Layered Systems

Among many possible optical lattice structures, one dimensional optical lattices have been of a particular interest among researchers in realizing low-dimensional quantum systems. Multicomponent atomic gases in two dimensional and quasi-two dimensional layered structures , have enabled the ability to create cold atomic analogs of several interaction driven condensed matter states such as excitonic Bose condensate [Butov et al., 2002, Seamons et al., 2009] observed in bilayer systems and zero-field magnetic phases [Weitz et al., 2010, Velasco et al., 2012, Mayorov et al., 2011] observed in bilayer graphene.

Fermi gas with magnetically tunable two-body interactions [O'Hara, 2002] loaded in to an one dimensional bichromatic lattice potential, Fig. 1.1, creates such multilayer atomic system, providing broad platform to study not only these exotic new states of matter, but also to study interesting many-body physics such as entanglement and nonequilibrium dynamics. However, to realize these rich variety of states and the physics behind them, it is important to understand and control the two-body interactions of the confined species in tunable lattice potentials. It has been predicted theoretically [Orso et al., 2005] and observed in experimentally [Sommer et al., 2012] that anharmonicity in optical lattice potentials generally entangles the center of mass and relative coordinates of confinement-induced atom pairs, modifying the pair binding energy. Also, geometric control of pairing interactions between species in separated layers, produced by a harmonic confinement with an applied spin-dependent force, has been observed recently in a bilayer system [Kanász-Nagy et al., 2015].

However, until now there has been no quantitative experimental study of the elementary atom pairing in optical superlattice structures. In this dissertation I provide a complete theoretical model and experimental observations, representing two-body pairing in such structures, created using a bichromatic optical lattice potential. I employ a spectroscopic techniques to experimentally study the two-body pairing states under different symmetry configurations of the superlattice potential and find that the measurements are in excellent agreement with the theoretical model, derived in this thesis.

1.3 Thesis Overview

In Chapter 2, I provide background information behind optical lattice and superlattice potentials. A brief overview of band theory is provided describing the band structures and how bands are tuned in optical superlattice potentials. An introduction to magnetically induced Feshbach resonance is also described as a way of controlling interactions between multi-component fermi gases confined in lattice potentials. Chapter 3 describes the theory behind two-atom pairing in a one dimensional optical superlattice potential, exploring the eigenvalues and eigenvectors of

these pair states. In Chapter 4, I discuss the methods, including the techniques used to calibrate the lattice parameters and also to probe the binding energies of atom pair states. A brief introduction to radio frequency spectroscopy is also provided in order for the reader to understand the experimental results described in the next chapter. In Chapter 5, a detailed discussion comparing experimental measurements with the theoretical model is provided, summarizing the dissertation.

Chapter 2

Background

In this chapter, I wish to give the reader an introduction on some of the basic theoretical concepts that will be useful for understanding the full theory discussed in Chapter 3. In the experiment, cold atoms are confined by means of optical dipole traps. So I will start by doing a brief introduction to optical dipole traps and move on to optical lattice potentials. Then I will do a brief overview of band theory, which describes the energy eigenstates for a single atom in a periodic optical dipole potential (i.e. optical lattice). Finally, the focus will be to tell the reader how interactions between atoms are controlled using a magnetically induced Feshbach resonance.

2.1 Optical Dipole Traps

When a neutral atom is placed in an electric field $\mathbf{E}$, the interaction creates an induced dipole moment $\mathbf{d} = \alpha\mathbf{E}$ in the atom, where α is the polarizability. Then the potential of the induced dipole moment is given by

$$V_{dip} = -\frac{1}{2}\mathbf{d}\cdot\mathbf{E}. \tag{2.1}$$

A semiclassical expression for the polarizability can easily be obtained by taking the atom as a two level system interacting with the classical electric field via a dipole interaction. Using time dependent perturbation theory, we find that,

$$\alpha = \alpha_s\left[\frac{1}{1-\omega^2/\omega_0^2}\right] \tag{2.2}$$

where ω_0 is the resonance frequency of two level atom and ω is the frequency of the driving field. Here $\alpha_s = 2\mu_{eg}^2/\hbar\omega_0$ is the static polarizability of the two level atom with μ_{eg} the dipole matrix element.

As the atoms cannot respond at the optical frequencies, eq. 2.1 can be time averaged, and

written in terms of the intensity of a focused gaussian beam,

$$V_{dip} = -\frac{2\pi\alpha I}{c} \tag{2.3}$$

where the intensity I is given by,

$$I = \frac{I_0}{1 + (z/z_0)^2}\, e^{-2r^2/w^2} \tag{2.4}$$

for a beam travelling in z direction. Here I_0 is the peak intensity, w is the $1/e^2$ intensity radius and $z_0 = \pi w^2/\lambda$ is the Rayleigh length of the focused beam with a wavelength λ. Note that experimentally $I_0 = 2P/\pi w^2$ with P being the measured power of the gaussian beam. For an atom placed in a focused laser field, the dipole force resulting from the interaction potential is $F_{dip} = -\nabla V_{dip}$. The sign of the force is then determined by the sign of the polarizability in eq. 2.2. For red detuned fields ($\omega >> \omega_0$) dipole force is inward and atom is attracted towards the regions with maximum intensity; For blue detuned fields, the force is outward, repelling the atom the from high intensity region. Figure 2.1 shows the potential felt by an atom in a red detuned focused laser beam trap.

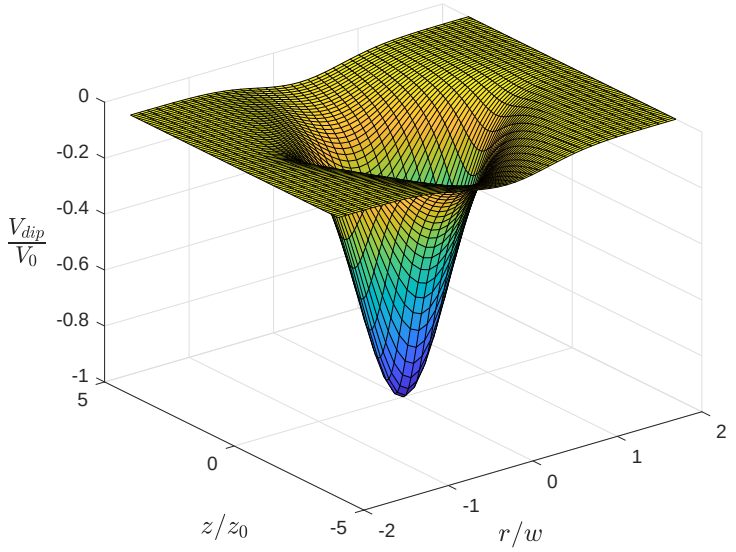

Figure 2.1: Potential created by a focused laser beam propagating in z direction. Here $V_0 = 2\pi\alpha I_0/c$.

2.2 Optical Lattices

Optical lattices are made of combining two counter propagating laser beams with linearly polarized electric fields creating a standing wave. The potential felt by an atom placed in a standing wave laser field created by two counter propagating beams of wavelength λ in the z direction is given by

$$V(z) = V_0 \cos^2(kz) \tag{2.5}$$

where $V_0 = 16\alpha P/c\,w^2$ with P, the measured power for the beam and $k = \pi/d$, where $d = \lambda/2$ is the lattice spacing. Here α is given by eq. 2.2. Note that this gives rise to a periodically varying potential. For red detuned beams, the atoms are trapped in the maximum intensity regions and for blue detuned beams, in the minima. Figure 2.2 shows the potential creadted by

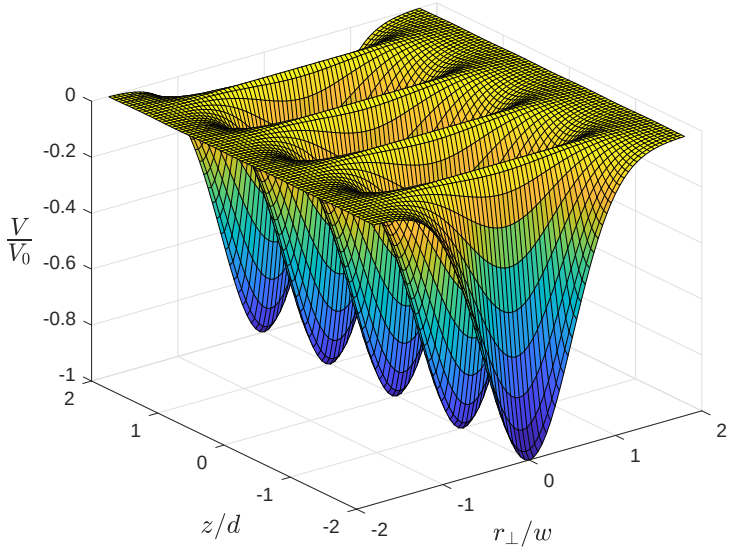

Figure 2.2: Potential created by two counter propagating focused laser beams moving in z direction.

two counter propagatin gaussian laser beams focused at $z = 0$, where the relevent potential is given by the following expression,

$$V(r_\perp, z) = -\frac{V_0}{1 + (z/z_0)^2}\, cos^2(kz)\, e^{-2r_\perp^2/w^2} \tag{2.6}$$

At the limit where $z << z_0$ we can neglect the slowly varying z dependence. This is true for our experiments since ultracold gases with a temperature, $T << V_0/k_B$, are confined to a small region near the focus of the gaussian beams. By applying the same argument, the exponential

variation can also be expanded for $r_\perp/w << 1$. The resulting potential is then approximately harmonic in $r_\perp$ and periodically varying in z,

$$V(r_\perp, z) \simeq \frac{1}{2} m\omega_\perp^2 r_\perp^2 + V_0\, cos^2(kz) \tag{2.7}$$

where $\omega_\perp = \sqrt{4V_0/mw^2}$ is the atom harmonic oscillation frequency in the radial direction with m, the mass of the trapped atom.

By increasing the number of beam pairs interfered in space one can also realize higher dimensional optical lattice potentials. For the purpose of discussion throughout this thesis, let me rewrite the periodic part of the potential in eq. 2.7 as $V(z) = sE_R \cos^2(kz)$ with s describing the intensity of the laser beams and here $E_R = \frac{\hbar k^2}{2m}$ is the recoil energy. This can be then expressed as

$$V(z) = sE_R/2[1 + \cos(2kz)]. \tag{2.8}$$

By eliminating the constant term finally the potential is,

$$V(z) = \frac{sE_R}{2} \cos(2kz). \tag{2.9}$$

From now on, this will always be the form used to represent a periodic lattice potenial.

2.3 Review of Band Theory

Next, I will do a brief review of single particle band theory. The goal here is to introduce the energy eigenvalues and eigenvectors for a single particle placed in a periodic potential. Let us now assume a 1D periodic potential given by eq. 2.9. The Shrödinger equation for this problem can be written as,

$$\left[-\frac{\hbar^2}{2m}\frac{\partial^2}{\partial z^2} + V(z)\right] \psi_q^\alpha(z) = E^\alpha(q)\, \psi_q^\alpha(z), \tag{2.10}$$

where α is the band index and q denotes the quasi-momentum for the first Brillouin zone, $-\pi/d \leq q \leq \pi/d$. Note that the potential $V(z) = sE_R cos^2(kz)$ here is given by 2.7 without the term that depends on $r_\perp$. The eigenstates are given by

$$\psi_q^\alpha(z) = \sum_G C_G^\alpha(q) \frac{e^{i(q+G)z}}{\sqrt{Nd}}, \tag{2.11}$$

where $G = (0, \pm 1, \pm 2, ...)\, G_0$ with $G_0 = \pi/d$ being the fundamental reciprocal lattice vector and N is the number of lattice sites taken into account. Note the states are complete on the lattice interval $0 \leq z \leq Nd$,

$$\sum_{\alpha,q} \psi_q^{\alpha}(z)\psi_q^{\alpha*}(z') = \delta(z - z'). \tag{2.12}$$

Eq. 2.10 can be solved numerically to get the energy eigen values $E^{\alpha}(q)$ and coefficents $C_G^{\alpha}(q)$. A full treatment for this problem is given in ref. [Cheng, 2016]. As a reminder, let me show the reduced zone energy band diagram for three different lattice depths. Here the total energy is given as a function of the quasi-momentum of the particle. When lattice depth is relatively small energy distribution resembles the energies of a free particle. For a finite lattice depth the energies exhibit gaps between different the energy bands. As the depth increases further the energy bands become more flat, like the energy level diagram one would expect for a simple harmonic oscillator, where the particle is trapped in a deep potential well.

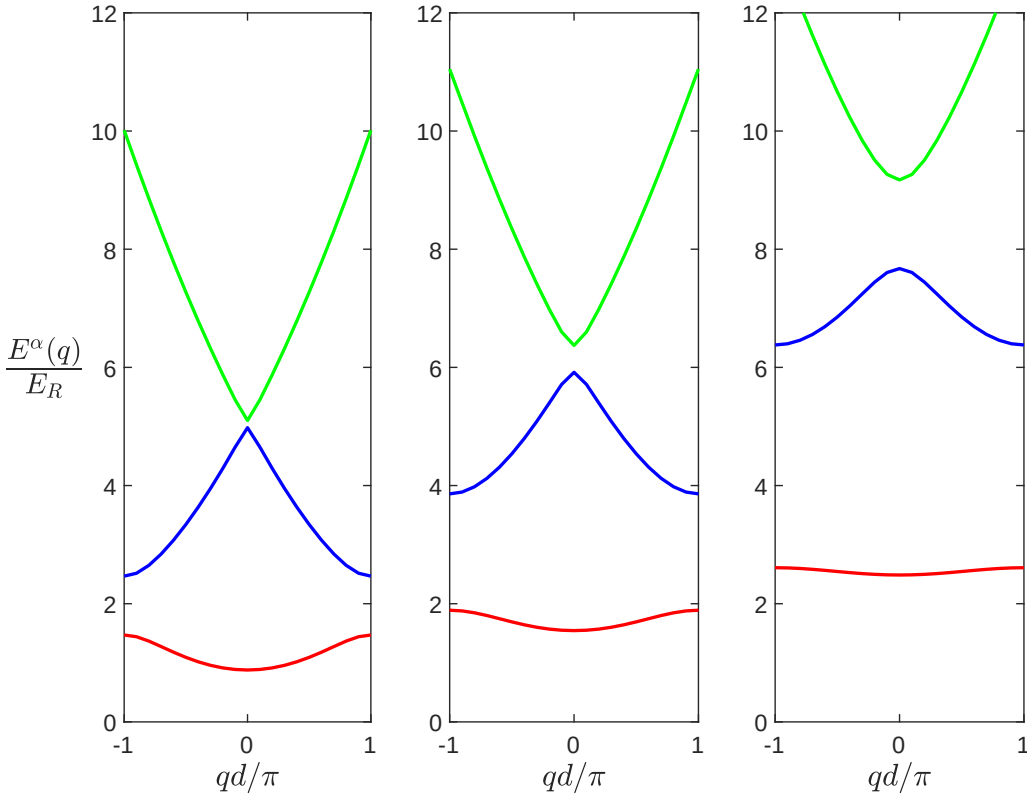

Figure 2.3: Energies of three lowest energy bands for different lattice depths. From left to right the depth varies as, $s = 2, 4, 8$. Note that all the energies are expressed in terms of the recoil energy, $E_R = \frac{\hbar^2 k^2}{2m}$ of the lattice beams with $k = \frac{\pi}{d}$. Lattice spacing is given by d.

2.4 Optical Superlattice Potential

Optical superlattice potentials are created by combining two or more optical standing waves. For our experiment, I consider the simplest form of superlattice potential, which is called a bichromatic superlattice. As the name implies, a bichromatic superlattice is created by combing two optical fields with a primary attractive lattice, denoted "red" and a secondary repulsive lattice, denoted "green". Taking the red lattice to be the fundamental and $V_{red}(z) = -s_1 E_R \cos^2(kz)$ with $k = \pi/d$, where $d = \lambda/2$ is the lattice spacing, the bichromatic potential can be written as,

$$V(z) = -\frac{s_1 E_R}{2}\cos(2kz) + \frac{s_2 E_R}{2}\cos^2(4kz + \phi). \tag{2.13}$$

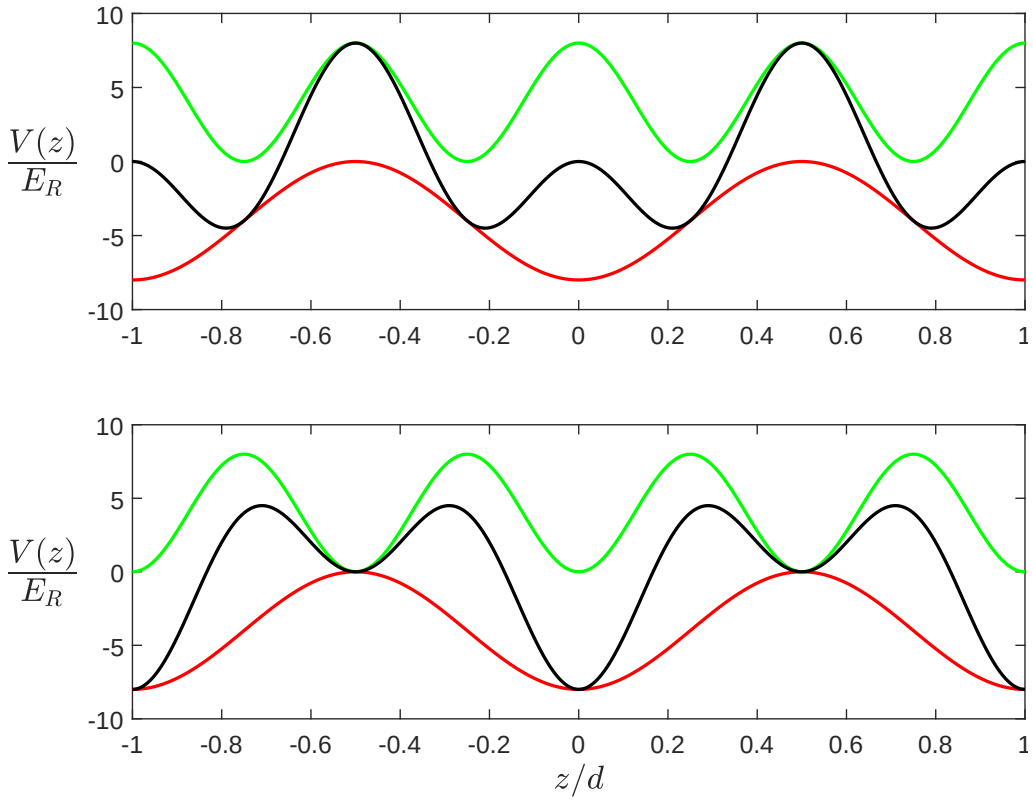

Figure 2.4: Variation of the bichromatic lattice potential (solid black) with z for $\phi = 0$ (top figure) and for $\phi = \pi$ (bottom figure). $s_1 = 8$ (solid red) and $s_2 = 8$ (solid green). Note a double-well is created at $z = 0$ for $\phi = 0$ (top), and a single-well at $z = 0$ for $\phi = \pi$ (bottom).

In fig. 2.4, bichromatic potential (solid black line) for $s_1 = 8$ and $s_2 = 8$ is shown for two

different phases. When $\phi = 0$, the net potential is a series of double wells while a series of single wells are generated for $\phi = \pi$.

Energy eigenvalues and eigenvectors for an atom in this potential can also be calculated using eq. 2.10. To give the reader an idea about how the energy band diagram changes with the addition of a secondary potential, here I plot the energy eigenvalues of the first three energy bands for a few different combinations of lattice depths and phases. By looking at the figure, the reader can see that optical superlattice potential provides a wide control of the band structure of a trapped atom.

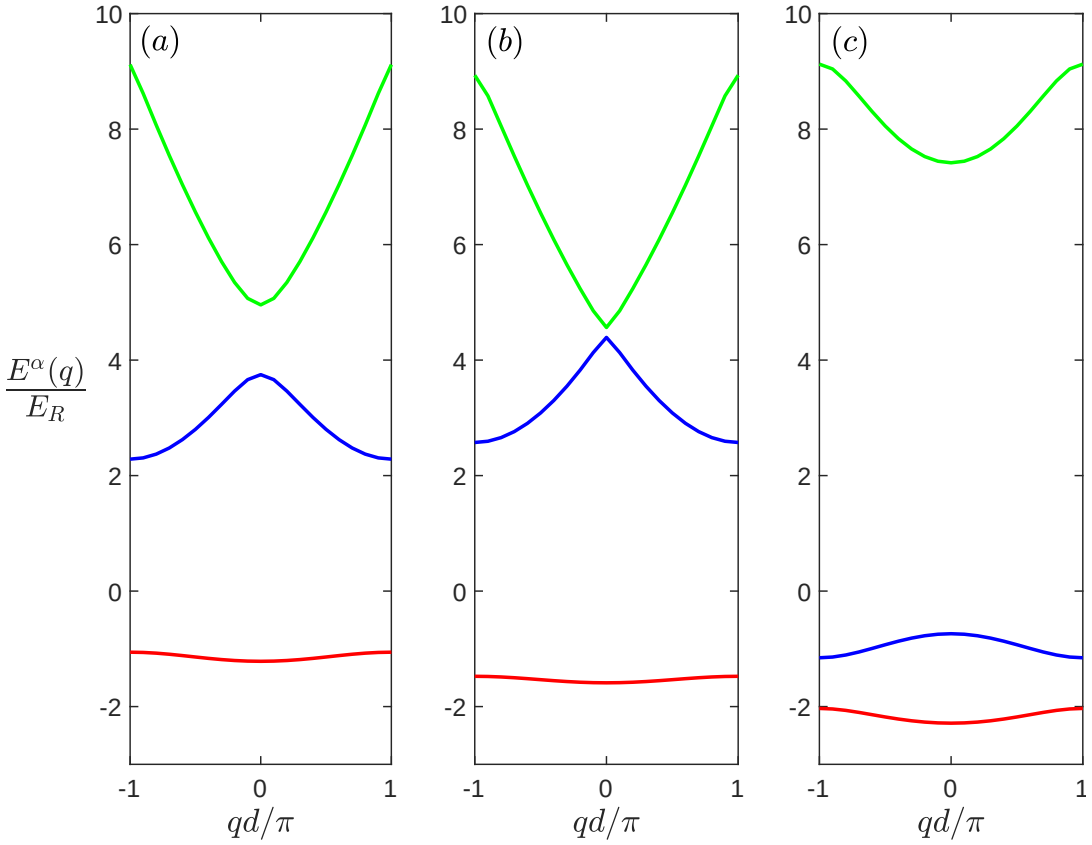

Figure 2.5: Variation of energies of the three lowest energy bands of the bichromatic potential. (a) $s_1 = 7$, $s_2 = 0$, $\phi = 0$. (b) $s_1 = 7$, $s_2 = 3.5$, $\phi = \pi$. (a) $s_1 = 7$, $s_2 = 16.5$, $\phi = 0$.

2.5 Tunable Interactions

Here in this dissertation, the interest is to see how the above mentioned energy level diagrams are modified by interactions between atoms. If two atoms are considered the interaction between them can be characterized by their s-wave scattering length, a. By controlling a, we can control the strength of interactions between the two atoms. Experimentally this is achieved by making use of a magnetically induced collisional Feshbach resonance, which occurs for two atoms in a bias magnetic field.

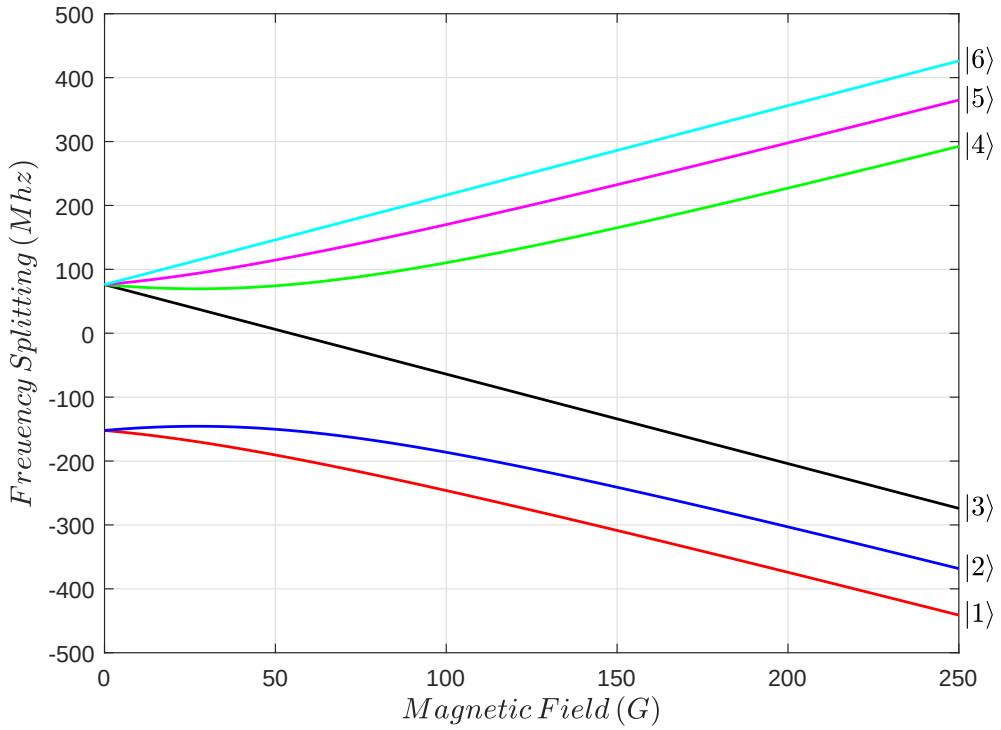

Figure 2.6: Tuning of energy of the lowest six hyperfine states with an externally applied magnetic field. a_0 is the Bohr radius.

In our experiment, we trap and cool a gas of ^{6}Li fermions to quantum degeneracy. This particular isotope of Li consists of 3 neutrons, 3 protons and 3 electrons, with a valence electron in the $2S$ orbit. The angular momentum quantum number, L for this electron is zero with a spin of $S = 1/2$. ^{6}Li has a nuclear spin $I = 1$. Hence, the total angular momentum quantum number F can be either $1/2$ or $3/2$, making the ground state to be six-fold degenerate. The interaction between the electron and the nuclear magnetic moments as well as an externally applied magnetic field, breaks this degenracy and results in six distinct eigenstates for the

ground electronic state of ^{6}Li. The reader can refer to previous theses from our group to see the full derivation of these lowest six eigenstates. These eigenstates are usually labled as $|1\rangle$, $|2\rangle$ and so on, starting from the lowest eigen state. Figure 2.6 shows how the energy of these six lowest eigenstates tunes with an externally applied magnetic field. When two ^{6}Li atoms collide with each other their scattering length is determined by their molecular potentials. For s-wave scattering, which is dominent at low temperatures the interaction is approximated by a contact pseudopotential, takes the following format [Huang, 1987],

$$V(\mathbf{r})\Psi(\mathbf{r}) = \frac{4\pi\hbar^2 a}{m}\delta(\mathbf{r})\frac{\partial}{\partial r}[r\Psi(\mathbf{r})]. \tag{2.14}$$

Here $\mathbf{r} = \mathbf{r_1} - \mathbf{r_2}$ is the relative position between the two colliding atoms, and a is the scattering length. Since Pauli exclusion principle prevents identical ^{6}Li fermions from interacting with each other, in the experiment, we trap a mixture of atoms in the two lowest hyperfine states $|1\rangle$ and $|2\rangle$ (see Fig 2.6).When two atoms collide, one from each of these states, they approach each other the via either a triplet or a singlet molecular potential. For the triplet potential the valence

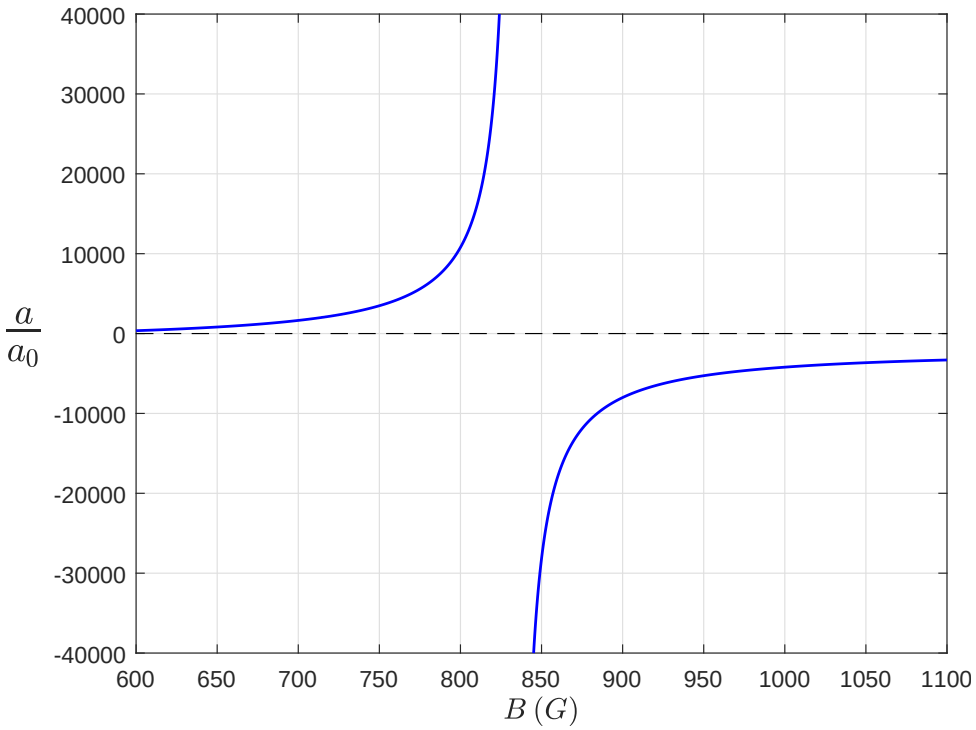

Figure 2.7: Variation of the s-wave scattering length in Bohr units (a_0 is the Bohr radius) of states $|1\rangle$ and $|2\rangle$ as a function of applied magnetic field, B.

electrons of the atoms combined to from a triplet spin state with total spin $S_{total} = S_1 + S_2$ is equal to one where as for the singlet potential the total spin becomes zero ($S_{total} = 0$).

It can be shown that at a high enough magnetic field, the pair of atoms in the lowest two states, $|1\rangle$ and $|2\rangle$, is approximately in a triplet state with spins aligned parallel hence the energy of the two atom state is tunable by an applied magnetic field. The spins of the singlet state are anti-parallel and the tunability of the energy is negligible. Feshbach resonance occurs when the energy of the two colliding atoms in the triplet state is to be degenerates with a bound molecular state in the singlet molecular potential. The two dominant resonances between states $|1\rangle$ and $|2\rangle$ occurs near 549 G (narrow) and 834 G (broad). For our experiment we exploit the broad resonance to tune the interaction between the two colliding atoms. Scattering length a near 834 G resonance is approximately,

$$a = a_{bg}\Big(1 - \frac{\Delta_B}{B - B_0}\Big) \tag{2.15}$$

where $a_{bg} = -1405\, a_0$, $B_0 = 834.149\, G$ and $\Delta_B = 300\, G$. Figure 2.7 shows how scattering length, a changes near the resonance.

Chapter 3

Multi-Band Model

In Chapter 2, I calculated the energies of a single atom placed in a one dimensional lattice potential. In this chapter, I focus on the case of two interacting atoms in one dimensional optical lattice and superlattice potentials. Our model is based on the Green's function method described in [Orso et al., 2005], which treated the 1D lattice with no radial confinement. In this model we include a finite radial confinement arising from the focused lattice beams and solve the two particle Shrodinger equation to obtain the energy eigenvalues and their corresponding eignevectors.

3.1 Two Interacting Atoms in a 1D Optical Lattice

To determine the eigenstates and binding energies for two atoms in a 1D bichromatic optical lattice with nonzero radial confinement, the required dimer wavefunctions are the bound state solutions of the two-atom Schrödinger equation

$$H\Psi(\mathbf{R},\mathbf{r}) = E_{tot}\Psi(\mathbf{R},\mathbf{r}), \tag{3.1}$$

where $\mathbf{R} = (\mathbf{r}_1 + \mathbf{r}_2)/2$ is the position of the center of mass (CM), $\mathbf{r} = \mathbf{r}_1 - \mathbf{r}_2$ is the relative coordinate and E_{tot} is the total CM and binding energy of the dimer.

The Hamiltonian is given by

$$H(\mathbf{R},\mathbf{r}) = H_0(\mathbf{R},\mathbf{r}) + g\,\delta(\mathbf{r})\frac{\partial}{\partial r}[r...], \tag{3.2}$$

where H_0 is the Hamiltonian for two noninteracting atoms in the optical potential and $g \equiv 4\pi\hbar^2 a/m$ determines the strength of the s-wave pseudo-potential [Huang, 1987], with m the atom mass and a the zero-energy scattering length. Here we have assumed that the effective range is negligible, as is the case for ^{6}Li near the broad Feshbach resonances.

For a single atom, the trapping potential energy is taken to be

$$V(x_1, y_1, z_1) = V_\perp(x_1, y_1) + V(z_1). \tag{3.3}$$

We assume that the radial confining potential energy is harmonic and cylindrically symmetric, $V_\perp(x_1, y_1) = \frac{1}{2}m\omega_\perp^2(x_1^2 + y_1^2)$.

The axial potential energy $V(z_1)$ in the bichromatic lattice arises from two optical standing waves, a primary attractive lattice denoted "red" and a secondary repulsive lattice, denoted "green," as described in sec. 2.4 in Chap. 2. For the red standing wave, the periodic potential is $V_{red}(z_1) = -s_1\, E_R\, \cos^2(kz_1)$, where $E_R = \hbar^2k^2/(2m)$ is the recoil energy, with $k = 2\pi/\lambda$ the optical wavevector. Here, $\lambda = \lambda_{red}/\sin(\theta/2)$ is the effective wavelength for two beams that intersect at an angle θ. Taking the red lattice as the fundamental, $k = \pi/d$, where $d = \lambda/2$ is the lattice spacing. The green lattice beams copropagate with the red beams and are created by frequency doubling of a portion of the red laser intensity. Hence, the effective wavelength for the green standing wave is precisely $\lambda/2$ and $V_{green}(z_1) = s_2\, E_R\, \cos^2(2kz_1 + \phi/2)$. The bichromatic lattice potential for one atom is then

$$V(z_1) = -\frac{s_1 E_R}{2}\, \cos(G_0 z_1) + \frac{s_2 E_R}{2}\, \cos(2\, G_0 z_1 + \phi), \tag{3.4}$$

where we have defined the fundamental reciprocal lattice vector $G_0 = 2k = 2\pi/d$ and eliminated the spatially constant terms. In the experiments, the stable relative phase ϕ between the green and red standing wave intensities is adjusted using a Soleil-Babinet compensator for static control, calibrated as described in Chapter 4.

As introduced back in Chapter 2 we define the single particle Bloch states, which are determined from the 1D Schrödinger equation,

$$\left[-\frac{\hbar^2}{2m}\frac{\partial^2}{\partial z_1^2} + V(z_1)\right]\psi_{q_1}^{\alpha_1}(z_1) = E^{\alpha_1}(q_1)\,\psi_{q_1}^{\alpha_1}(z_1), \tag{3.5}$$

where α_1 denotes the band and q_1 denotes the quasi-momentum, $-\pi/d \le q_1 \le \pi/d$ for the first Brillouin zone. The eigenstates are given by

$$\psi_{q_1}^{\alpha_1}(z_1) = \sum_{G_1} C_{G_1}^{\alpha_1}(q_1)\frac{e^{i(q_1+G_1)z_1}}{\sqrt{Nd}}, \tag{3.6}$$

where $G_1 = (0, \pm1, \pm2, ...)\, G_0$ is a reciprocal lattice vector and N is the number of lattice sites. The states are complete on the lattice interval $0 \le z_1 \le Nd$,

$$\sum_{\alpha_1, q_1} \psi_{q_1}^{\alpha_1}(z_1)\psi_{q_1}^{\alpha_1 *}(z_1') = \delta(z_1 - z_1'). \tag{3.7}$$

For two atoms, the total lattice potential is

$$U(z_1, z_2) = V(z_1) + V(z_2) = V(Z + z/2) + V(Z - z/2) \equiv U(Z, z). \tag{3.8}$$

As noted in ref. [Orso et al., 2005], we see that the CM Z and relative z coordinates are generally entangled by the lattice potential.

With a harmonic radial potential, for two atoms of equal mass, the CM X, Y and relative x, y motions are separable, i.e., with $M = 2m$ the dimer total mass and $\mu = m/2$ the reduced mass,

$$U_\perp(\rho_1, \rho_2) \to U_\perp(R_\perp, r_\perp) = \frac{M\omega_\perp^2}{2}(X^2 + Y^2) + \frac{\mu\omega_\perp^2}{2}(x^2 + y^2), \tag{3.9}$$

Hence, we can take

$$\Psi(\mathbf{R}, \mathbf{r}) = \Phi_{CM}(X, Y)\, \Psi(\mathbf{r}, Z), \tag{3.10}$$

where $\Phi_{CM}(X, Y)$ is just the harmonic oscillator state of the CM in the X-Y plane,

$$\left[-\frac{\hbar^2}{2M}\left(\frac{\partial^2}{\partial X^2} + \frac{\partial^2}{\partial Y^2}\right) + \frac{M\omega_\perp^2}{2}(X^2 + Y^2)\right] \Phi_{CM}(X, Y) = E_{CM}^\perp \Phi_{CM}(X, Y). \tag{3.11}$$

As the orthornormal CM states $\Phi_{CM}(X, Y)$ factor out, are not coupled by the interaction, and do not change in radio frequency transitions, we will not consider them further.

The nontrivial part of the wavefunction entangles $\mathbf{r}$ and Z, and satisfies

$$\left[H^0(\mathbf{r}, Z) - E\right] \Psi(\mathbf{r}, Z) = -g\, \delta(\mathbf{r}) \frac{\partial}{\partial r} \left[r \Psi(\mathbf{r}, Z)\right], \tag{3.12}$$

where we have defined the total energy in eq. 3.1 to be $E_{tot} = E_{CM}^\perp + E$ and

$$H^0(\mathbf{r}, Z) = -\frac{\hbar^2}{2\mu}\nabla_{r_\perp}^2 + \frac{1}{2}\mu\omega_\perp^2 r_\perp^2 - \frac{\hbar^2}{2\mu}\frac{\partial^2}{\partial z^2} - \frac{\hbar^2}{2M}\frac{\partial^2}{\partial Z^2} + U(Z, z), \tag{3.13}$$

with $r_\perp^2 = x^2 + y^2$.

3.1.1 Green's Function Solution

Following ref. [Orso et al., 2005], we solve eq. 3.12 using a Green's function method, with

$$\left[H^0(\mathbf{r}, Z) - E\right] G_E(\mathbf{r}, Z; \mathbf{r}', Z') = -\delta(\mathbf{r} - \mathbf{r}')\delta(Z - Z'). \tag{3.14}$$

The formal solution to eq. 3.12 for a state of energy E is then

$$\Psi_E(\mathbf{r}, Z) = \psi_E^0(\mathbf{r}, Z) + g \int dZ' \int d^3\mathbf{r}' G_E(\mathbf{r}, Z; \mathbf{r}', Z')\, \delta(\mathbf{r}') \frac{\partial}{\partial r'} \left[r' \Psi_E(\mathbf{r}', Z')\right], \tag{3.15}$$

where the homogeneous solution obeys $\left[H^0(\mathbf{r},Z)-E\right]\psi_E^0(\mathbf{r},Z)=0$.

The Green's function is given in terms of a complete set of homogenous solutions satisfying $H^0(\mathbf{r},Z)\psi_\alpha(\mathbf{r},Z)=E_\alpha\,\psi_\alpha(\mathbf{r},Z)$,

$$\sum_\alpha \psi_\alpha(\mathbf{r},Z)\psi_\alpha^*(\mathbf{r}',Z')=\delta(\mathbf{r}-\mathbf{r}')\delta(Z-Z'). \tag{3.16}$$

Then,

$$G_E(\mathbf{r},Z;\mathbf{r}',Z')=\sum_\alpha \frac{\psi_\alpha(\mathbf{r},Z)\psi_\alpha^*(\mathbf{r}',Z')}{E-E_\alpha+i0^+} \tag{3.17}$$

satisfies eq. 3.14.

We are interested in the bound state solutions of eq. 3.12. In this case, the homogeneous solution in eq. 3.15 is not needed and

$$\Psi_E(\mathbf{r},Z)=g\int dZ'\,G_E(\mathbf{r},Z;0,Z')\,\frac{\partial}{\partial r'}\left[r'\Psi_E(\mathbf{r}',Z')\right]_{r'\to 0}. \tag{3.18}$$

To solve eq. 3.18, we define

$$f_E(Z)=\frac{\partial}{\partial r}\left[r\Psi_E(\mathbf{r},Z)\right]_{r\to 0}. \tag{3.19}$$

Applying $g^{-1}\partial_r[r...]_{r\to 0}$ to the left hand side of eq. 3.18 and using eq. 3.19, we obtain an integral eigenvalue equation as in ref. [Orso et al., 2005],

$$\frac{1}{g}f_E(Z)=\int dZ' K_E(Z,Z')\,f_E(Z'). \tag{3.20}$$

Here, the kernel is given by

$$K_E(Z,Z')=\frac{\partial}{\partial r}\left[r\,G_E(\mathbf{r},Z;0,Z')\right]_{r\to 0}. \tag{3.21}$$

As the lattice potential energy $U(Z,z)$ is periodic in Z, the normalized eigenstates, eq. 3.19, can be assumed to take the Bloch form,

$$f_E^Q(Z)=\sum_{G'} B_{G'}^E(Q)\,\frac{e^{i(G'+Q)Z}}{\sqrt{Nd}}, \tag{3.22}$$

where G' is a reciprocal lattice vector and Q is the total (CM) quasi-momentum, which is conserved.

Projecting eq. 3.20 with $g=4\pi\hbar^2 a/m$ onto the the orthonormal basis, $e^{i(G+Q)Z}/\sqrt{Nd}$, and

using eq. 3.22, we obtain the matrix eigenvalue equation

$$\frac{d}{a}B^E_G(Q) = \sum_{G'} M_{GG'}(E,Q)\, B^E_{G'}(Q), \tag{3.23}$$

which is diagonal in Q. Here,

$$M_{GG'}(E,Q) = \frac{4\pi\hbar^2}{m\,N}\int dZ \int dZ'\, e^{-i(G+Q)Z+i(G'+Q)Z'}\, K_E(Z,Z'). \tag{3.24}$$

3.1.2 Evaluating the Kernel $K_E(Z,Z')$

To proceed further, we need to evaluate the kernel $K_E(Z,Z')$ in eq. 3.21. As pointed out in ref. [Orso et al., 2005], this is not trivial, since the Green's function diverges as $1/r$ at short distance, due to the contact form of the two-body interaction. Following ref. [Orso et al., 2005], to evaluate the kernel, we exploit the fact that the operator $\partial_r[r...]$ projects out the regular part of G_E at $r \to 0$, since $\partial_r[r/r] = 0$, so that the kernel is finite.

Consider first the kernel for an energy E and a finite depth bichromatic lattice. We denote the lattice parameters by $s \equiv \{s_1, s_2, \phi\}$, and write

$$K^s_E(Z,Z') = \frac{\partial}{\partial r}\left[r\, G^s_E(\mathbf{r},Z;0,Z')\right]_{r\to 0}. \tag{3.25}$$

Subtracting the kernel for any other set of parameters s_0 and energy E_0 yields

$$K^s_E(Z,Z') - K^{s_0}_{E_0}(Z,Z') = \frac{\partial}{\partial r}\left\{r\left[G^s_E(\mathbf{r},Z;0,Z') - G^{s_0}_{E_0}(\mathbf{r},Z;0,Z')\right]\right\}_{r\to 0}. \tag{3.26}$$

As both Green's functions diverge as $1/r$ as $r \to 0$, the difference of the two Green's functions is regular as $r \to 0$. Hence, $\partial_r\{r[G^s_E - G^{s_0}_{E_0}]\} = r\partial_r(G^s_E - G^{s_0}_{E_0}) + \partial_r[r]\,(G^s_E - G^{s_0}_{E_0}) \to G^s_E - G^{s_0}_{E_0}$ as $r \to 0$. Then, we can write formally

$$K^s_E(Z,Z') = G^s_E(0,Z;0,Z') - G^{s_0}_{E_0}(0,Z;0,Z') + K^{s_0}_{E_0}(Z,Z'), \tag{3.27}$$

where $K^{s_0}_{E_0}$ corresponds to $G^{s_0}_{E_0}$. As shown below, the evaluation is carried out so that difference of the Green's functions is manifestly finite as $r, r' \to 0$.

An important feature of eq. 3.27 is that the kernel $K^s_E(Z,Z')$ is *independent* of the choice of the lattice parameters s_0 and the energy E_0. The evaluation is simplified by following ref. [Orso et al., 2005], and choosing s_0 to correspond to a zero depth lattice, where both the Green's function $G^{s_0=0}_{E_0}(0,Z;0,Z')$ and the kernel $K^{s_0=0}_{E_0}(Z,Z')$ are easily determined, as discussed further below.

We evaluate eq. 3.17 for G_E, using the complete set of separable eigenstates of the Hamil-

tonian of eq. 3.13,

$$\psi_\alpha(\mathbf{r}, Z) = \chi(r_\perp)\,\psi(z, Z). \tag{3.28}$$

The radial state satisfies

$$\left[-\frac{\hbar^2}{2\mu}\nabla^2_{r_\perp} + \frac{1}{2}\mu\omega_\perp^2 r_\perp^2\right]\chi(r_\perp) = E_\perp\,\chi(r_\perp), \tag{3.29}$$

with the general orthonormal solutions

$$\chi^l_{n_\perp}(r_\perp, \phi) = e^{il\phi}\sqrt{\frac{n_\perp!}{(n_\perp + |l|)!}}\,\frac{e^{-\frac{r_\perp^2}{4l_\perp^2}}}{\sqrt{2\pi l_\perp^2}}\left(\frac{r_\perp}{l_\perp\sqrt{2}}\right)^{|l|} L^{|l|}_{n_\perp}\!\left(\frac{r_\perp^2}{2\,l_\perp^2}\right), \tag{3.30}$$

where $L^{|l|}_{n_\perp}(\rho)$ is an associated Laguerre polynomial, $l_\perp = \sqrt{\hbar/(m\omega_\perp)}$ is the harmonic oscillator length for one atom, and

$$E^l_{n_\perp} = (2n_\perp + |l| + 1)\hbar\omega_\perp. \tag{3.31}$$

As $r_\perp, r'_\perp \to 0$ in determining the kernels, only the $l = 0$ states contribute. Defining $n_\perp = m_r$ as the radial quantum number, we take

$$\chi(r_\perp) \to \chi_{m_r}(r_\perp) = \frac{e^{-\frac{r_\perp^2}{4l_\perp^2}}}{\sqrt{2\pi l_\perp^2}}\,L^0_{m_r}\!\left(\frac{r_\perp^2}{2\,l_\perp^2}\right), \tag{3.32}$$

with $E^0_{m_r} = (2m_r + 1)\hbar\omega_\perp$. Here, the Laguerre polynomial is

$$L^0_{m_r}(\rho) = \sum_{k=0}^{m_r}\frac{(-\rho)^k\,m_r!}{(k!)^2(m_r - k)!} \tag{3.33}$$

so that $L^0_{m_r}(0) = 1$ is independent of m_r. These $l = 0$ solutions are normalized so that

$$\int_0^\infty 2\pi\,r_\perp dr_\perp\,\chi^*_{m'_r}(r_\perp)\chi_{m_r}(r_\perp) = \delta_{m'_r, m_r}. \tag{3.34}$$

For the axial part of the solution $\psi(z, Z)$, we recall that

$$-\frac{\hbar^2}{2\mu}\frac{\partial^2}{\partial z^2} - \frac{\hbar^2}{2M}\frac{\partial^2}{\partial Z^2} + U(Z, z) = -\frac{\hbar^2}{2m}\frac{\partial^2}{\partial z_1^2} + V(z_1) - \frac{\hbar^2}{2m}\frac{\partial^2}{\partial z_2^2} + V(z_2),$$

where $z_1 = Z + z/2$, $z_2 = Z - z/2$. Then, with $\alpha \equiv \{\alpha_1, q_1, \alpha_2, q_2, m_r\}$, we take the required set of $l = 0$ solutions to be

$$\psi_\alpha(\mathbf{r}, Z) \equiv \chi_{m_r}(r_\perp)\,\psi^{\alpha_1}_{q_1}(z_1)\,\psi^{\alpha_2}_{q_2}(z_2). \tag{3.35}$$

The Green's function for $l = 0$ is then given by eq. 3.17 as

$$G_E(r_\perp, r'_\perp, z_1, z'_1, z_2, z'_2) = \sum_{m_r,\alpha_1,q_1,\alpha_2,q_2} \frac{\chi_{m_r}(r_\perp)\chi^*_{m_r}(r'_\perp)\psi^{\alpha_1}_{q_1}(z_1)\psi^{\alpha_1 *}_{q_1}(z'_1)\psi^{\alpha_2}_{q_2}(z_2)\psi^{\alpha_2 *}_{q_2}(z'_2)}{E - \hbar\omega_\perp(2m_r+1) - E_{\alpha_1}(q_1) - E_{\alpha_2}(q_2) + i0^+} \tag{3.36}$$

To obtain the kernel, eq. 3.27, we note that only the difference of two Green's functions appears, evaluated at $r_\perp, r'_\perp \to 0$. Taking the limit $z, z' \to 0$ later, we can write

$$\begin{aligned} G^s_E(z, Z; z', Z') - G^{s=0}_{E_0}(z, Z; z', Z') \quad = \\ -\frac{m}{4\pi\hbar^2} \sum_{\alpha_1,q_1,\alpha_2,q_2} \psi^{\alpha_1}_{q_1}(z_1)\psi^{\alpha_1 *}_{q_1}(z'_1)\psi^{\alpha_2}_{q_2}(z_2)\psi^{\alpha_2 *}_{q_2}(z'_2) \sum_{m_r} \frac{1}{m_r + \frac{E_{\alpha_1}(q_1)+E_{\alpha_2}(q_2)+\hbar\omega_\perp - E}{2\hbar\omega_\perp}} \\ -same\,(s=0, E=E_0). \end{aligned} \tag{3.37}$$

Here, the states $\psi^{\alpha_1}_{q_1}(z_1)$ and energies $E_{\alpha_1}(q_1)$ in the first term are evaluated for the nonzero lattice parameters s and we have used eq. 3.32 to obtain $\chi_{m_r}(0)\chi^*_{m_r}(0)/(2\hbar\omega_\perp) = m/(4\pi\hbar^2)$.

We see that for each term in 3.37 the sum over m_r is divergent. However, the overall sum is convergent since the denominators in the s and $s = 0$ terms become identical in the limit $m_r \to \infty$ and the remaining sums over the band states are complete (eq. 3.7) and give $\delta(z_1 - z'_1)\delta(z_2 - z'_2)$ for any lattice depth. The sum over m_r then can be evaluated using

$$\sum_{m_r=0}^{\infty} \left(\frac{1}{m_r + b} - \frac{1}{m_r + c} \right) = \psi^{(0)}(c) - \psi^{(0)}(b), \tag{3.38}$$

where $\psi^{(n)}(x) \equiv (d/dx)^{n+1} ln[\,\Gamma(x)]$, i.e., polygamma$[n, x]$. The polygamma function is defined for all x, and diverges when x is zero or a negative integer. Note that integral values of x correspond to energies E that are resonant with a noninteracting two-atom states in eq. 3.37. For finite scattering length, bound states always correspond to non-integer x. We can choose the constant c to be the same for both sums in eq. 3.37, as the corresponding constant $\psi^{(0)}(c)$ will cancel. Taking $b = [E_{\alpha_1}(q_1) + E_{\alpha_2}(q_2) + \hbar\omega_\perp - E]/(2\hbar\omega_\perp)$ in the first term, we can replace the sum over m_r by $-\psi^{(0)}(b)$. Taking $z = z' = 0$, we have

$$\begin{aligned} G^s_E(0, Z; 0, Z') - G^{s=0}_{E_0}(0, Z; 0, Z') \quad = \\ \frac{m}{4\pi\hbar^2} \sum_{\alpha_1,q_1,\alpha_2,q_2} \psi^{(0)}\left[\frac{\epsilon_{\alpha_1}(q_1) + \epsilon_{\alpha_2}(q_2) + \beta - \tilde{E}}{2\beta} \right] \psi^{\alpha_1}_{q_1}(Z)\psi^{\alpha_1 *}_{q_1}(Z')\psi^{\alpha_2}_{q_2}(Z)\psi^{\alpha_2 *}_{q_2}(Z') \\ -same\,(s=0, E=E_0). \end{aligned} \tag{3.39}$$

Here, I have written all energies in recoil energy units, i.e., $E_{\alpha_1}(q_1) = \epsilon_{\alpha_1}(q_1)\,E_R$, $\hbar\omega_\perp = \beta\,E_R$

and $E = \tilde{E}\, E_R$. Then the relevant Kernel, $K_E^s(Z, Z')$ in 3.27 takes the following form,

$$K_E^s(Z,Z') = \frac{m}{4\pi\hbar^2} \sum_{\alpha_1,q_1,\alpha_2,q_2} \psi^{(0)}\left[\frac{\epsilon_{\alpha_1}(q_1)+\epsilon_{\alpha_2}(q_2)+\beta-\tilde{E}}{2\beta}\right] \psi_{q_1}^{\alpha_1}(Z)\psi_{q_1}^{\alpha_1 *}(Z')\psi_{q_2}^{\alpha_2}(Z)\psi_{q_2}^{\alpha_2 *}(Z') \\ -same\,(s=0, E=E_0) + K_{E_0}^{s=0}(Z,Z'). \tag{3.40}$$

3.1.3 Evaluating $M_{GG'}(E,Q)$

To solve the eigenvalue problem, eq. 3.23, numerically, I need to find a simplified expression for $M_{GG'}(E,Q)$ in eq. 3.24. By substituting eq. 3.40 in eq. 3.24 we define,

$$M_{GG'}(E,Q) = M_{G,G'}^s(E,Q) - M_{G,G'}^{(0)}(E_0,Q) + M_{G,G'}^0(E_0,Q), \tag{3.41}$$

where

$$M_{GG'}(E,Q) = \frac{4\pi\hbar^2}{m\,N}\int dZ \int dZ'\, e^{-i(G+Q)Z+i(G'+Q)Z'} \\ \frac{m}{4\pi\hbar^2} \sum_{\alpha_1,q_1,\alpha_2,q_2} \psi^{(0)}\left[\frac{\epsilon_{\alpha_1}(q_1)+\epsilon_{\alpha_2}(q_2)+\beta-\tilde{E}}{2\beta}\right] \psi_{q_1}^{\alpha_1}(Z)\psi_{q_1}^{\alpha_1 *}(Z')\psi_{q_2}^{\alpha_2}(Z)\psi_{q_2}^{\alpha_2 *}(Z') \tag{3.42}$$

and $M_{G,G'}^{(0)}(E_0,Q)$ is of the same form, evaluated for $s \to 0$ and $E \to E_0$. Note that the *difference* of the first two terms in eq. 3.41 is convergent, i.e., for high band number α, the Bloch states at finite lattice depth approach free particle states and the total energy becomes large compared to E and E_0. From eq. 3.27, the last term, $M_{GG'}^0(E_0)$, is the matrix element of the zero lattice depth kernel $K_{E_0}^{s=0}(Z,Z')$, which I will evaluate a little further below. Eq. 3.42 can be evaluated in Z, Z' coordinates separately by defining,

$$I_1 = \int_0^{Nd} dZ\, e^{-i(G+Q)Z}\psi_{q_1}^{\alpha_1}(Z)\psi_{q_2}^{\alpha_2}(Z) \\ = \sum_{G_1,G_2} C_{G_1}^{\alpha_1}(q_1)C_{G_2}^{\alpha_2}(q_2)\int_0^{Nd}\frac{dZ}{Nd}e^{i(q_1+G_1+q_2+G_2-G-Q)Z}, \tag{3.43}$$

and similarly for the Z' integral. Taking advantage of the periodicity, $\exp[i(G_1+G_2-G)nd] = 1$, we let $\tilde{Z} = Z - nd$ and write

$$\int_0^{Nd}\frac{dZ}{Nd}e^{i(q_1+G_1+q_2+G_2-G-Q)Z} = \sum_{n=0}^{N-1}\int_{nd}^{d+nd}\frac{dZ}{Nd}\,e^{i(q_1+G_1+q_2+G_2-G-Q)Z} \\ = \frac{1}{N}\sum_{n=0}^{N-1} e^{i(q_1+q_2-Q)dn}\int_0^d \frac{d\tilde{Z}}{d}\,e^{i(q_1+G_1+q_2+G_2-G-Q)\tilde{Z}}. \tag{3.44}$$

The first factor is a geometric series, which is unity for $q_1 + q_2 = Q + integer \times G_0$ and vanishes otherwise, since q_1, q_2, and Q are all integer multiples of $2\pi/(Nd)$. Taking $q_1 + q_2 = Q$, the remaining integral is just δ_{G,G_1+G_2}. The Z-integral is then

$$I_1 = \sum_{G_1,G_2} C^{\alpha_1}_{G_1}(q_1) C^{\alpha_2}_{G_2}(q_2)\, \delta_{Q,q_1+q_2}\, \delta_{G,G_1+G_2}. \tag{3.45}$$

The corresponding Z' integral is given by the complex conjugate of eq. 3.45, with $G, G_1, G_2 \to G', G'_1, G'_2$. Hence we deduce,

$$\begin{aligned} M^s_{G,G'}(E,Q) &= \frac{1}{N} \sum_{q_1,\alpha_1,\alpha_2} \psi^{(0)} \left[\frac{\epsilon_{\alpha_1}(q_1) + \epsilon_{\alpha_2}(Q-q_1) + \beta - \tilde{E}}{2\beta} \right] \\ &\quad \sum_{G_1} C^{\alpha_1}_{G_1}(q_1) C^{\alpha_2}_{G-G1}(Q-q_1) \sum_{G'_1} C^{\alpha_1 *}_{G'_1}(q_1) C^{\alpha_2 *}_{G'-G'_1}(Q-q_1) \end{aligned} \tag{3.46}$$

We can simplify the evaluation of the $s = 0$ term, $M^{(0)}_{G,G'}(E_0, Q)$, which contains free particle kinetic energies in the z-direction. Formally, for $s = 0$, the coefficients $C^{\alpha_1}_{G_1}(q_1)$ for each q_1 are nonzero only for one value of G_1, i.e., for the first three bands, $C^1_{G_1}(q_1) = \delta_{G_1,0}$, $C^2_{G_1}(q_1) = \delta_{G_1,-G_0}\theta[q_1] + \delta_{G_1,G_0}\theta[-q_1]$, $C^3_{G_1}(q_1) = \delta_{G_1,G_0}\theta[q_1] + \delta_{G_1,-G_0}\theta[-q_1]$. This requires $G'_1 = G_1$ and $G' = G$ for the sums over reciprocal lattice vectors. Defining $G = \tilde{G}k$, $Q = \tilde{Q}k$, etc., and noting that the dimensionless kinetic energy for atom 1 is $\hbar^2(G_1 + q_1)^2/(2mE_R) = (\tilde{G}_1 + \tilde{q}_1)^2$, and similarly for atom 2, the sum over all bands and all G_1 then gives the simple result,

$$M^{(0)}_{G,G'}(\tilde{E}_0, \tilde{Q}) = \delta_{G,G'} \frac{1}{N} \sum_{q_1,G_1} \psi^{(0)} \left[\frac{(\tilde{G}_1 + \tilde{q}_1)^2 + (\tilde{G} + \tilde{Q} - \tilde{G}_1 - \tilde{q}_1)^2 + \beta - \tilde{E}_0}{2\beta} \right]. \tag{3.47}$$

3.1.4 Evaluating the Kernel $K^{s=0}_{E_0}(Z, Z')$ and matrix element $M^0_{GG'}(E_0, Q)$

To complete the evaluation of eq. 3.41, we require the matrix elements $M^0_{GG'}(E_0, Q)$ of the zero lattice depth kernel $K^{s=0}_{E_0}(Z, Z')$, which are easily determined. We begin by noting that for $E = E_0$ and $s = 0$, the first two terms of eq. 3.41 cancel. As the momentum is conserved for zero lattice depth, eq. 3.23 is diagonal in G,

$$\frac{d}{a} B^{E_0}_G(Q) = M^0_{GG}(E_0)\, B^{E_0}_G(Q). \tag{3.48}$$

For zero lattice depth, the value of d/a is determined by the dimer binding energy and is independent of the CM energy. Hence, we can exploit the flexibility in the choice of E_0 in

eq. 3.41 (and eq. 3.27) to define a *fixed* reference d/a,

$$M^0_{GG'}(E_0) = (d/a)_{ref}\,\delta_{G,G'}, \tag{3.49}$$

by choosing $E_0 = E_0(G,Q)$ in the last two terms of eq. 3.41 to be the total energy for a *fixed* binding energy ϵ_b^{ref} (see eq. 3.52). The value of $(d/a)_{ref}$ is then related to ϵ_b^{ref} (reference binding energy in units of E_R) by

$$\left(\frac{d}{a}\right)_{ref} = \pi\sqrt{\frac{\beta}{2}}\,I_{dimer}(\epsilon_b^{ref}/\beta), \tag{3.50}$$

where the scattering length and dimer binding energy are related by [Zhang et al., 2012, Bloch et al., 2008],

$$\frac{l_\perp}{a} = I_{dimer}(\epsilon) \equiv \int_0^\infty \frac{dv}{\sqrt{4\pi v^3}}\left[1 - \frac{2v}{1-e^{-2v}}e^{-\epsilon v}\right]. \tag{3.51}$$

Here, $\epsilon = E_b/\hbar\omega_\perp$ is the binding energy in units of $\hbar\omega_\perp = \beta\,E_R$. In eq. 3.50, we have used $d/l_\perp = \pi\sqrt{\frac{\beta}{2}}$.

For eq. 3.49 and eq. 3.47 to be consistent, we use in eq. 3.47 the energy,

$$\tilde{E}_0(G,Q,\epsilon_b^{ref}) = \frac{(\tilde{G}+\tilde{Q})^2}{2} + \beta - \epsilon_b^{ref}, \tag{3.52}$$

where the first term is the free particle CM energy of the dimer along the z-axis and β is the radial ground state energy, both in units of E_R. From eq. 3.52, we see that the total energy argument in eq. 3.47 can be written as $2\tilde{x}^2 + (\tilde{G}+\tilde{Q})^2/2 + \beta - \tilde{E}_0 = 2\tilde{x}^2 + \epsilon_b^{ref}$, where $\tilde{x} = \tilde{G}_1 + \tilde{q}_1 - (\tilde{G}+\tilde{Q})/2$. In the continuum limit, with $\sum_{G_1,q_1} \to (N/2)\int_{-\infty}^{\infty} d\tilde{x}$, one can show that $M^{(0)}_{G,G}(\tilde{E}_{01},\tilde{Q}) - M^{(0)}_{G,G}(\tilde{E}_{02},\tilde{Q}) = d/a_1 - d/a_2$, with d/a_1 and d/a_2 given by eq. 3.50 and $\tilde{E}_{01}$ and $\tilde{E}_{02}$ given by eq. 3.52 for binding energies ϵ_{b1}^{ref} and ϵ_{b2}^{ref} respectively. With eq. 3.49, this result assures that the total matrix $M_{GG'}(E,Q)$ of eq. 3.41 is independent of the choice of reference binding energy. For numerical evaluation with a finite number of bands, we choose ϵ_b^{ref} to be small compared to the maximum energy of the highest band.

Finally we can write down the matrix which is needed to be diagonalize as follows,

$$\begin{aligned} M_{GG'}(E,Q) \;=\; & \\ & \frac{1}{N}\sum_{q_1,\alpha_1,\alpha_2} \psi^{(0)}\left[\frac{\epsilon_{\alpha_1}(q_1)+\epsilon_{\alpha_2}(q_2)+\beta-\tilde{E}}{2\beta}\right] \sum_{G_1,G_1'} C^{\alpha_1}_{G_1}(q_1) C^{\alpha_2}_{G-G1}(q_2) C^{\alpha_1 *}_{G_1'}(q_1) C^{\alpha_2 *}_{G'-G_1'}(q_2) \\ & -\delta_{G,G'}\,\frac{1}{N}\sum_{q_1,G_1}\psi^{(0)}\left[\frac{(\tilde{G}_1+\tilde{q}_1)^2 + (\tilde{G}+\tilde{Q}-\tilde{G}_1-\tilde{q}_1)^2 - (\tilde{G}+\tilde{Q})^2/2 + \epsilon_b^{ref}}{2\beta}\right] \\ & +(d/a)_{ref}\,\delta_{G,G'} \end{aligned} \tag{3.53}$$

3.2 Numerical Implementation

Using eq. 3.53 in eq. 3.23, we find the eigenstates $f_E^Q(Z)$ (see eq. 3.22), and eigenvalues d/a for a fixed Q and selected total energy E. In units of E_R, we take the total energy in eq. 3.46 to be

$$\tilde{E} = 2\,\epsilon_1(Q/2) + \beta - \epsilon_b. \tag{3.54}$$

Here, we follow ref. [Orso et al., 2005] and define the binding energy ϵ_b relative to the energy of two noninteracting atoms in ground band, each with quasi-momentum $Q/2$. For the lowest band, with $\epsilon_b > 0$, this procedure assures that the total bound state energy lies below the continuum. Negative values of ϵ_b then correspond to higher lying bound states.

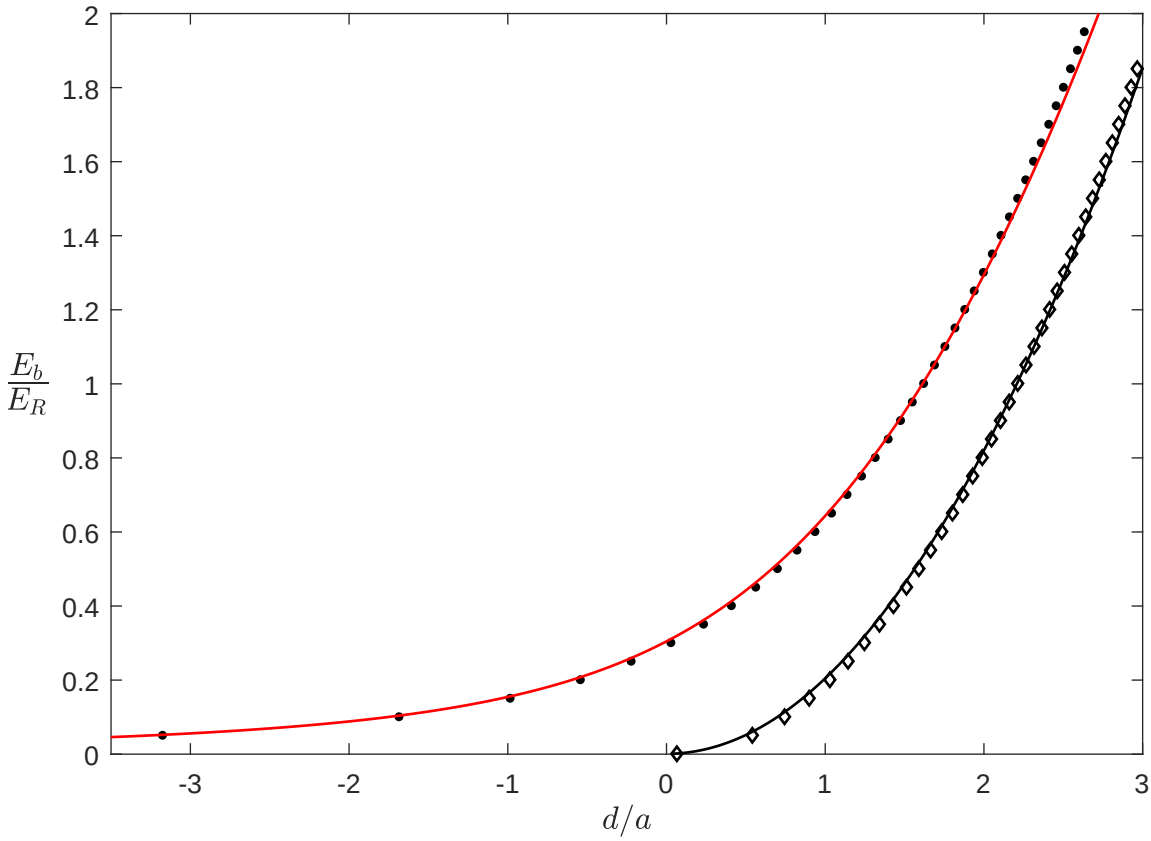

Figure 3.1: Binding energy versus d/a for zero lattice depth. Curves for $\beta = \hbar\omega_\perp/E_R = 0.5$(upper) and $\beta = 0.01$(lower) . Black dots/diamonds: Full diagonalization of eq. 3.23 for $s = 0$ (see text). Solid curves: Exact integral, eq. 3.50.

Eq. 3.23 is solved numerically using MATLAB. Note that the G_1, G_2 sums needed to be

done so that $G = G_1 + G_2$. Similarly for G_1', G_2' for each G'. To assures the convergence of the difference of the sums of first two terms of eq. 3.41 we first verify numerically that $M^{s\to 0}_{G,G'}(E \to E_0, Q) = M^{(0)}_{G,G'}(\tilde{E}_0, \tilde{Q})$. For nonzero dimer quasi-momentum Q, it is convenient, but not necessary, to symmetrize the sums over q_1 in eq. 3.46 and eq. 3.47, by taking $\tilde{q}_1 = \tilde{Q}/2 + \tilde{q}$ and performing the sum over $\tilde{q} = 2m_1/N$ for $-N/2 \le m_1 \le N/2 - 1$.

To check the consistency of the numerical implementation using a fixed $(d/a)_{ref}$, we consider first the zero lattice depth case, Fig. 3.1, for two different radial confinements, $\hbar\omega_\perp = 0.5\, E_R$, i.e., $\beta = 0.5$, and $\hbar\omega_\perp = 0.01\, E_R$, which approaches the free-space limit. We initially employ a 9 band model with 20 sites and take the reference binding energy to be $\epsilon_b^{ref} = 1.1$ in E_R units, giving $(d/a)_{ref} = 1.75$ for $\beta = 0.5$ and 2.31 for $\beta = 0.01$. For $s = 0$ and $\beta = 0.5$, we first

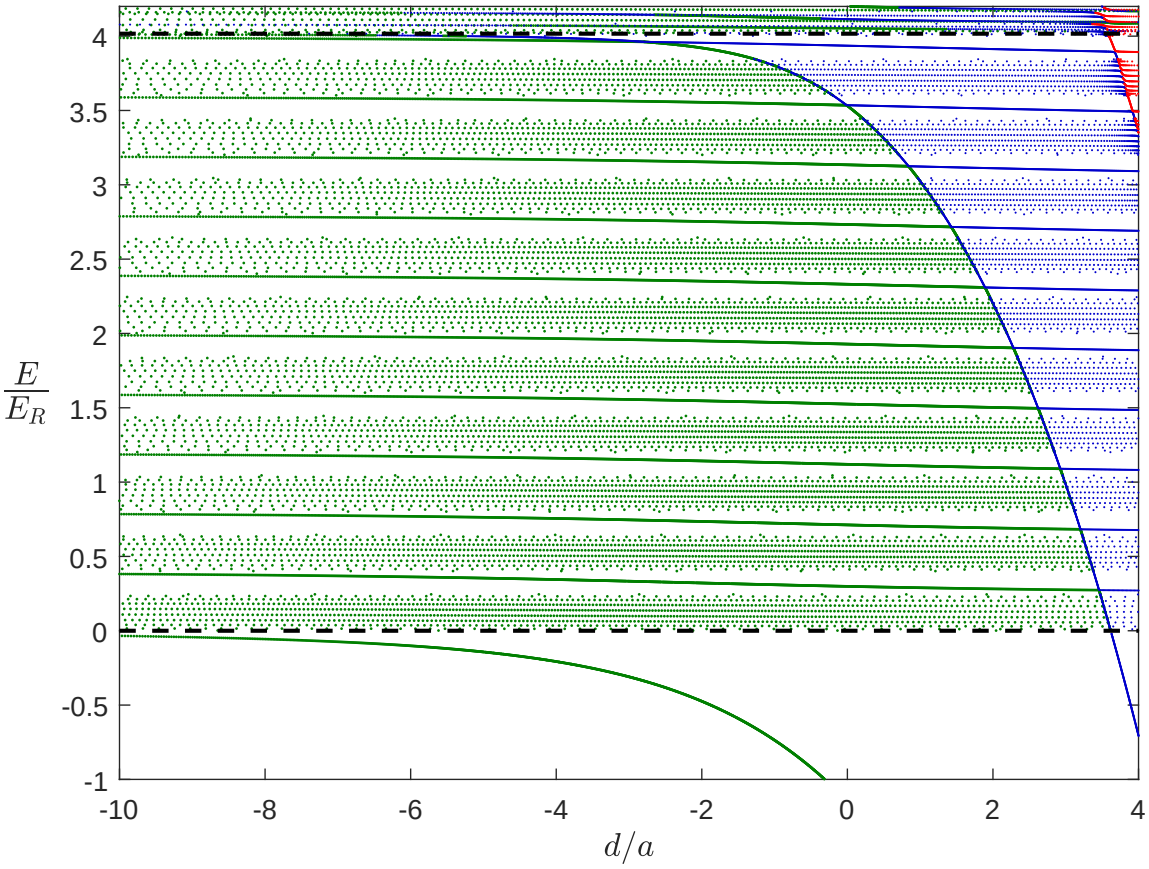

Figure 3.2: Total energy, E of two interacting atoms relative to the energy of two noninteracting atoms in ground band for dirfferent interaction strengths quantified by d/a where d is the lattice spacing and a is the s-wave scattering length. The lowest two d/a solutions (Green dots: 1^{st} sol. & blue dots: 2^{nd} sol.) are shown here. Dashed black lines represent the energy asymptots (see text). Red dots represent the third d/a solution.

diagonalize eq. 3.23 with $M_{G,G'}(E,Q)$ determined by eq. 3.41 and E by eq. 3.54. This yields 9 different d/a solutions for each input binding energy $\epsilon_b = E_b/E_R$. The lowest energy solution is displayed as the black dots on the upper left curve of the figure. The solid red curve on the left shows the exact integral, eq. 3.50, which determines d/a versus ϵ_b. Shown on the lower right are the corresponding results for $\beta = 0.01$ (full diagonalization: black diamonds) and exact integral (blue solid curve), which approach the free-space dimer binding energy (black-dashed curve), where $E_b = \hbar^2/(ma^2)$ for $a > 0$, i.e., $E_b/E_R = 2/\pi^2(d/a)^2$. As can be seen, both methods (i.e. eq. 3.50 and the full diagonalization of eq. 3.50) yeild identical results, as they should be for a zero lattice depth.

A typical energy diagram for a single color lattice ($s_1 = 8, s_2 = 0$) is shown in Fig. 3.2 with a finite radial confinement ($\beta = \hbar\omega_\perp/E_R = 0.2$). Fig. 3.2 shows the two lowest d/a solutions for a variety of energies E, as green and blue dots. Note that for $E > 0$ the change in color

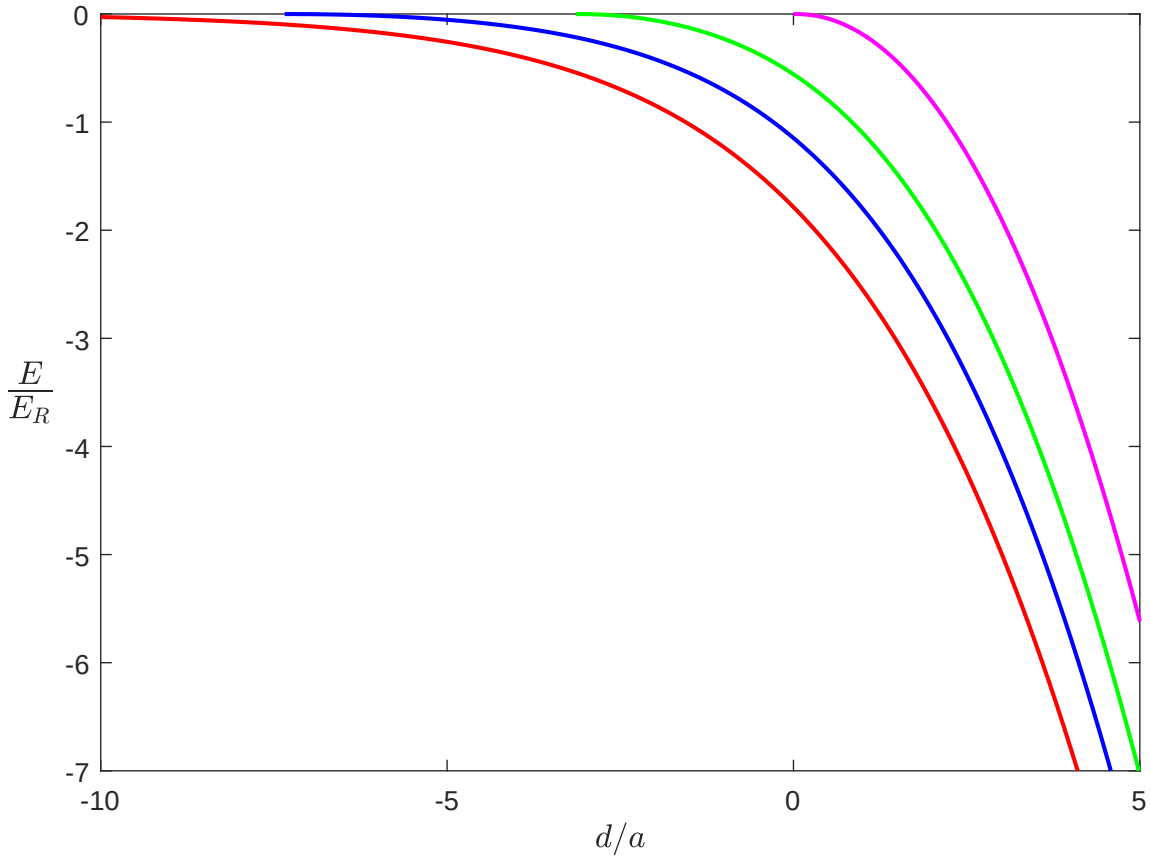

Figure 3.3: Binding energy versus d/a for different lattice depths: from top to bottom, $s_1 = 0, 5, 10, 20$ ($s_2 = 0$).

from left to right is a result of our d/a labeling: For the same E, the smallest (left most) d/a solutions are green, the next larger d/a solutions are blue. The lowest d/a solution (colored in green for $E < 0$ in Fig. 3.2) asymptotes to the lowest energy of two unbound atoms in the first band, $2\,E^1_{q_1=0} \equiv 0$, shown as the lower black horizontal dashed line. The second d/a solution (continuous blue curve in Fig. 3.2) asymptotes to the lowest energy for two unbound atoms, one in each of the first and second bands, $E^2_{\pm 1} + E^1_{\mp 1} - 2\,E^1_0$, shown as the upper black horizontal dashed line.

For a single color lattice, and small $\beta = 0.01$, we reproduce the results given for the ground band of ref. [Orso et al., 2005], for binding energies $\epsilon_b > 0$ in E of eq. 3.54. Note that here also, I only show you the lowest d/a solution. As expected when lattice depth is zero a bound state only exists for $d/a > 0$ (lowest curve on Fig. 3.3) where as for $s_1 > 0$, confinement supports a bound state even for $d/a < 0$.

3.2.1 Positive Energy States

In addition to the real bound states (i.e. $\epsilon_b < 0$), for $\epsilon_b > 0$, we obtain positive energy states, which lie above the ground state. The structure of these states as can be seen in fig. 3.2 is somewhat complicated, due to the discreteness of the radial and axial energies. In fig. 3.2, for $E > 0$ the coarse structure arises due to dicrete radial states while the fine structure arises from finite number of lattice sites, used in solving the eigenvalue problem. The finite number of lattice sites gives rise to discreste energies for the quasi-momentum states.

To examine the coarse structure closely, in fig. 3.4, I have shown the two particle energies obtained for a fairly deep lattice $s_1 = 40$ with $\beta = 0.2$. Green dots represent the energy eigenvalues obtained by diagonalizing eq. 3.23. Dashed black lines represent the energy states for two non interacting atoms in their lowest energy band and different radial states. These states are similar to those obtained for harmonic confinement in three dimensions [Idziaszek and Calarco, 2006]. As can be seen when d/a approaches negative infinity (i.e. when the interactions are weak) the total energy of the interacting system approaches the two free particle radial harmonic oscillator energy level structure. The first dashed line (at $E = 0$) represents the energy of two free particles in their ground bands with the lowest energy (i.e. energy corresponds to quasi-momentum, $q = 0$) and in their groud radial states (with energy equals to $\hbar\omega_\perp$ for each atom). The next dashed line represents the total energy of two particles in their first excited radial states (with energy equal to $2\hbar\omega_\perp$). Note that here, the fine structure is almost invisible since the single particle energy bands are flat (due to the high lattice depth chosen) and resemble the levels of a simple harmoinc oscillator.

Next, to take a close a look at the fine structure of fig. 3.2, I zoom in on the region where the total energy of the two particle system E, is in the range $-0.05 < E < 0.25$. Fig. 3.5 shows

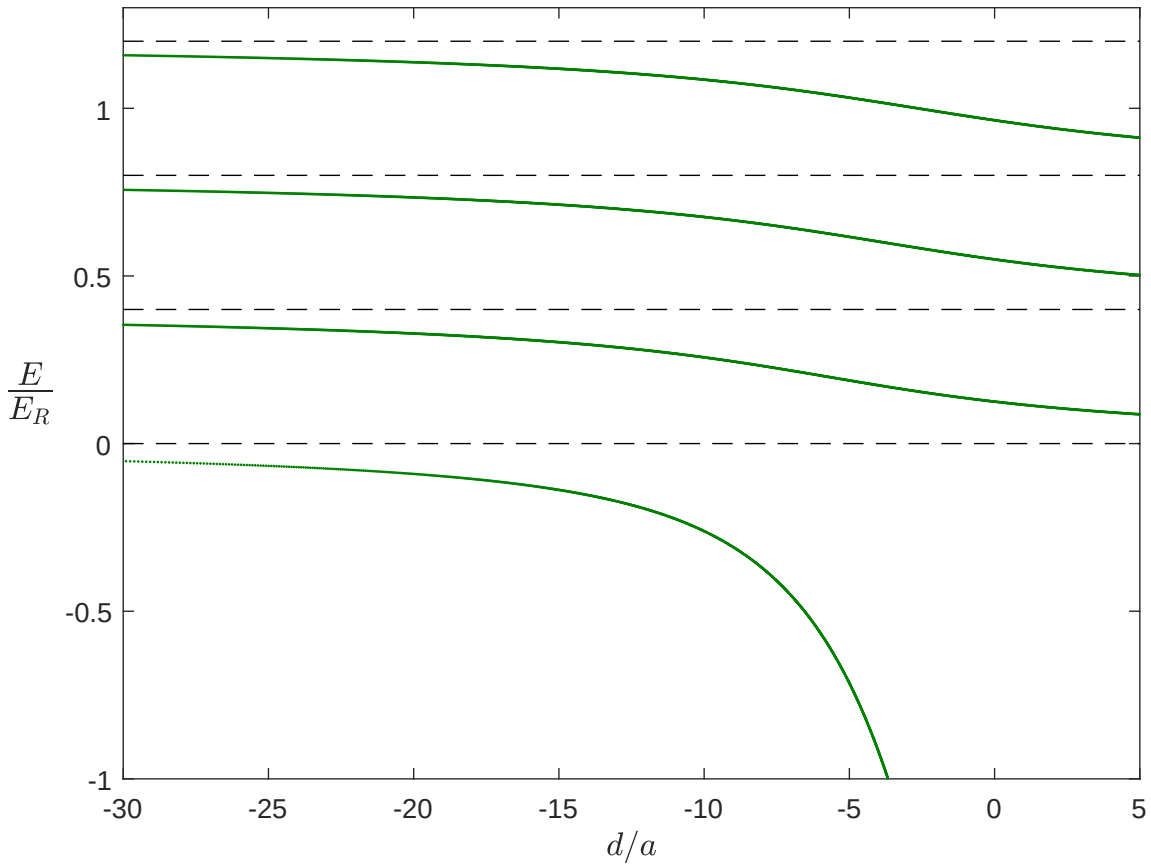

Figure 3.4: Green dots: Energy versus d/a for $s1 = 40$ with $\beta = \hbar\omega_\perp/E_R = 0.2$. Dashed lines: energy of two free particles in different radial states (equally spaced by $2\hbar\omega_\perp$ in E_R units).Note here $E = 0$ is taken as the total energy of two free particles in their ground bands with $q = 0$ and their ground radial harmonic oscillator states.

the behaviour of these positive solutions as they reach the noninteracting regime (i.e. d/a approaches negative infinity). Here in this figure, the horizontal black dashed lines reperesent the total energy of two free particles sitting on different quasi momentum states (i.e. different values of q) of the first energy band. As it can be seen from the figure the number of solutions are exactly eqauls to the number of discrete quasimomentum states we dicided to keep when solving the problem. For an infinitley long lattice this fine structure will turn in to a continuum. One more thing to note here is that the resolution of these energy diagrams stricly depends on the chosen resolution of the input energy, E when solving the eigen value problem. Typically the energies are input in equally spaced intervals, $\Delta E = 2.5 \times 10^{-6} E_R$. Smaller step sizes make the d/a solutions look more continuous.

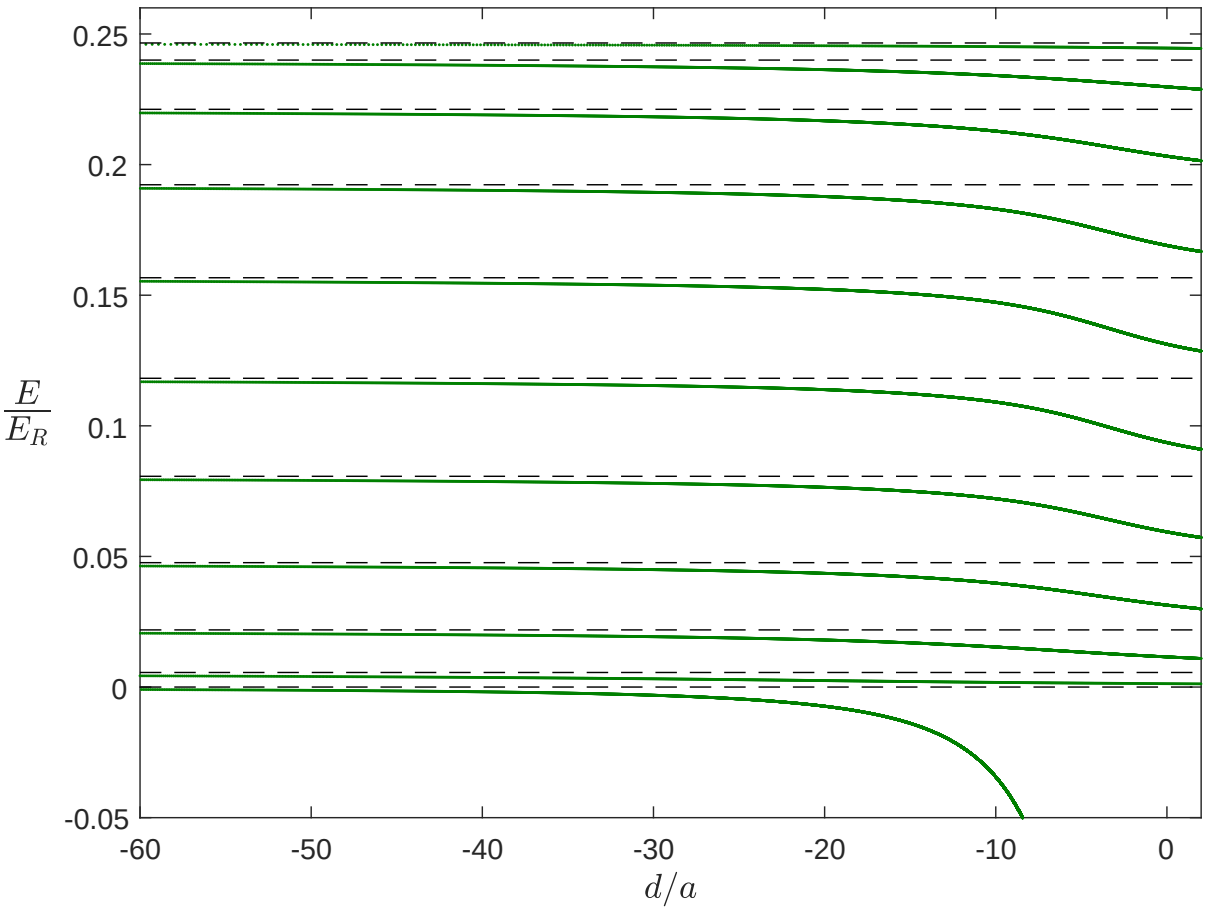

Figure 3.5: Expanded energy E versus d/a view of fig. 3.2 for $-0.05 < E < 0.25$. Horizontal black dashed lines are the energy asymptotes of two free particles in different q states in their ground band and ground radial harmonic oscillator states. Note that here

3.3 Two-Particle Wavefunction

The atom pair wavefunctions for total energy E are determined from eq. 3.18, using eq. 3.19,

$$\Psi_E(\mathbf{r}, Z) \propto \int dZ'\, G_E(\mathbf{r}, Z; 0, Z')\, f_E^Q(Z'), \tag{3.55}$$

where $f_E^Q(Z)$ is given by eq. 3.22. $G_E(\mathbf{r}, Z; 0, Z')$ is given by eq. 3.36, with the relative coordinates, $r'_\perp = 0$ and $z' = 0$,

$$G_E(\mathbf{r}, Z; 0, Z') = \sum_{m_r, \alpha_1, q_1, \alpha_2, q_2} \frac{\chi_{m_r}(r_\perp)\chi^*_{m_r}(0)\psi^{\alpha_1}_{q_1}(Z + z/2)\psi^{\alpha_2}_{q_2}(Z - z/2)\psi^{\alpha_1 *}_{q_1}(Z')\psi^{\alpha_2 *}_{q_2}(Z')}{E - \hbar\omega_\perp(2m_r + 1) - E_{\alpha_1}(q_1) - E_{\alpha_2}(q_2)}. \tag{3.56}$$

The Z' integral in eq. 3.55 is evaluated in the same way as eq. 3.44,

$$\begin{aligned} C^{\alpha_1,\alpha_2}_{q_1,q_2}(E,Q) &= \int_0^{Nd} dZ'\, \psi^{\alpha_1 *}_{q_1}(Z')\psi^{\alpha_2 *}_{q_2}(Z')\, f^Q_E(Z') \\ &= \delta_{Q,q_1+q_2} \sum_{G',G'_1} B^E_{G'}(Q) C^{\alpha_1 *}_{G'_1}(q_1) C^{\alpha_2 *}_{G'-G'_1}(q_2) \\ &\equiv \delta_{Q,q_1+q_2}\, \tilde{C}^{\alpha_1,\alpha_2}_q(E,Q), \end{aligned} \tag{3.57}$$

where we take $q_1 = Q + q/2$ and $q_2 = Q - q/2$ to define a symmetrized coefficient,

$$\tilde{C}^{\alpha_1,\alpha_2}_q(E,Q) \equiv \sum_{G',G'_1} B^E_{G'}(Q) C^{\alpha_1 *}_{G'_1}(Q/2+q) C^{\alpha_2 *}_{G'-G'_1}(Q/2-q), \tag{3.58}$$

which is determined by the eigenstate amplitudes $B^E_{G'}(Q)$.

With these definitions, we take the normalized wavefunctions to be

$$\begin{aligned} \Psi_E(\mathbf{r},Z) &= \frac{A}{\sqrt{N}} \sum_q \sum_{\alpha_1,\alpha_2} \tilde{C}^{\alpha_1,\alpha_2}_q(E,Q)\, \psi^{\alpha_1}_{Q/2+q}(Z+z/2)\, \psi^{\alpha_2}_{Q/2-q}(Z-z/2) \\ &\quad \times \sum_{m_r} \frac{\chi_{m_r}(r_\perp)}{m_r + \frac{\epsilon_{\alpha_1}(Q/2+q)+\epsilon_{\alpha_2}(Q/2-q)+\beta-\tilde{E}}{2\beta}}, \end{aligned} \tag{3.59}$$

where all energies are in units of E_R as above, and A is a normalization constant. Although the wavefunction is formally divergent for $r_\perp = 0$, it is normalizable, and can be used to compute the transition strengths discussed below in Sec. 3.4.

We determine A by requiring $\langle E|E\rangle = 1 = \int d^3\mathbf{r}\, dZ\, |\Psi_E(\mathbf{r},Z)|^2$. The radial integration is trivial, since the radial states are orthornormal. For the axial states, $dzdZ = dz_1 dz_2$ and $\psi^{\alpha_1}_{Q/2+q}(Z+z/2)\psi^{\alpha_2}_{Q/2-q}(Z-z/2) = \psi^{\alpha_1}_{q_1}(z_1)\psi^{\alpha_2}_{q_2}(z_2)$, which are also orthonormal. Then, for a dimer state of total energy E_1, we have

$$\langle E_1|E_1\rangle = 1 = |A_1|^2 \frac{1}{N} \sum_q \sum_{\alpha_1,\alpha_2} |\tilde{C}^{\alpha_1,\alpha_2}_q(E_1,Q)|^2 \psi^{(1)}\left[\frac{\epsilon_{\alpha_1}(Q/2+q)+\epsilon_{\alpha_2}(Q/2-q)+\beta-\tilde{E}_1}{2\beta}\right], \tag{3.60}$$

where $\psi^{(1)}(x) = \sum_{m_r}(m_r+x)^{-2}$ is polygamma$[1,x]$.

3.3.1 Axial Probabilty Distribution

We can calculate the axial probability distribution, $P_E^Q(Z,z)$ for any given energy, E and pair quasi momentum Q,

$$P_E^Q(Z,z) = \int_0^\infty 2\pi r_\perp \, dr_\perp \, |\Psi_E(\mathbf{r},Z)|^2 \int dX dY |\Phi_{CM}(X,Y)|^2. \tag{3.61}$$

Using eq. 3.59 and realizing $\int_0^\infty 2\pi \, r_\perp dr_\perp \, \chi^*_{m'_r}(r_\perp)\chi_{m_r}(r_\perp) = \delta_{m'_r,m_r}$ and $\int dX dY |\Phi_{CM}(X,Y)|^2 = 1$ we get,

$$P_E^Q(Z,z) = \frac{|A|^2}{N} \sum_{m_r} \left| \sum_{\alpha_1,\alpha_2} \frac{\tilde{C}_q^{\alpha_1,\alpha_2}(E,Q)\, \psi^{\alpha_1}_{Q/2+q}(Z+z/2)\, \psi^{\alpha_2}_{Q/2-q}(Z-z/2)}{m_r + \frac{\epsilon_{\alpha_1}(Q/2+q)+\epsilon_{\alpha_2}(Q/2-q)+\beta-\tilde{E}}{2\beta}} \right|^2. \tag{3.62}$$

Note that here $\sum_{m_r}$ formally includes an infnite number of terms. Hence when the problem is solved numerically, we include only a finite number of m_r terms. To see validity of including a

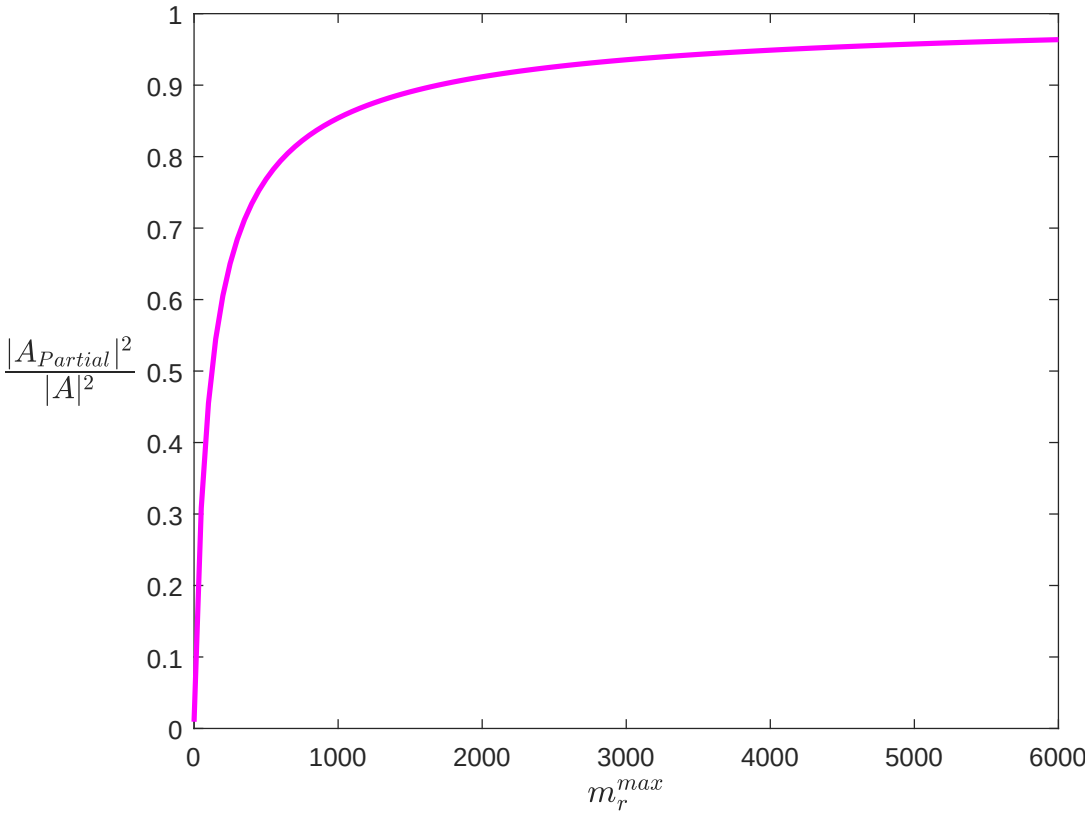

Figure 3.6: Value of $|A_{partial}|^2$ for different values of m_r^{max}. Calculation is done for a pair state with a total energy of $E = -2.37\, E_R$. Note that $\beta = 0.0166$, $s_1 = 8$, $s_2 = 16$.

finite number of terms first we calculate the partial norm, $|A_{partial}|^2$ by replacing the polygamma function in eq. 3.60 with an m_r sum, $\sum_{m_r}$ and truncating the series to a maximum value of m_r^{max}.

$$1 = |A_{partial}|^2 \frac{1}{N} \sum_q \sum_{\alpha_1,\alpha_2} |\tilde{C}_q^{\alpha_1,\alpha_2}(E_1, Q)|^2 \psi^{(1)} \sum_{m_r=0}^{m_r^{max}} \frac{1}{\left(m_r + \frac{\epsilon_{\alpha_1}(Q/2+q)+\epsilon_{\alpha_2}(Q/2-q)+\beta-\tilde{E}}{2\beta}\right)^2} \tag{3.63}$$

Fig. 3.6 shows how $|A_{partial}|^2$ approaches full norm as the number of m_r terms increases in eq. 3.63. The axial probability density $P_E^Q(Z, z)$ helps us to understand how the atom pair is

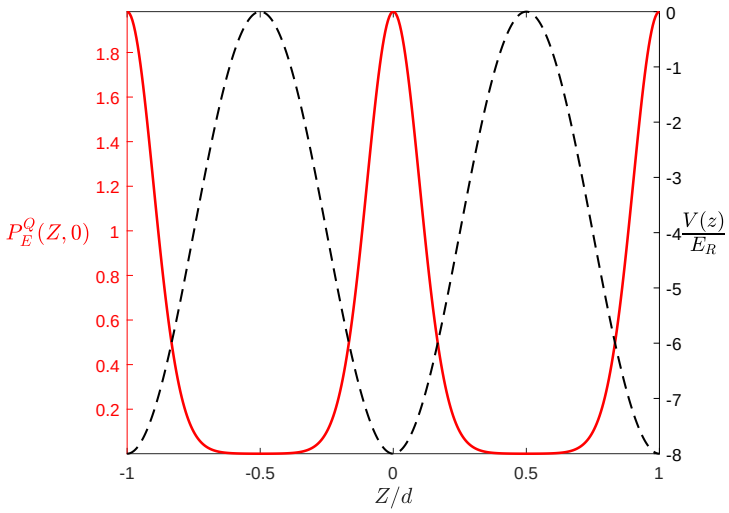

Figure 3.7: CM probability density (solid line) in the axial direction of a pair with total energy, $E = -1.8$. Dashed line shows the lattice potential for a lattice of $s_1 = 8$ and $\beta = 0.0166$.

spread along the lattice direction, based on its total energy. First let's look at $P_E^Q(Z, z)$ when relative distance between the atoms z equals to zero. This tells us how the CM of the pair is spread along the lattice direction. In fig. 3.7 solid line shows the probability density, $P_E^Q(Z, 0)$ for a single color lattice potential of $s_1 = 7$ with a total energy $E = -1.8E_R$. The dashed line shows the lattice potential in Z. As it is expected the pair CM wavefunction peaks up at each lattice site showing how the pair is localized at each lattice site.

Next, to explore further we can also look at the CM axial probability distribution of an atom pair in a bichromatic potential. Fig. 3.8 shows the energy diagram for two particles in a bichromatic potential as a function of the scattering length. Note that here only the two lowest d/a solutions are shown for $E < 0$. Here, A and B are the pairing states with $d/a = 1.28$,

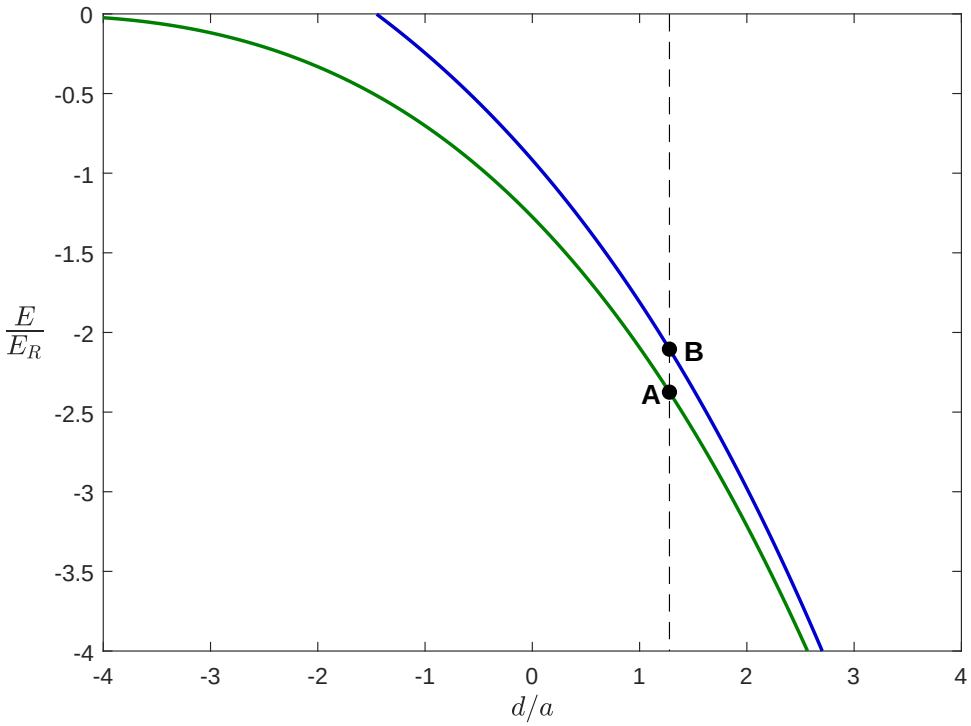

Figure 3.8: Total energy, E of two particles for a lattice of double-well potentials ($s_1 = 8$, $s_2 = 16$ and $\phi = 0$) versus d/a. A and B show the pairing states with $d/a = 1.28$. Note again that $E = 0$ reperent the energy of two free atoms in their graound band (at $q = 0$) and ground radial harmonic oscillator states.

veritcal dashed line in Fig. 3.8 [Note: As it was discussed in Chapter 2, experimentally the scattering length between two atoms, each in a different hyperfine states, can be magnetically tuned via Feshbach resonance. This means, if the atoms of a certain hyperfine mixture (ex: $|1\rangle$ - $|2\rangle$ mixture) is loaded in to the bichromatic lattice potential, Feshbach resonanse between those two states allows us to explore any point along the $x-$axis of Fig. 3.8. So, for the purpose of our discussion here, I have chosen to look at the axial probability distributions of atom pair states at $d/a = 1.28$]. CM axial probability distribution for paring states A and B with $d/a = 1.28$ are plotted in fig. 3.9.

As expected, again we can see that the CM of the pair is delocalized around the double-well center at $Z/d = 0$ and is found in either right or left well of the potential for the case where $\phi = 0$. In other words, as for state A (or B), there is an equal probability of finding it in either right or left well.

For the two states A or B, we can also look at the relative probabilty distribution $P_E^Q(z)$ for chosen value of Z. For a example, if we look at the distribution $P_E^Q(Z = 0.22, z)$ for solution A, it tells us how the atom pair is distributed along the lattice direction if the CM of the pair is

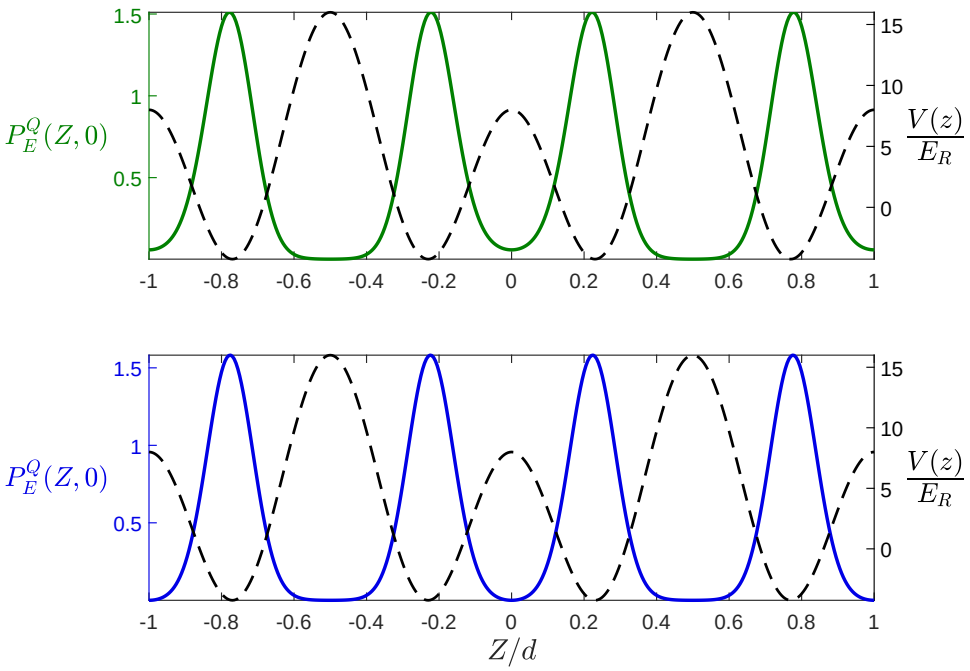

Figure 3.9: CM probability density in the axial direction of atom pair state A (Top/Green) and B (Bottom/Blue). Dashed line shows the lattice potential for a lattice of $s_1 = 8$, $s_2 = 16$, $\phi = 0$ and $\beta = 0.0166$.

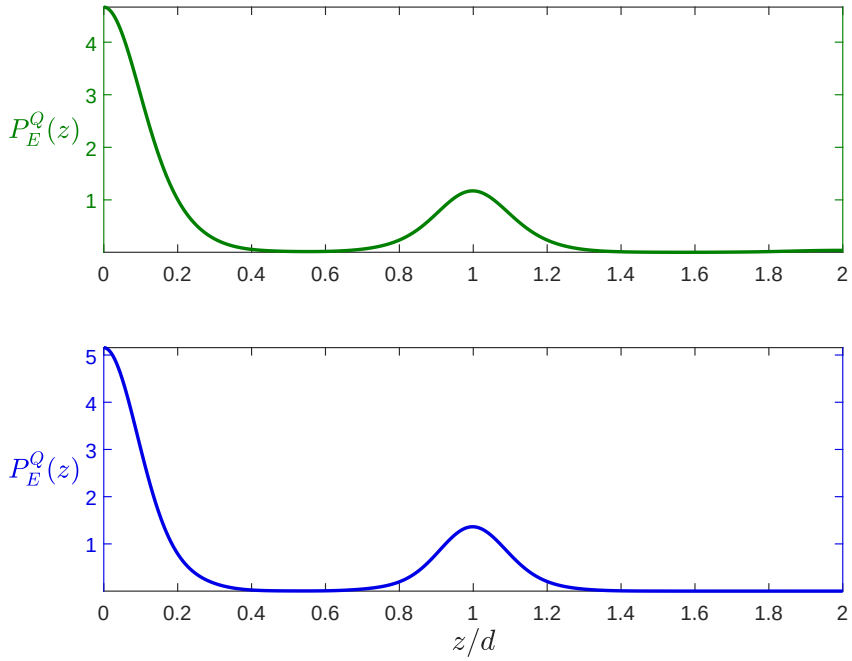

Figure 3.10: Relative probability density in the axial direction of atom pair state A (Top/-Green) and B (Bottom/Blue) of Fig. 3.8. Note the CM co-ordinate, $Z = 0.22$ for both states (see text)

assumed to be in one of the wells of the double-well potential (according to Fig. 3.9, $Z = 0.22$ assumes the CM of the pair is in the right-well). In fig. 3.10, I plot the probabilty of finiding one particle with respect to the other (i.e. $P_E^Q(z)$) as a function of their relative corordinate z in units of the lattice spacing d. Fig. 3.10 shows that for pairing states both A and B, the size of the pair is mostly confined to the potential well that they sit in.

It is also interesting to see what happens to these probabilities when you change phase between the two lattices so that the double well potential get slightly tilted. Fig. 3.11 shows the CM probability density for the tilted double well potential. Here the phase, $\phi = \pi/8$. We can see that now the right well, with respect to the double-well center has become slightly deeper than the left well hence localizing the highier energy solution (Green solid line) A within itself. Lower energy solution is now localized in the left well of the double-well potential.

Corresponding relative probability densities are shown in Fig. 3.12. Note that here, for state A, CM co-ordinate Z is chosen to be equal to 0.2, since the atom pair is localized in right well of the double-well potential (see Fig. 3.11) while for state B, $Z = -0.25$ as it is localized in the right well.

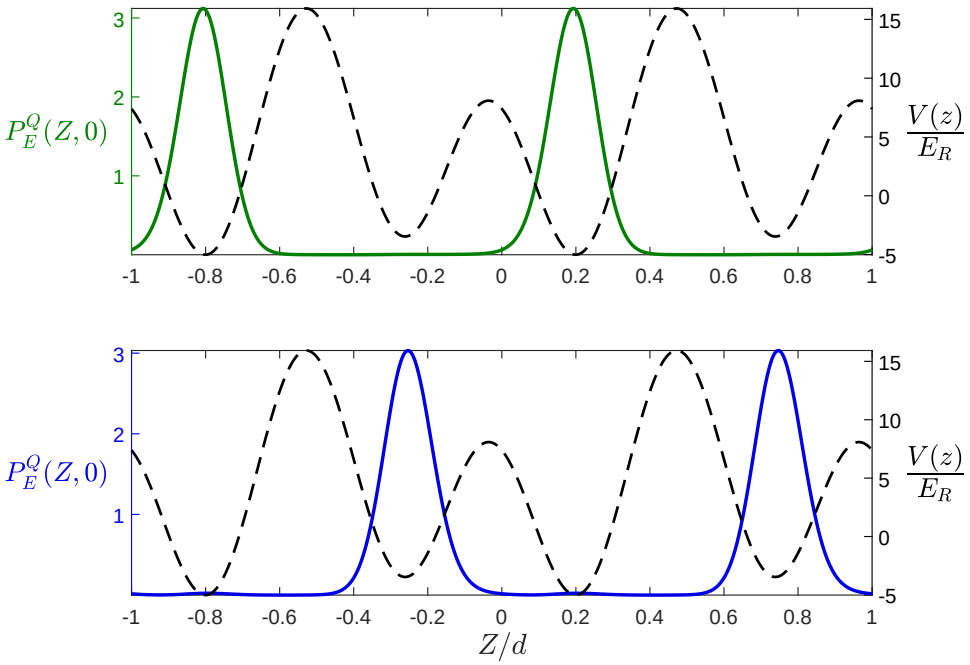

Figure 3.11: CM probability density in the axial direction of atom pair state A (Top/Green) and B (Bottom/Blue). Dashed line shows the lattice potential for a lattice of $s_1 = 8$, $s_2 = 16$, $\phi = \pi/8$ and $\beta = 0.0166$.

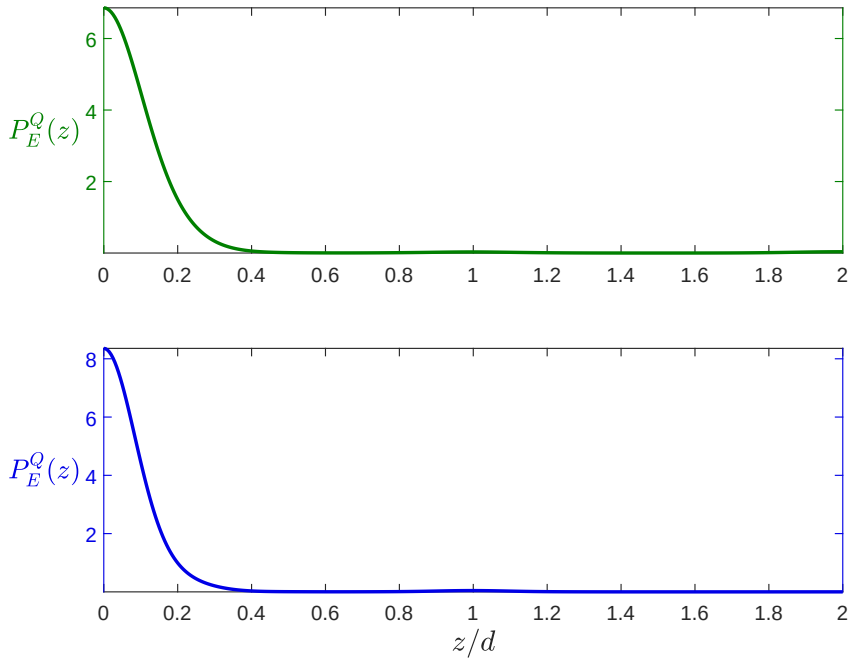

Figure 3.12: Relative probability density in the axial direction of atom pair state A (Top/-Green) and B (Bottom/Blue). For state A the CM coordinate, $Z = 0.2$ and for state B, $Z = -0.25$ (see text)

3.4 Transition Strengths

In the experiments, we employ a mixture of the two lowest hyperfine states of ^{6}Li, denoted $|1\rangle$, $|2\rangle$ and use a radio-frequency pulse to induce transitions from state $|2\rangle$ to an initially unpopulated state $|3\rangle$. For a given bias magnetic field, the s-wave scattering length for a $|1,2\rangle$ atom pair is generally different from that of the final $|1,3\rangle$ pair. To determine the Franck-Condon factors, we therefore need to compute the overlap integral between atom pair wavefunctions with different energies and different d/a values. The overlap integrals for two dimer states of total energies E_1 and E_2,

$$\langle E_2|E_1\rangle = \int d^3\mathbf{r}\, dZ\, \Psi^*_{E_2}(\mathbf{r}, Z)\Psi_{E_1}(\mathbf{r}, Z)$$

are similarly determined,

$$\begin{aligned}\langle E_2|E_1\rangle &= A_2^* A_1 \frac{1}{N}\sum_q \sum_{\alpha_1,\alpha_2} \tilde{C}_q^{\alpha_1,\alpha_2 *}(E_2,Q)\tilde{C}_q^{\alpha_1,\alpha_2}(E_1,Q) \\ &\quad \frac{2\beta}{\tilde{E}_2-\tilde{E}_1}\left\{\psi^{(0)}\left[\frac{\epsilon_{\alpha_1}(Q/2+q)+\epsilon_{\alpha_2}(Q/2-q)+\beta-\tilde{E}_1}{2\beta}\right]\right. \\ &\quad \left.-\psi^{(0)}\left[\frac{\epsilon_{\alpha_1}(Q/2+q)+\epsilon_{\alpha_2}(Q/2-q)+\beta-\tilde{E}_2}{2\beta}\right]\right\}. \qquad (3.64)\end{aligned}$$

Here, we have used $\sum_{m_r}(m_r+b)^{-1}(m_r+c)^{-1} = [\psi^{(0)}(c)-\psi^{(0)}(b)]/(b-c)$. In the limit, $|\tilde{E}_2\rangle \to |\tilde{E}_1\rangle$, it is easy to show that eq. 3.64 is equivalent to eq. 3.60.

Overlap integrals also can be computed from eq. 3.23, using the fact that $M_{GG'}(E,Q)$ of eq. 3.41 is hermitian,

$$\begin{aligned}\left(\frac{d}{a_1}-\frac{d}{a_2}\right)\sum_G B_G^{E_2 *}(Q)B_G^{E_1}(Q) &= \sum_{G,G'} B_G^{E_2 *}(Q)[M_{GG'}(E_1,Q)-M_{GG'}(E_2,Q)]B_{G'}^{E_1}(Q) \\ &= \sum_{G,G'} B_G^{E_2 *}(Q)[M^s_{GG'}(E_1,Q)-M^s_{GG'}(E_2,Q)]B_{G'}^{E_1}(Q), \qquad (3.65)\end{aligned}$$

where the $s=0$ terms in eq. 3.41 are independent of E and cancel. Then, using eq. 3.65, with eqs. 3.46, 3.58, and 3.64, it is straightforward to obtain

$$\langle E_2|E_1\rangle = A_2^* A_1 \frac{2\beta}{\tilde{E}_2-\tilde{E}_1}\left(\frac{d}{a_1}-\frac{d}{a_2}\right)\sum_G B_G^{E_2 *}(Q)B_G^{E_1}(Q). \qquad (3.66)$$

Normalization, eq. 3.60, determines the amplitudes A_1 and A_2. Numerical evaluation confirms that eq. 3.66 and eq. 3.64 yield precisely the same results as they should. Eq. 3.66 shows that $\langle E_2|E_1\rangle = 0$ for $d/a_1 = d/a_2$ and $E_2 - E_1 \neq 0$, i.e., dimer eigenstates of the same Hamiltonian with different total energies are orthogonal, as they should be. More importantly, Eq. 3.66 shows that $\langle E_2|E_1\rangle = 0$ for orthogonal eigenvectors $B_G^E(Q)$ of eq. 3.23, i.e., for orthogonal eigenstates $f_{E_2}^Q(Z)$ and $f_{E_1}^Q(Z)$ of eq. 3.22, which provides substantial insight, as the functions $f_E^Q(Z)$ are easily plotted.

Fig. 3.13 shows the normalized CM probabilty distribution of atom pair state A (solid line) $|f_{E_A}^Q(Z)|^2$ (Magenta circles), suggesting the close resemblance between the two-atom probability density $|\Psi_E(\mathbf{r},Z)|^2$, integrated along the $r_\perp$ direction with $z=0$, and the $f_{E_A}^Q(Z)$ functions. Figure 3.14 shows the CM probability density and the $f_{E_A}^Q(Z)$ of state A for $\phi = \pi/8$ case.

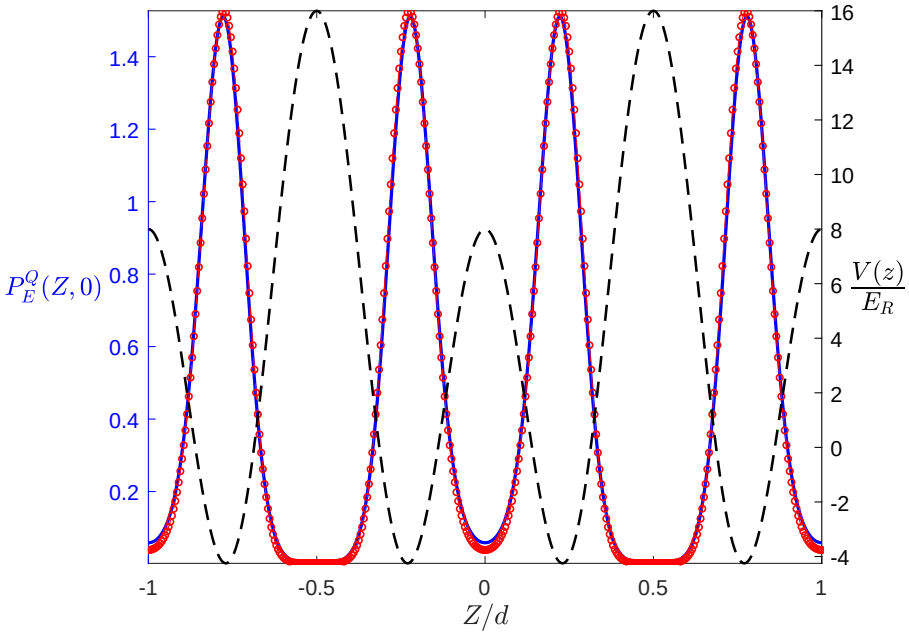

Figure 3.13: Solid Line: CM probability density in the axial direction of atom pair state A (Green) for $z = 0$ in Fig. 3.8 with $\phi = 0$. Magenta circles represents $|f_{E_A}^Q(Z)|^2$.

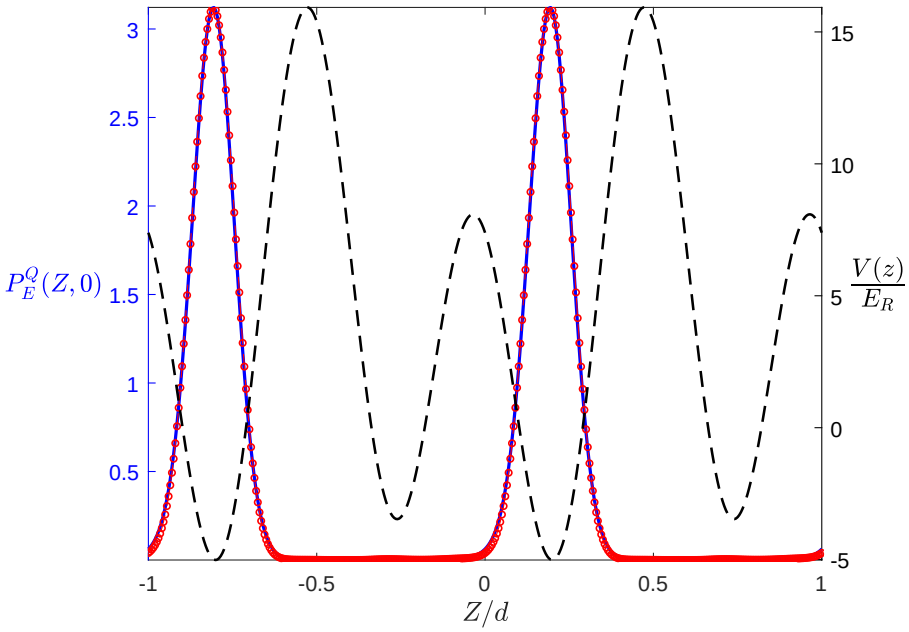

Figure 3.14: Solid Line: CM probability density in the axial direction of atom pair state A (Green) for $z = 0$ in Fig. 3.8 with $\phi = \pi/8$. Magenta circles represent $|f_{E_A}^Q(Z)|^2$.

Chapter 4

Experimental Methods

In this chapter, my main goal is to present the details of the experiment. First I will briefly explain the standard atom cooling and trapping procedure used for preparation of our sample. Then I will be discussing the techniques used to calibrate the lattice depths and the relative phase between the green and infrared beams. Finally, I provide a brief explanation on radio frequency spectroscopy, which is used to probe the biding energy of the atom pairs, as discussed in Chapter 3.

4.1 Preparation of the atomic sample

Sample preparation involves realizing a two component Fermi gas of ^{6}Li atoms (comprising atoms in the two lowest hyperfine states); using standard cooling and trapping techniques. Here, I wish to discuss this procedure in brief, but the reader is encouraged to refer to previous theses from our group members, if a thorough description is needed.

We start by evaporating solid ^{6}Li stored in an oven and directing the atomic beam in to a vacuum chamber where a magnito-optical trap (MOT) and a CO_2 laser optical dipole trap are used to cool and trap the atoms. In the process, solid ^{6}Li is heated up to about $\simeq 400°$C and vaporized through a long beam collimating wick nozzle such a way that the temperature from about 400°C at the oven to 250°C at the end of the nozzle. This temperature gradient assures that any condensed ^{6}Li is recycled back to the oven, greatly extending the lifetime of the oven.

As the thermal velocity of the atoms exiting the oven region is too high for them to be captured by a magneto-optical trap, a Zeeman slower with a counter propagating laser beam is used to slow the speed of the atoms to about 30 m/s. A standard MOT consists of pair of anti-Helmholtz coils with three orthogonal and retro-reflected red detuned (from the D2 transition of ^{6}Li) laser beams inside a vacuum chamber. A Coherent 899-21 dye laser pumped by a Verdi V-10 solid state laser along with standard frequency stabilization techniques, generates laser

beam with a wavelength near the ^{6}Li D_2 resonance near 671 nm, with a linewidth $\simeq$1 MHz to be used as the trapping beams for the MOT. At the end of the MOT cooling stage temperature is reduced to doppler limit of 140 μK, with an average velocity of about 60 cm/s. Atoms are then transfered to a far off-resonance optical dipole trap (FORT) before extinguishing the magnetic field and the trapping beams for the MOT. The MOT beams are extinguished and a bias magnetic field of $\sim$8 G is applied to break the degeneracy of $^2S_{1/2}$ ground state where the atoms are trapped. Then a frequncy modulated radio frequency pulse with a central frequency correspond to the energy splitting between the lowest two hyperfine states (states $|1\rangle$ and $|2\rangle$) is applied to obtained a balanced mixture of the lowest hyperfine states $|1\rangle$ and $|2\rangle$.

The optical trap beam with a wavelength of 10.6 μm is generated by a 140 W CO_2 laser. This beam is focused to a size of 50 μm $1/e^2$ radius, creating a peak trap depth of about 70μK . The bias magnetic field is then increased to 834 G where the Fechbach resoance occurs for a $|1\rangle - |2\rangle$ mixture, to enhance the collision rate between the atoms. At this stage, the atoms are evaporatively cooled by binary elastic collisions, where highier energy atoms escape the trap while reducing the temperature of the atoms that are left behind. At the end of this cooling stage we are left with about 500 thousand atoms per hyperfine state at a temperature of about 50 μK.

The atoms are then further cooled down using force evaporative cooling. Here the CO_2 potential is gradually lowered over afew seconds to continue the evaporation process, finally cooling the atoms between 10 and 100 nK.

4.2 Bichromatic Optical Lattice

The bichromatic superlattice potential is created by combining on a beam splitter two optical fields of wavelengths $\lambda_1 = 1064$ nm (which will be referred as "red") and $\lambda_2 = 532$ nm (which will be referred as "green"), with the second field obtained by frequency doubling of the first. Figure 4.1 shows a reasonably complete diagram of the lattice beam setup (note that the it does not include optical elements used for shaping the beams such as telescope setups, etc.). The $\lambda_1 = 1064$ nm beam is generated by a single frequency (linewidth $<$ 50 kHz), linearly polarized, CW ytterbium fiber laser (IPG Photonics: YLR-30-1064-LP-SF), which can generate up to 30W of usable power. We use a frequency doubling unit (Toptica Photonics: SHG Pro) with a conversion efficiency of about 40% to generate about 2W of the $\lambda_2 = 532$ nm light. Both of these beams are then passed through two acousto-optic modulators (AOM) (Gooch & Housego: R23080-1.06-LTD, MFS160-1C2B8-5), which control the intensity of the beams. The two AOMs are phase-locked using a RF drive/controller (Gooch & Housego: 64020-200-2ADSDFS-A-2CX) in order to preserve the two to one ratio of the input frequencies. The two beams are then coupled into two high power, single mode, polarization maintaining fibers

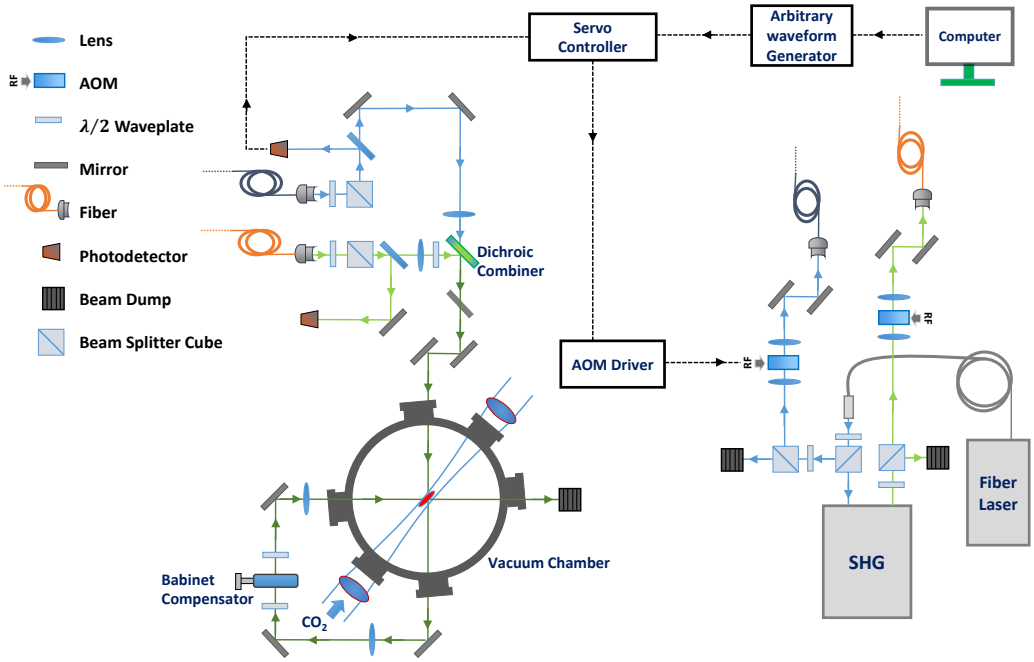

Figure 4.1: Bichromatic optical lattice beam grnerator. ≃5 W of power from 1064 nm beam (generated by a fiber laser) is frequency doubled using a second harmonic generator (SHG) to generate the 532 nm beam. The beams then go through phase-locked acousto optic modulators (AOM) and are coupled in to two high power fibers. At the output side close to the vacuum chamber, two beams are then combined on a dichroic combiner to co-propagate. After exiting the chamber, two beams are propagated through a Soleil-Babinet compensator, which controls the relative phase between the lattices.

(OZ Optics: PMJ-A3HPC,A3HPC-1064-6/125 and QPMJ-A3HPC,A3HPC-488-3.5/125) with a $\sim 60\%$ transmission efficiency.

Close to the vacuum chamber, output beams from the fibers are passed through two focusing lenses and combined on a dichroic beam combiner. The lenses assure that the two beams are focused in the same plane inside the vacuum chamber where the atom cloud is. Red beam is focused to a spot size($1/e$ field radius) of $80\,\mu$m while the green beam is focused to $100\,\mu$m. The two beams then co-propagate after they are being combined at the dichoric combiner and pass through the atom cloud once before exiting the chamber. The angle at which the beams propagate with respect to the CO_2 laser trap beam are carefully calculated using absorption images of the cloud [Cheng, 2016]. After exiting the chamber, the beams are then re-collimated

and propagated through a Soleil-Babinet compensator (Karl Lambert Corp: K1149), which controls the phase between the two fields manually. This permits control of the relative phase of the red and green standing wave optical potentials. Calibration of the Babinet compensator is discussed in Sec. 4.6. Finally, the two beams are then refocused and redirected in to the chamber to create the bichromatic optical lattice potential.

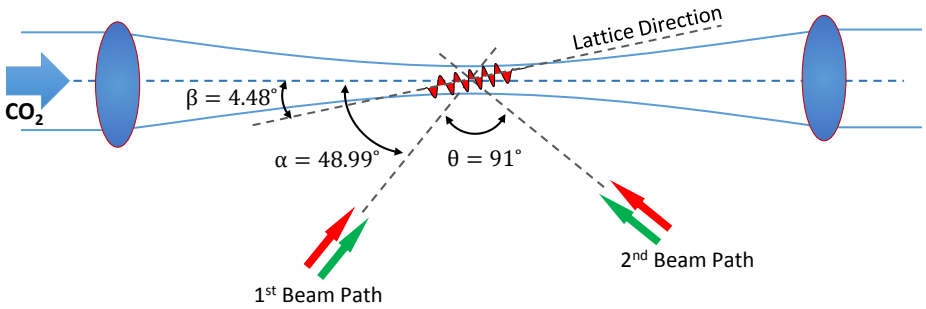

Figure 4.2: Bichromatic optical lattice beam arrangement. Note that all three beams (CO_2, 1^{st} and 2^{nd} lattice beams) lie on the same plane. α and β are carefully measured experimentally [Cheng, 2016]. The angle between the two beams that make up the lattice is $\theta = \pi - (\alpha - \beta) = 91°$, which determines the lattice periods.

4.3 Lattice Loading

At the end of the forced evaporation process described in Sec. 4.1 the atoms are ready to be loaded in to the bichromatic potenial. Figure 4.3 shows the experimental sequence for the experiments that are described in this thesis. After FREE evaporation process, the CO_2 laser FORT potential (denoted as the solid blue curve in Fig. 4.3) is lowered to about 0.2% from its peak value during the force evaporation. At the end of this process the FORT potential is kept at it's lowest value and the atoms are then adiabatically loaded into the red lattice by increasing the intensity of the red lattice beams over a 250 ms time period (denoted as the solid red curve in Fig. 4.3).

After raising the red lattice to the desired depth, the CO_2 laser trap is increased to provide additional radial confinement as the repulsive green lattice potential (denoted as the solid green curve in Fig. 4.3) is ramped up over 250 ms. While the atoms are being loaded into the superlattice, the bias magnetic field is tuned to set the desired scattering length. The intensity of each of the lattice beams are stabilized using a servo-locking system in order to minimze

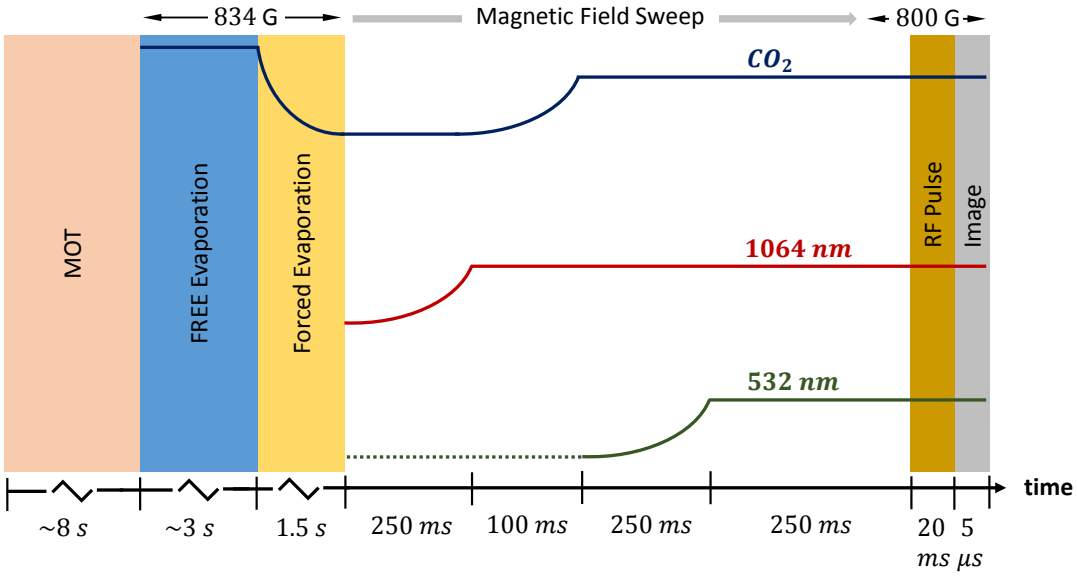

Figure 4.3: A typiclal timing sequence for the experiment. Solid purple, red and green curves shows the variation of the potential depth of the CO_2 laser beam trap, red lattice (denoted as 1064 nm) and the green lattice (denoted as 532 nm) consecutively. The bias magnetic field is also tuned from 834 G to a final field of interest (here to 800 G) to set the desired scattering lenght a. 20 ms radio frequency (RF) pulse is applied to probe tha binding energy of the atom pairs, prior to taking an absorbtion image using a 5 μs resonance optical pulse to measure the atom number in a chosen hyperfien state.

the fluctuations in the lattice potential that can lead to both parametric heating of the atomic sample and also to inaccurate spectral measurements described in Sec. 4.7. A portion of the each lattice beam at the output of their fibers, is directed to a photo diode (see Fig. 4.1) to monitor their power. Each of these outputs is then fed in to a servo-controllers where this photodiode signal is then servo-locked to a user-definedd value generated by a computer controlled arbitrary waveform generator.

4.4 Lattice Beam Alignment

Lattice beam alignment is critical and is done in two steps. First the red beam and the green beam are aligned with each other before and after the vacuum chamber to ensure their co-propagation. This is done using two CMOS cameras (ThorLabs: DCC1545M-GL) placed before and after the vacuum chamber (see Fig. 4.4). After red and green beams are combined at the dichroic combiner, a flipper mirror (FL1) is used to reflect the beams towards first camera

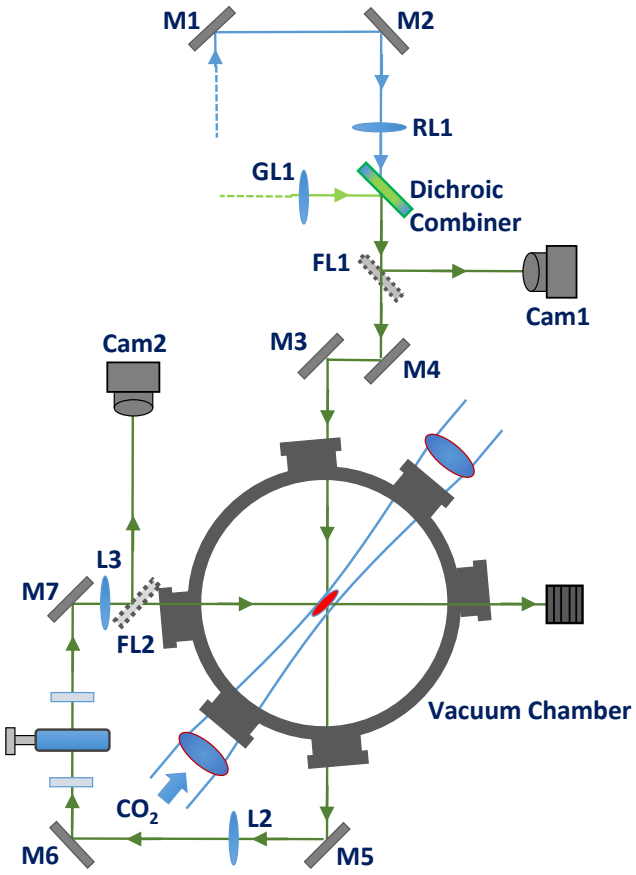

Figure 4.4: Lattice beam setup close to the vacuum chamber. RL1 and GL1 are the lenses that facus red and green beams into the vacuum chamber. Cam1 and Cam2 are used to align the red and green beams with each other. FL1 and FL2 denote flipper mirrors that can be flipped in and out of the beam path.

(Cam1), which is placed exactly a focal length away from focusing lenses for the two beams (GL1 and RL1). Then, the beam directing mirror M1 is adjusted both vertically and horizontally to overlap the red beam with the green beam on Cam1, making sure that the two beams co-propagate when they pass through the atom cloud on their way in to the vacuum chamber. A second camera, Cam2 is placed at the focal point of lens L2, which refocuses the beams back onto the atom cloud. Mirror M2 is then adjusted to align the Red beam on the Green beam on Cam2. Few iterations of this procedure assures that the two beams co-propagate along the 1^{st} and the 2^{nd} beam paths (see Fig. 4.2).

The second part of the alignment procedure is to make sure that the 1^{st} and the 2^{nd} beam paths (as labeled in Fig. 4.2) are overlapped with the atom cloud. A full description of this

alignment procedure is given in Ref [Cheng, 2016]. For the purpose of completness, I will also give a brief description of the method. As explained in Sec. 4.1 the atom cloud is imaged using an absorption image taken by a cameras placed in the plane of the lattice beams and perpendicular to the direction of propagation of the CO_2 laser beam (see Fig. 4.5) where the atoms are trapped before the lattice beams are applied. The position of the cloud is recorded on both the vertical and horizontal cameras in Fig. 4.5. Then the first lattice beam is shined on to the atoms and the atoms are trapped in it. Note that this step of the alignment procedure is done using only the red lattice beam, since the green beam exerts a repulsive force on the atoms making them leave the trap. Then the beam directing mirror M3 (see Fig. 4.4) is adjusted to match the position of the trapped cloud with the previously recorded position of the cloud when it was inside the CO_2 laser trap. The procedure is done on both the horizonatal and veritcal cameras in order to make sure the red beam is aligned in all x, y and z directions. Finally the second beam is shined on to the atoms and an absorption image is taken after extinguishing the CO_2 laser trap for $\sim 0.15\,ms$. The idea is to let the atom cloud trapped inside the cross beam optical lattice and record it's position. Now the beam directing mirror M7 is adjusted in order to match this position again with the previously recorded position of the CO_2 trap.

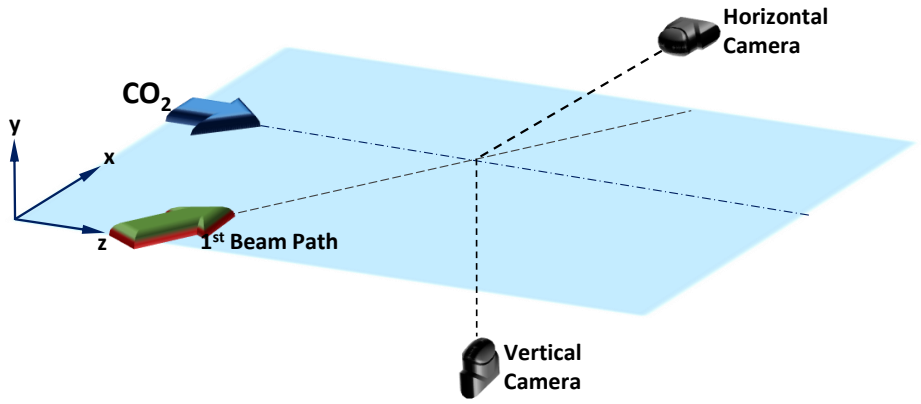

Figure 4.5: Lattice beams and CMOS camera arrangement. The two CMOS cameras are used to take absorption image of the atom cloud in two orthogonal directions. The red arrow represents the 1^{st} lattice beam (refer back to Fig. 4.2). The blue arrow represents the propagation direction of the CO_2 laser beam.

4.5 Lattice Depth Calibration

We calibrate the depth s_1 of the red lattice potential at 90% of maximum power by modulation of the lattice amplitude to induce interband transitions in a single-component gas [Cheng, 2016]. This yields $s_1 = 15$ in recoil energy ($E_R = \hbar^2 k^2/(2m)$) units. The results are consistent with Kapitza-Dirac scattering measurements [Cheng, 2016] to within 5%, where the lattice potential is pulsed, imprinting a phase variation across a trapped atomic sample. Releasing atoms leads to a multi-order interference pattern, with relative contrast of the orders determined by the lattice depth. We verify that the measured value of s_1 is consistent with the calculated depth using the measured beam powers and radii. In the RF spectroscopy experiments (described in Chp. 5), we reduce the laser power to scale the trap depth to the chosen value of $s_1 = 7.0$.

Calibrating the green lattice using the same techniques is more difficult, because the recoil energy is 4 times larger than that of the red. In this case, the maximum available green lattice depth is too low for a reliable Kapitza-Dirac scattering calibration due to fast dephasing. Using lattice modulation spectroscopy at 90% of maximum green power, we find $s_2 = 16$ in red recoil energy units to better than 10% accuracy, by employing a model fit to the measured modulation spectrum. The resolution is limited by the curvature of the second and the third bands. To fit the measured radio-frequency spectra (which will be presentend in Chapter. 5) using the theoretical model described in Chapter 3, first we fix the red lattice depth s_1 and the phase ϕ to the calibrated values (as described in Sec. 4.6), then we adjust s_2. Compared to the value of $s_2 = 16$ measured by modulation spectroscopy for the green lattice depth, we find that $s_2 = 16.5$ gives better fits to all of the spectra, which are obtained for several different phases and scattering lengths. Adjustment of s_2 by $0.5\,E_R$ produces only a small change in the peak positions of the spectra. For example, near $s_2 = 16.5$, the lower energy peak of the spectrum in Figs. 5.6 varies linearly with s_2 with a slope of 2.3 kHz/E_R.

4.6 Relative Phase Calibration

As mentioned in Section 4.2, the relative phase between the red and the green beam standing waves are controlled by a Babinet compensator. This consists of two birefringent wedges and a slab (see Fig. 4.6). Optical axes of the two wedges are oriented perpendicular to the axis of the slab. The refractive indices along the two perpendicular axes are labeled as n_o and n_e in Fig. 4.6. To understand how the Babinet compensator works, consider two laser fields, E_1 and E_2 (of two wavelengths with $\lambda_1 = 2\lambda_2 = \lambda$), which are cross polarized and progress through the device. Each field picks up a phase as it passes the wedges and the slab. According to the diagram, the phase change of field E_1 is, $\phi_1 = \frac{2\pi}{\lambda_1}[(n_o)_1 d + (n_e)_1 D]$ and for field $E-2$ is $\phi_2 = \frac{2\pi}{\lambda_2}[(n_e)_2 d + (n_o)_2 D)$. The phase difference between the two fields as they exit the babinet

is then,

$$\phi = \phi_1 - \phi_2 = \frac{2\pi}{\lambda}[(n_o)_1 - 2(n_e)_2]d + \frac{2\pi}{\lambda}[(n_e)_1 - 2(n_o)_2]D. \tag{4.1}$$

Note that, when the two beams (i.e. red and green beams) enter the vacuum chamber for the first time the electric fields of both beams are linearly polarized in the same direction. So after exiting the vacuum chamber, the polarization direction of the green beam is selectively rotated by 90° using a half-wave plate such that the two beams are cross polarized as they enter the Babinet. In the real Babinet compensator, the top wedge (see Fig. 4.6) is adjustable perpendicular to the propagation direction of the beams by a micrometer. This allows the thickness d to be continuously varied, hence changing the relative pahse differnce, ϕ bnetween the two fields. First, we calibrate the tuning rate of the phase as a function of the micrometer reading. This

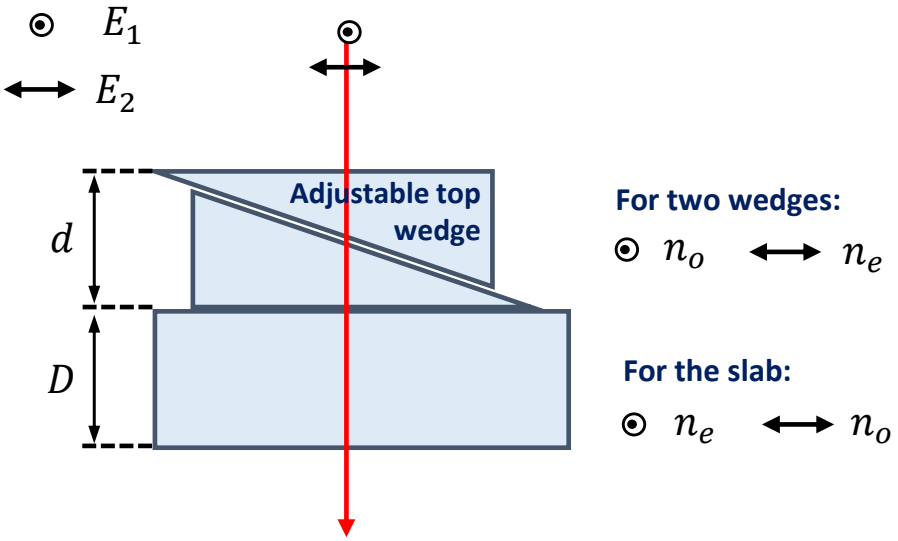

Figure 4.6: Construction of the Babinet compensator. E_1 and E_2 are two cross polarized optical fields. n_o and n_e are the refractive indices along the ordinary and extra-ordinary axes of the wedges and of the slab. Note that the top wedge can be translated perpendicular to the propagation direction of the optical fields (solid red line) to vary d using an attached micrometer actuator. d is the total thickness of the two wedges.

is accomplished by combining the red and green beams on a beam splitter and then interfering the beams with a small intersection angle. This creates simultaneous red and green intensity standing wave patterns on a large scale, which is imaged on a CCD array to precisely measure the change $\Delta\phi$ in the relative phase shift, for a given change in the micrometer reading. A full

description of this procedure is given in Ref [Cheng, 2016]. Next we determine the $\phi = 0$ point, which is done independently of the red and green lattice depths. First, we conduct a Kapitza-Dirac scattering experiment for a single component gas in the superlattice potential for various phases. The populations of negative and positive higher momentum components are unequal and interchange roles as the phase crosses either zero or π [Jo et al., 2012]. Distinguishing the two, and determining the zero phase position accurately is a somewhat complicated process. This will be discussed in more detail in Chapter 5. However, this procedure is not practical for use on a daily basis, since it takes a long time to implement.

Instead we find that the faster procedure of measuring the number of atoms loaded into the superlattice also determines the phase. For a weak CO_2 laser trap, the number of atoms loaded is sensitive to the radial confinement provided by the superlattice potential, since the radial confinement arising from the red and green components of the superlattice nearly cancels close to zero phase. Shifting the phase away from zero in either direction increases loading and allows determination of the zero-phase point to better than $\pi/70$. This precision is better than needed for the spectroscopic experiments, since two radio-frequency spectra (discussed in Sec. 4.7) taken $\phi = \pi/70$ apart are nearly indistinguishable. Note that the phase sensitivity of the spectra depends on the red and green lattice depths: for shallower lattices the peak positions and relative populations of bands tune more slowly with the phase. We verify the location of the zero phase point both before and after taking each data set. The phase ϕ determined by these calibration procedures is used as an input to the theoretical model described in Chap. 3, without further adjustment.

4.7 Radio Frequency Spectroscopy

We probe the binding energy of the atom pairs created in our bichromatic optical lattice potential using a radio frequency (RF) spectroscopy technique. As described in Sec. 4.1 we start by cooling and trapping a 50/50 mixture of atoms in the lowest two hyperfine states $|1\rangle$ and $|2\rangle$, Fig. 4.7. Once the atoms are loaded into the bichromatic potential, they can form $|12\rangle$ atom pair states. Then a radio frequency pulse is applied to transfer atoms from hyperfine state $|2\rangle$ to an initially empty hyperfine state $|3\rangle$. To understand the concept behind this technique, first consider a single component atomic gas in hyperfine state $|2\rangle$. Figure 4.7 show an energy diagram of the lowest three hyperfine states of ^{6}Li atoms at a specific magnetic field (see Fig. 2.6). To get the corresponding spectra experimentally, we scan the RF frequency and record the number of atoms left in state $|2\rangle$. This is achieved by selectively taking an absorption image of atoms in state $|2\rangle$ immediately after applying the RF pulse. Near 800 G, the typycal bare atomic resonance frequency, ν_{32}^0 is $\simeq$81 Mhz where a peak can be observed corresponding to a maximum atom loss from state $|2\rangle$.

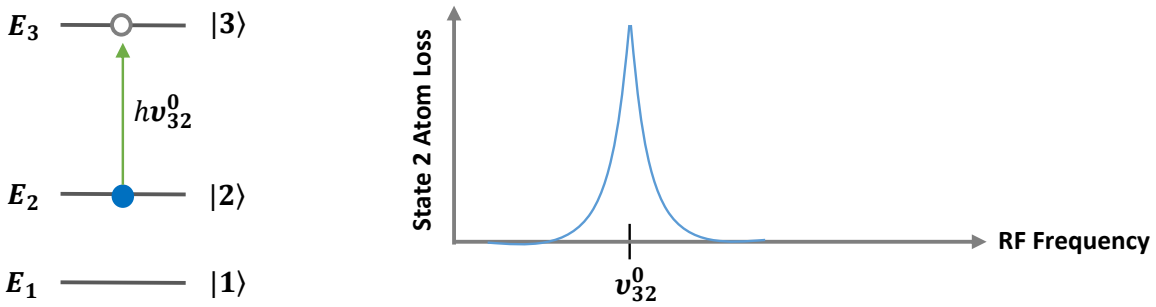

Figure 4.7: Left: RF transition between energy levels of a single component system. Right: Correnponding spectra of state $|2\rangle$ atom loss as a function of the input RF frequency. ν_{32}^0 is the resonance frequency.

In this thseis we are mostly interested to see how the spectrum changes when there is binding between the atoms present in the system. To understant the spectrum, consider an interacting mixture of $|1\rangle$ and $|2\rangle$ atoms. Figure 4.8 shows how the energy level diagram and the spectrum changes for the interacting mixture when two atoms pair. $E_1 + E_2$ is the total energy of the initial system if the two atoms are non-interacting. When the atoms are allowed

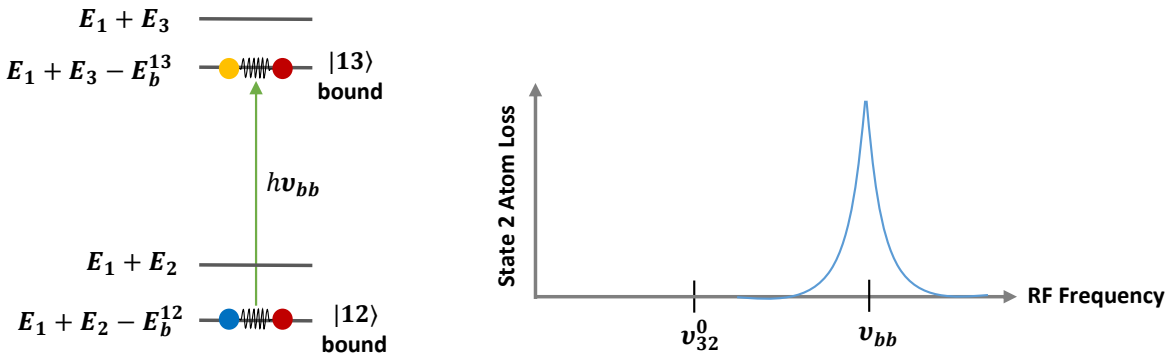

Figure 4.8: Left: RF transition between energy levels of an interacting system of $|1\rangle$ and $|2\rangle$. $E^1 2_b$ and $E^1 3_b$ are the binding energies of $|12\rangle$ and $|13\rangle$ atom pairs. Right: Correnponding RF spectra with a shifted pairing peak at $\nu_{bb}^0 = E_b^{12} - E_b^{13}$.

to pair, the total energy of the two-atom system is now shifted down by the binding energy, E_b^{12} of the pair. Now, if a RF pulse is applied to convert state $|2\rangle$ in to $|3\rangle$, this transforms the

$|12\rangle$ pairing state to a $|13\rangle$ pairing state. For the purpose of this discussion, we assume that probabilty of converting a $|12\rangle$ pair in to a $|13\rangle$ pair is unity (i.e. no bound to free transitions). Experimentally, if the Rf frequency is swept and the atom number on state $|2\rangle$ is monitored, a shifted pairing peak can be observed corresponding to a maximum atom loss. The peak position is now given by the resonance frequency $\nu_{bb} = (E_b^{12} - E_b^{13})$. And the corresponding spectrum is,

$$S(\nu) = \frac{1}{\pi} \frac{\gamma}{[\Delta\nu_{RF} - \nu_{bb}]^2 + \gamma^2}, \tag{4.2}$$

where $\Delta\nu_{RF} = \nu_{RF} - \nu_{32}^0$, is the RF frequency relative to the resonance frequency of the bare atom $|2\rangle \rightarrow |3\rangle$ transition. γ denotes the spectral linewidth (HWHM) $\simeq 1.8$ kHz, which is small compared to $(E_b^{12} - E_b^{13})/h$ and comparable to that of our previous measurements [Cheng et al., 2016].

Chapter 5

Experimental Results and Comparison with Theory

In this chapter, I will discuss two primary radio frequency (RF) spectra measured for two different phase configurations of the bichromatic lattice potential. I will compare these spectra against the theoretical model described in Chapter 3. However, before presenting the measured RF spectra, as promised in Sec. 4.6 in Chapter 4, the first section of this chapter describes how to find the zero phase (i.e. $\phi = 0$) accurately for the bichromatic potential, using the measured RF spectra. Then we will study the measured RF spectra near 800 G for $\phi = 0$ and $\phi = \pi/35$ cases in detail, and compare to predictions for total quasi-momentum of the atom pairs $Q = 0$. Finally, I will discuss how the measured spectra compare with the theory when $Q \neq 0$.

5.1 Finding Zero Phase

In Sec. 4.6, I discussed how the micrometer reading of the Babinet compensator is calibrated using the interference pattern created by combining the Red and Green lattice beams. This procedure is accomplished by setting up an interferometer on a test bench, which does not provide any information about how to find the zero phase between the two lattices when they are combined inside the vacuum chamber. Interfernce patterns only tell us how the phase change correspond to a given change in the micrometer reading. Kapitza-Dirac scattering helps us to distinguish 0 and ϕ phases from other values, yet cannot tell the two apart.

To distinguish the two, we measure the radio frequency spectra of atom pairs for several phase choices: π phase corresponds to a nominally single well potential with a higher depth and higher binding energy, than that of the 0-phase double-well. To determine the zero phase more accurately, we take spectra close to zero phase in steps of $\pi/35$ and deduce the zero point from the symmetry argument that the spectra should be identical under the change of the sign of

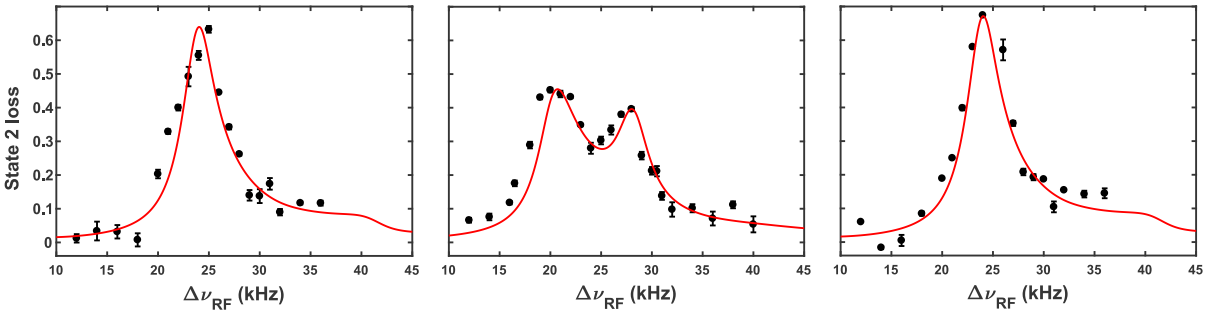

Figure 5.1: Radio-frequency $|12\rangle \rightarrow |13\rangle$ dimer transition spectra (black dots) versus predictions (red curves) for $B = 834.6$ G. Spectrum for (from left to right) $\phi = -2\pi/35$; $\phi = 0$; $\phi = +2\pi/35$. Error bars denote the standard deviation of the mean of 5 runs.

the phase. This is illustrated in Fig. 5.1 for $\phi = -2\pi/35$ and $\phi = 2\pi/35$, which are symmetric about $\phi = 0$. However as mentioned in Sec. 4.6, this is a rather tedious process to carry out on a daily basis, as it very time consuming. Instead we rely on phase dependent lattice loading measurements (described in Sec. 4.6)to find the zero phase.

5.2 Measured RF Spectra for a Symmetric Double Well Potential

We first consider the case of a series of symmetric double well potentials created by the bichromatic lattice for $\phi = 0$ and measure the RF spectra for $|12\rangle$ atom pair states. Figure. 5.2 shows the measured spectrum at 800.6 G. Here the lattice depths are chosen such that $s_1 = 7.0$ and $s_2 = 16.5$ with phase $\phi = 0$. After the $|1\rangle - |2\rangle$ atom pair mixture is loaded into the bichromatic potential, a 20 ms RF pulse is applied to transfer atoms from initially occupied state $|2\rangle$ to unoccupied state $|3\rangle$. Then the remaining atom number in state $|2\rangle$ is recorded using an absorption image. On the $y-$axis we record the fractional atom loss from state $|2\rangle$, for each input frequecny of the RF pulse (measured realtive to the bare atomic frequency, ν_{32}^0). Figure 5.2 shows peaks corresponding to two resonance frequencies, suggesting the posibility of having two different bound atom pair states $|12\rangle$. This turned out to be an intersting result. To understand where these two peaks are coming from, we go back to our theoretical model, which we discussed in Chapter. 3, and see how we can evaluate the spectrum starting from the energy diagram shown in Fig. 5.3.

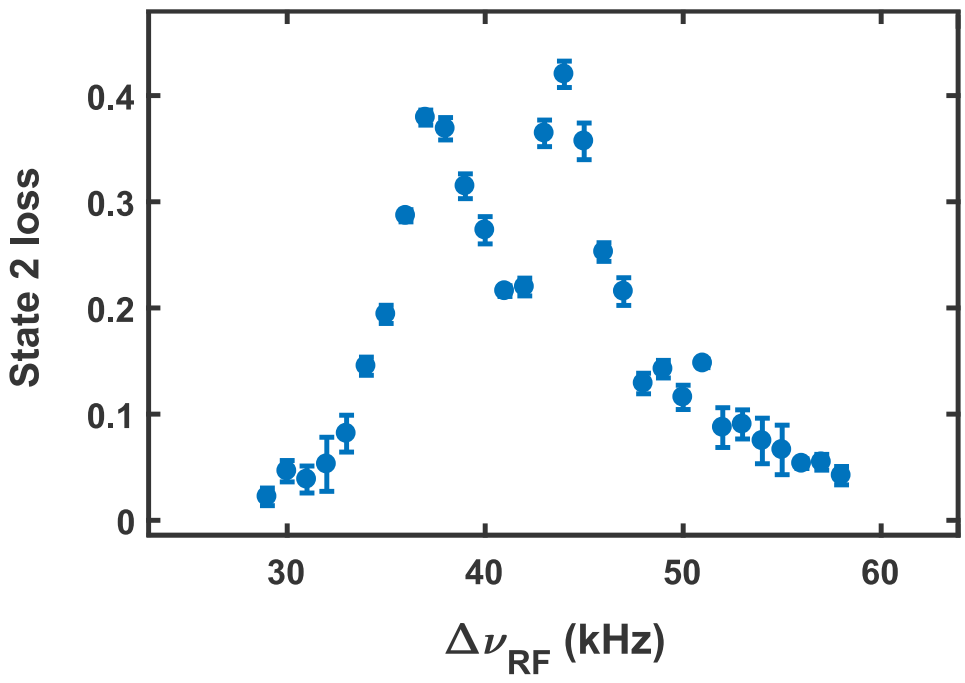

Figure 5.2: Radio-frequency $|12\rangle \rightarrow |13\rangle$ dimer transition spectra (blue dots). Here $s_1 = 7$, $s_2 = 16.5$ and $\phi = 0$. $\Delta\nu_{RF} = \nu_{RF} - \nu_{32}^0$ is the input radio frequency relative to the bare atomic frequency ν_{32}^0. Error bars denote the standard deviation of the mean of 5 runs.

5.2.1 Evaluation of Spectra

Figure. 5.3 shows the two lowest d/a solutions for $\phi = 0$ for a variety of energies E, as green and blue dots at low resolution, and as continuous curves at high resolution (insets). Note that the change in color from left to right is a result of our d/a labeling: For the same E, the smallest (left most) d/a solutions are green, the next larger d/a solutions are blue. For simplicity, we show predictions for $Q = 0$, as the Q-dependence for our lattice parameters is relatively small (Q dependance of the spectra is discussed in Sec. 5.4.1). States A and B are the two bound states of lowest total energy at $B = 800.6$ G with $d/a_{12} = 1.28$, denoted by the vertical solid black line. For symmetric double well potentials with $\phi = 0$ and $Q = 0$, dimer states A and B are delocalized between the right and left wells respectively, as depicted in cartoon on Fig. 5.4(a) and are symmetric or antisymmetric in the CM Z-coordinate relative to the double-well center, as shown by the eigenstates $f_E^Q(Z)$ in Fig. 5.4(b). It is important to notice that the $f_E^Q(Z)$ is not the CM state, as $\Psi_E(\mathbf{r}, Z)$ generally does not factor, entangling the atom pair relative coordinate $\mathbf{r}$ and the CM Z-coordinate. However, as explained in the next paragraph, the Franck-Condon factors for the RF transitions are proportional to the square of the overlap integrals of the $f_E^Q(Z)$ functions for the initial and final states, which provides

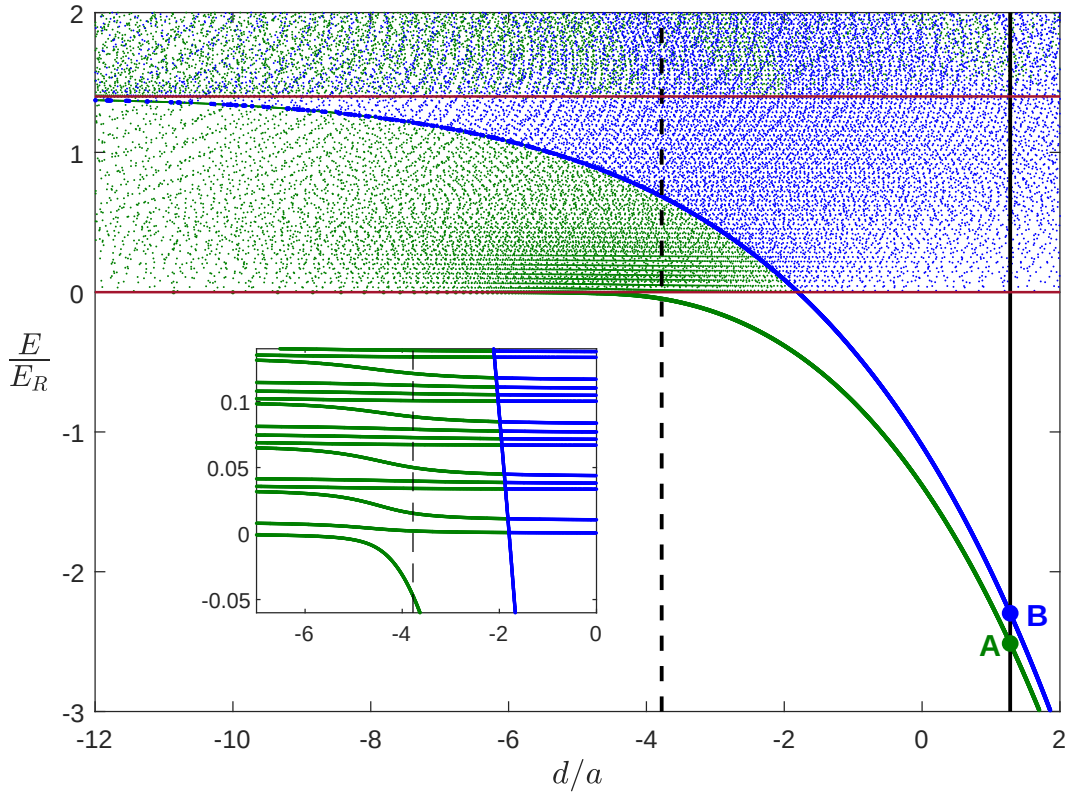

Figure 5.3: Dimer energies E for a lattice of double-well potentials versus d/a for $\phi = 0$. For each E, green and blue denote the two smallest d/a values. A and B show the initially populated $|12\rangle$ dimer states with $d/a_{12} = 1.28$. Crossings with the dashed black line at $d/a_{13} = -3.78$ determine final $|13\rangle$ dimer states. The energy asymptotes, shown as red horizontal lines, denote the lowest energy for two noninteracting atoms in the first band (lower red line) and for one in each of the first two bands (upper red line). Insets show typical structure for states above $E = 0$.

substantial insight. Note that the blue curve starting at B in Fig. 5.3, which arises from odd symmetry dimer states, crosses several nominally horizontal green and blue curves, which arise from even symmetry states.

Experimentally, the applied RF pulse convert a $|12\rangle$ atom pair state in to a $|13\rangle$ atom pair states with $d/a_{13} = -3.78$ (vertical dashed line). Using Fig. 5.3, we identify the set of possible final state energies from the crossings between the energy versus d/a curves (shown in detail in the insets) and the vertical dashed line corresponding to the chosen final d/a_{13} value. As described in Sec. 3.4, the overlap integral of the initial and final states,

$$\langle E_2|E_1\rangle = A_2^* A_1 \frac{2\beta}{\tilde{E}_2 - \tilde{E}_1}\left(\frac{d}{a_1} - \frac{d}{a_2}\right)\sum_G B_G^{E_2 *}(Q) B_G^{E_1}(Q). \tag{5.1}$$

is proportional to the overlap integral of the eigenfunctions $f_E^Q(Z) = \sum_{G'} B_{G'}^E(Q) \frac{e^{i(G'+Q)Z}}{\sqrt{Nd}}$, and the normalization constants of the initial and final states. Hence, the symmetry of the $f_E^Q(Z)$ eigenstates and the localization of the wavefunctions determine the strength of the overlap integrals, and which identified final states can be excited. In this case, a transition from the

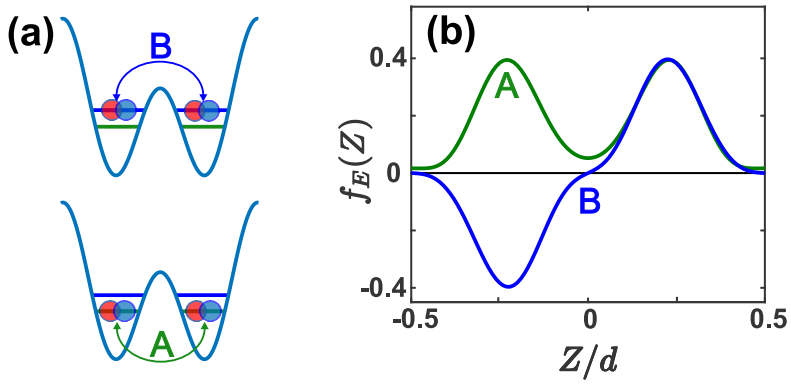

Figure 5.4: (b) Eigenstates $f_E(Z)$ (see eq. 3.55) versus CM coordinate Z are A symmetric or B antisymmetric with respect to the site center. (a) Cartoons depict delocalized symmetric (A) orantisymmetric (B) dimer CM states.

antisymmetric state B to the lowest final state at $E < 0$ and $d/a_{13} = -3.78$ is not allowed, as the two states have opposite symmetry in Z.

Using eq. 5.1, we compute the squared magnitude of the overlap integrals (Franck-Condon factors) for transitions originating from an initial $|12\rangle$ state with a given d/a_{12} value to all final $|13\rangle$ states with a fixed d/a_{13} value. We find that Franck-Condon factors decrease with increasing final state energy and that the sum over final states for each initial state converges to a value near unity. Fig. 5.5(b)(c) shows the final state energy distributions of the Franck-Condon factors for a symmetric lattice with $phi = 0$. For these plots, the vertical position of each horizontal bar corresponds to the energy of a final state. The bar lengths represent the probabilities on a log scale, where only transitions stronger than 10^{-3} are shown. The green bars in panel (b) correspond to transitions from state A of Fig. 5.3, while blue bars in panel (c) correspond to transitions from state B. For $\phi = 0$, transitions from the tightly bound lowest-lying symmetric state A, comprise a moderately strong excitation to the weakly bound, lowest-lying, symmetric final state with $E < 0$ and to a quasi-continuum of symmetric excited bound states with $E > 0$ as shown in Fig. 5.3 (b). The latter corresponds to a threshold spectrum for $\beta \to 0$ [Cheng et al., 2016]. Transitions from the tightly bound antisymmetric state B are dominated by a strong transition to another tightly bound antisymmetric state as shown in Fig. 5.3 (c). The

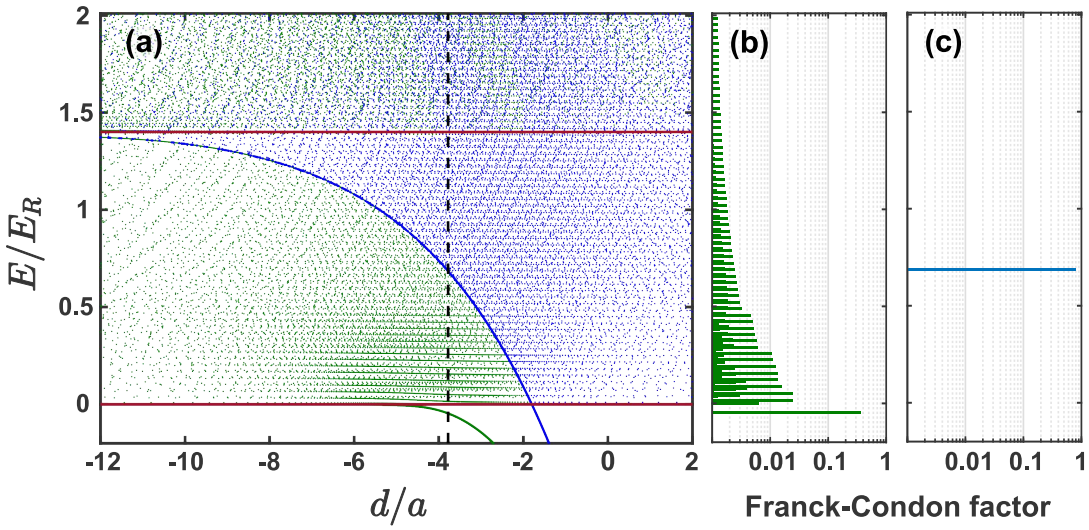

Figure 5.5: (a) Energies of $|13\rangle$ final states for $\phi = 0$ are determined from the crossings of the energy versus d/a curves with the $d/a_{13} = -3.78$ vertical dashed black line. Panels (b) and (c) show the final state energies and corresponding Franck-Condon factors for transitions from the initial states A (green bars) and B (blue bars). Only the final states with Franck-Condon factors larger than 10^{-3} are shown.

binding energy and corresponding localization of the final state for B is larger than that for A, increasing the transition strength. Note that the binding energies are determined with respect to the energy asymptotes, shown as horizontal red lines in Fig. 5.3 and Fig. 5.5(a). Transitions from state B to the quasi-continuum of higher lying excited bound states, above the upper energy asymptote, are weak and negligible for the measured spectrum, as the strong transition comprises most of the transition strength.

We find that the sum of the Franck-Condon factors for transitions from a single initial bound state to all possible final bound states is always close to unity, even for shallow lattices $s_1 = 2.5$ or tight radial confinement, $\beta = 2.0$. We surmise that with finite radial confinement and periodic boundary conditions for a lattice of finite length along z, the bound states are the only relevant solutions, i.e., formally the scattering states consist only of noninteracting states, which are orthogonal to the bound states. Similar behavior arises for simple periodic boundary conditions in a box of length L in one dimension. With an interaction of the form $\alpha\,\delta(z - z_0)$ and $\alpha \neq 0$, the formal bound state solutions obtained by the Green's function method are even in $z - z_0$ and span the space of interacting states, i.e., the solutions obtained for $\alpha = \alpha_1$ can be expanded in terms of the solutions obtained for $\alpha = \alpha_2$. In contrast, solutions which are odd in $z - z_0$ are noninteracting and irrelevant for computing Franck-Condon factors originating from an interacting state.

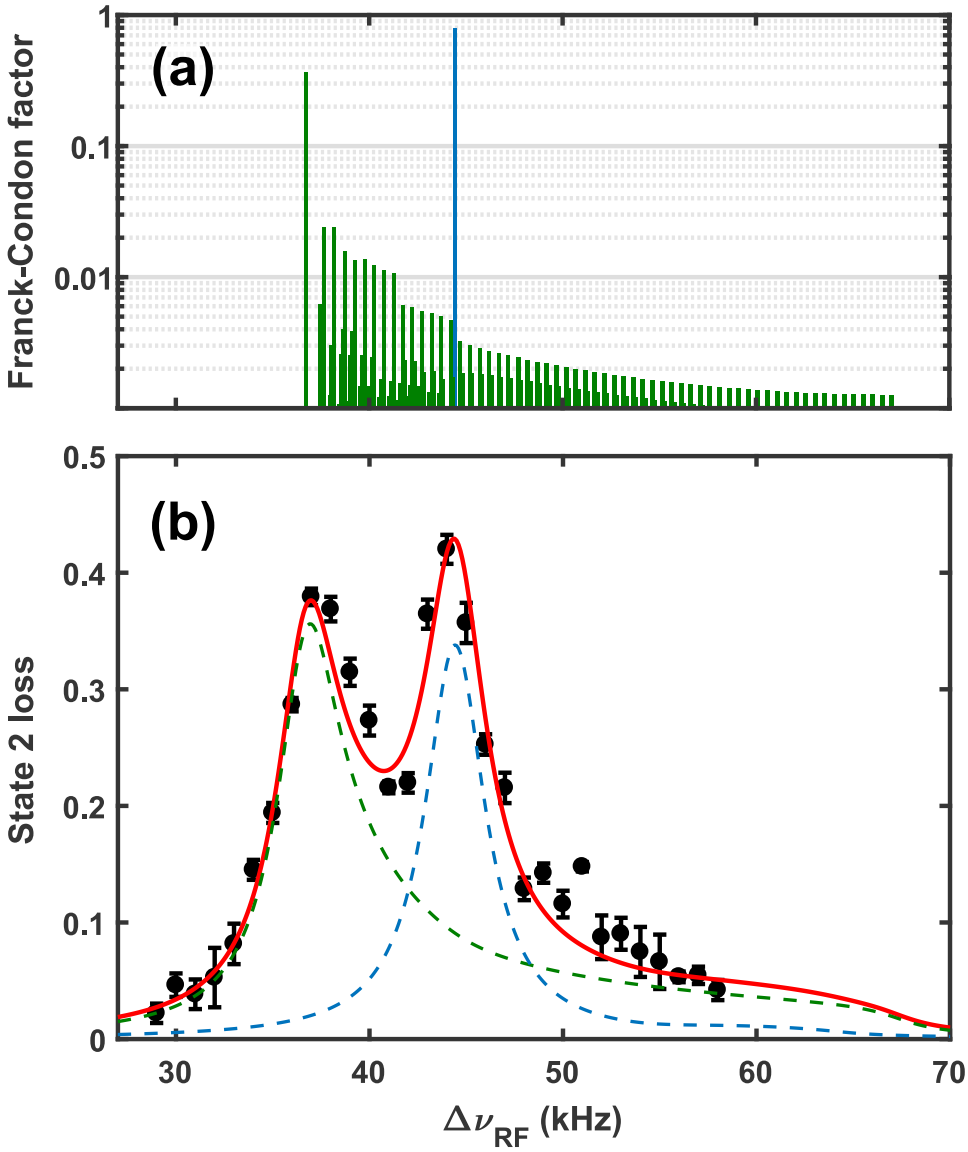

Figure 5.6: (a) Calculated Franck-Condon factors (log scale) for symmetric double-well potentials, $\phi = 0$ as a function of transition frequency. (b) Radio-frequency $|12\rangle \rightarrow |13\rangle$ dimer transition spectra (black dots) versus predictions (red curves). Green and blue denote contributions from states A and B of Fig. 5.3. Error bars denote the standard deviation of the mean of 5 runs.

To predict the measured spectra, we add the contributions from all of the transitions, assuming Lorentzian lineshapes with the same width, weighted by the calculated Frank-Condon factors and centered on the resonance frequencies corresponding to the energy differences. For

transitions originating in dimer state i = A or B, we compute the normalized spectrum,

$$S_i(\nu) = \frac{1}{\pi} \sum_f \frac{\gamma \, |\langle f|i\rangle|^2}{[\nu - (E_f - E_i)/h]^2 + \gamma^2}, \tag{5.2}$$

where ν is the radio frequency relative to the resonance frequency of the bare atom $2 \rightarrow 3$ transition. As mentioned in Sec. 4.7, γ denotes the spectral linewidth (HWHM) $\simeq$ 1.8 kHz, which is small compared to $(E_f - E_i)/h$. For our spectral resolution, with a Lorentzian halfwidth of 1.8 kHz, we find that increasing the number of bands from 9 to 17 and the number of sites from 20 to 40 makes a negligible change in the predicted spectra.

Figure. 5.6(a) shows the Franck-Condon factors $|\langle f|i\rangle|^2$ versus transition frequency, for transitions from the initial bound states i = A,B of Fig. 5.3 to final bound states f with a fixed value of $d/a_{13} = -3.78$. As can be seen in Fig. 5.3(a), for $\phi = 0$ transitions from the tightly bound symmetric state A (green), comprise a dominant excitation to the lowest-lying, most tightly bound, symmetric state (left peak) and to a weaker quasi-continuum of excited bound states. The transitions from the tightly bound antisymmetric state B are dominated by a single excitation to the lowest-lying, most tightly bound, antisymmetric state (blue peak).

As we expect the initial states to be thermally populated for the conditions of our experiment, we take the total spectrum to be proportional to $S(\nu) \propto \exp[-E_A/k_BT]\, S_A(\nu) + \exp[-E_B/k_BT]\, S_B(\nu)$. Here $S_A(\nu)$ and $S_B(\nu)$ are the individual spectra originating from transitions from intial state A and B (denoted in green and blue dashed lines in Fig. 5.6(b)). The red curves show the fits with $k_BT = 0.35\, E_R$. From the very good agreement between our model and the data, we conclude that for $\phi = 0$, the spectra arise from two initially populated dimer states (for each Q), denoted i =A, B in Figs. 5.3.

5.3 Measured RF Spectra for an Asymmetric Double Well Potential

It is interesting to see how the spectrum changes as the relative phase between the lattices is varied slightly, tilting the double well potential. Experimentally, we notices that even a slight change in relative phase ϕ introduces a drastic difference in the measured RF spectrum compared to $\phi = 0$ case. So as the next step of the experiment, we change the phase ϕ from $\phi = 0$ to $\phi = \pi/35$, keeping the lattice depths to be the same, $s_1 = 7$ and $s_2 = 16.5$. We notice that any change in the phase which is less than $\phi = \pi/35$ makes no measurable difference in the observed spectrum.

Before we see the effect on the measured spectrum, I'd like focus the reader's attention on the calculated dimer energy diagram given in Fig. 5.7 for the $\phi = \pi/35$ case. Notice now the

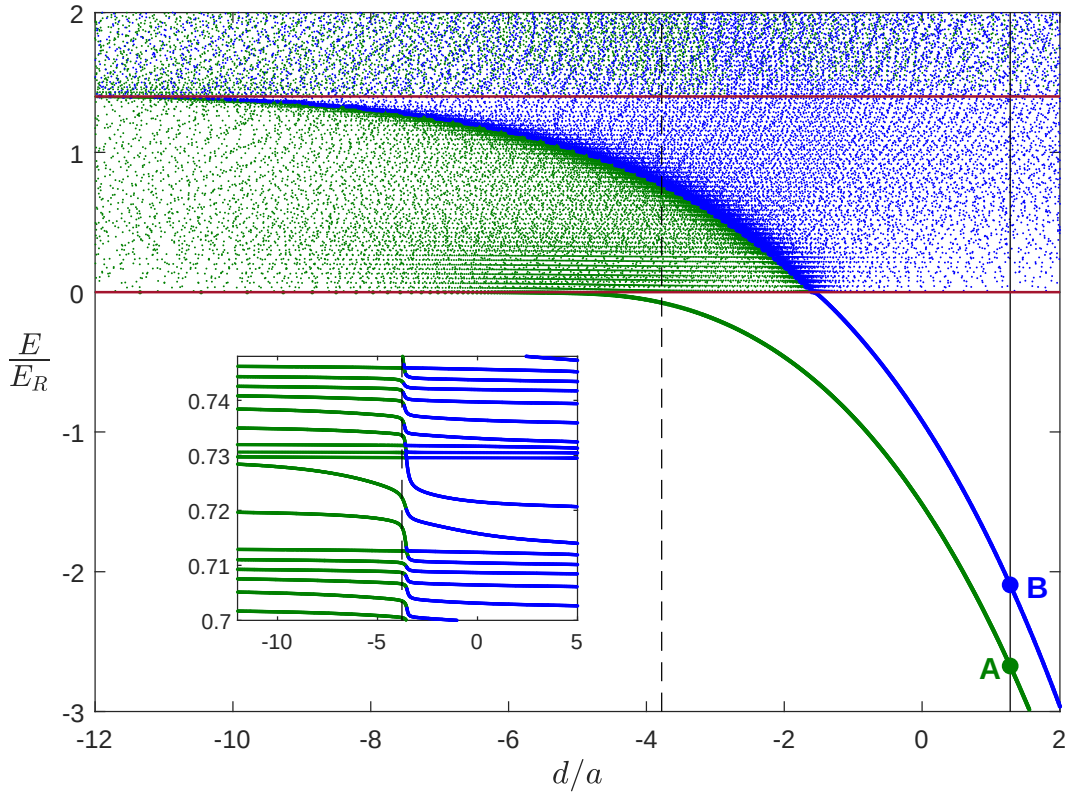

Figure 5.7: Dimer energies E for a lattice of tilted double-well potentials versus d/a for $\phi = \pi/35$. For each E, green and blue denote the two smallest d/a values. A and B show the initially populated $|12\rangle$ dimer states with $d/a_{12} = 1.28$. Crossings with the dashed black line at $d/a_{13} = -3.78$ determine final $|13\rangle$ dimer states. The energy asymptotes, shown as red horizontal lines, denote the lowest energy for two noninteracting atoms in the first band (lower red line) and for one in each of the first two bands (upper red line). Insets show typical structure for states above $E = 0$.

second d/a solution (denoted in blue) has become fuzzy in the region of $E > 0$ as opposed to the $\phi = 0$ case. A closer (see inset) tells us what appeared to be a crossing of the second d/a solution through horizontal lines of the first d/a solution for $E > 0$, now appears as an avoided crossing as it passes through this region (see inset of Fig. 5.7).

To understand the meaning of this behavior, let us turn our attention towards the $f_E^Q(Z)$ functions. Figure. 5.8(b) shows the eigenstates $f_E^Q(Z)$ for dimer state A and B in Fig. 5.7. For tilted double well potentials with $\phi = \pi/35$, we see that the states A and B are localized in the right or left well, breaking initial symmetry that was present for $\phi = 0$ in Fig. 5.4(b) and strongly mixing the two lowest lattice states, which have opposite symmetry. For $E > 0$, this mixing changes the crossings of the blue curve in Fig. 5.3(inset) to avoided crossings in Fig. 5.7(inset), blurring the energy diagram. The tilt in the double well potential also increases

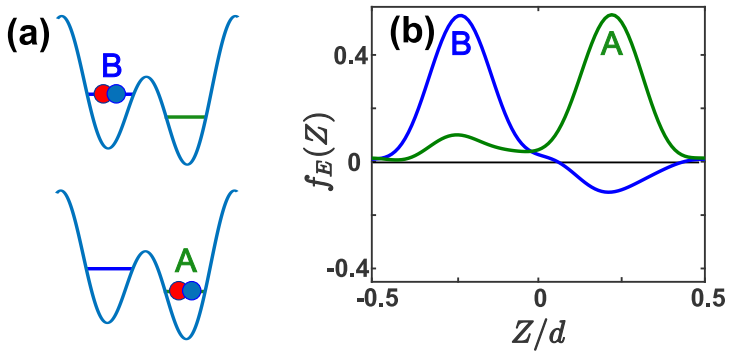

Figure 5.8: (a) Cartoons depict localized right (A) or left (B) dimer states. (b) Eigenstates $f_E(Z)$ (see eq. 3.55) versus CM coordinate Z are A symmetric or B antisymmetric with respect to the site center. .

the A-B energy separation compared to Fig. 5.3. When we evaluate the spectra using this energy diagram as we did before for the $\phi = 0$ case, we notice that this mixing of left- and right-well localized states increases the number of possible final states for transitions from state B. For example, the lowest final state at $E < 0$ acquires a non-zero overlap with the initial state B, as well as with state A, as shown in Fig. 5.9 (b) and (c). Similarly, as seen in Fig. 5.9(c), more

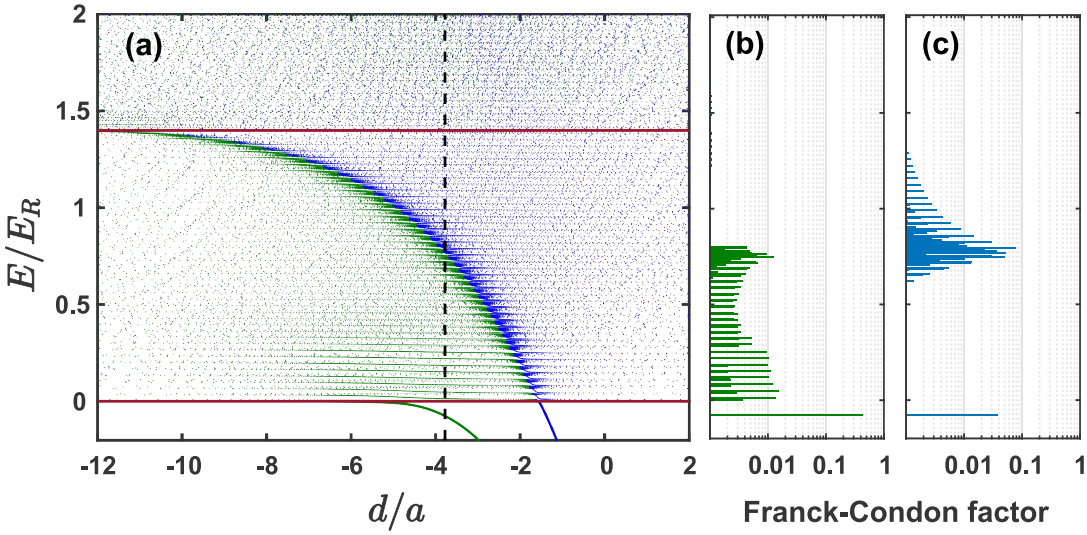

Figure 5.9: (a) Energies of $|13\rangle$ final states for $\phi = 0$ are determined from the crossings of the energy versus d/a curves with the $d/a_{13} = -3.78$ vertical dashed black line. Panels (b) and (c) show the final state energies and corresponding Franck-Condon factors for transitions from the initial states A (green bars) and B (blue bars). Only the final states with Franck-Condon factors larger than 10^{-3} are shown.

final states contribute around the fuzzy border line between green and blue domains of Fig. 5.9 (a), in contrast to the $\phi = 0$ case, Fig. 5.5(c) where all final states except one are orthogonal to the initial state B. For transitions from the right-well state A, Fig. 5.9(b), the strengths decrease quickly with increasing energy as the border line is crossed toward the blue domain,

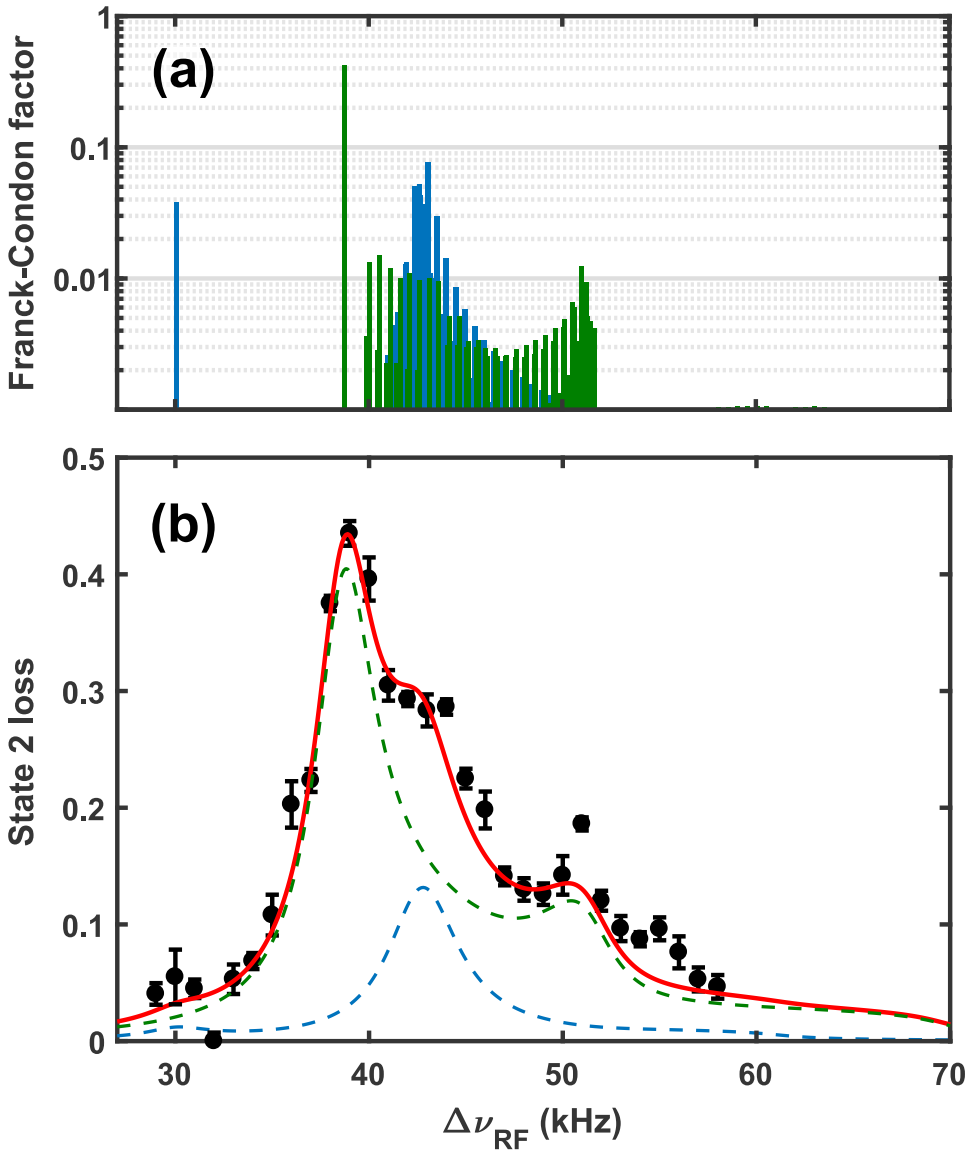

Figure 5.10: Bottom: Radio-frequency $|12\rangle \rightarrow |13\rangle$ dimer transition spectra (black dots) versus predictions (red curves). Green and blue denote contributions from states A and B of Fig. 5.7. Top: Calculated Franck-Condon factors (log scale) for symmetric double-well potentials, $\phi = 0$ as a function of transition frequency. Error bars denote the standard deviation of the mean of 5 runs.

because the final states become more left-well localized at higher energy. For transitions from the left-well state B, Fig. 5.9 (c), the strengths increase in the vicinity of the border line as the final states become more left-well localized and decrease further into the blue domain due to radial delocalization of the final states.

Observed RF spectrum is shown in Fig. 5.10(b) compaired to the theory (red curve). Note that the red curve shows the fits with $k_B T = 0.43\, E_R$, as opposed to $0.35\, E_R$ which was used for $\phi = 0$ case. However, an extended calculation given in Sec. 5.4.1, using a Boltzmann factor weighted sum over all Q, yields equally good fits, but with the same temperature, $k_B T = 0.48\, E_R \simeq k_B \times 0.34\, \mu$K, for both $\phi = 0$ and $\phi = \pi/35$. As pointed out above, the mixing of left- and right-well localized states increases the number of transitions from state B, blurring the spectrum near 40 kHz. Further, the lowest final state at $E < 0$ acquires a non-zero overlap with the initial state B, as shown by the blue peak at 30 kHz in Fig. 5.10(a). For transitions from the right-well state A, the strengths decrease quickly above 52 kHz, as the corresponding final states become more left-well localized with increasing energy above the fuzzy green-blue curve in Fig. 5.7.

5.4 Tuning from a Double Well to a Single Well Potential

Fig. 5.11 compares the spectra measured at $B = 800.6$ G to the theoretical model for lattice depths $s_1 = 7.0$ and $s_2 = 16.5$ for three different phase. As one would expect, the continuous

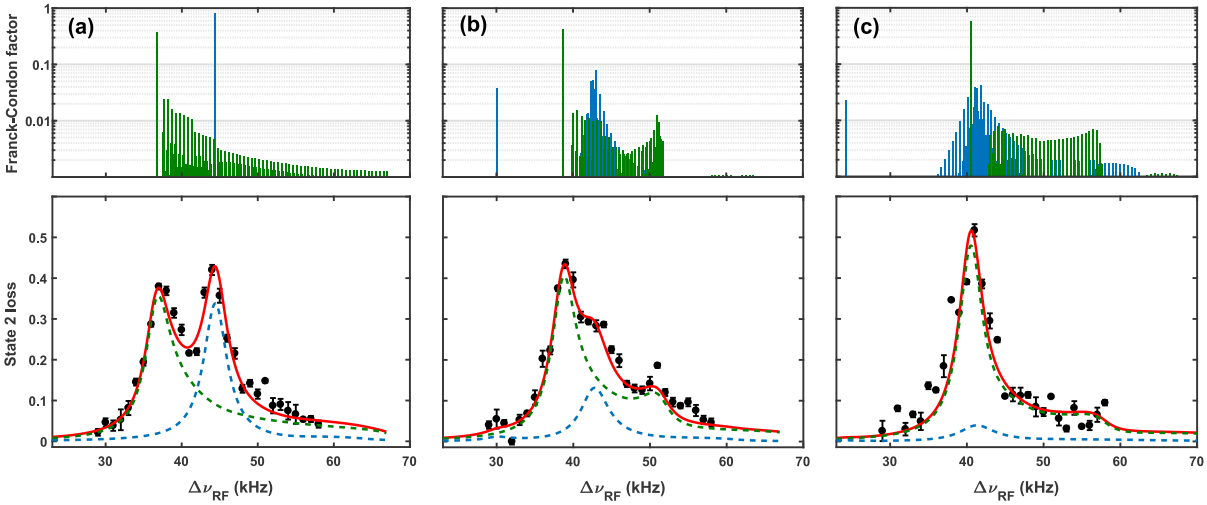

Figure 5.11: Radio-frequency $|12\rangle \rightarrow |13\rangle$ dimer transition spectra (black dots) versus predictions (red curves) for $B = 800.6$ G, $s_1 = 7$, $s_2 = 16.5$. Calculated Franck-Condon factors (log scale) versus transition frequency and spectrum for (a) $\phi = 0$; (b) $\phi = \pi/35$; (c) $\phi = 2\pi/35$. Error bars denote the standard deviation of the mean of 5 runs.

change in phase eventually turns the double well potential in to a single potential well, ultimately supporting only one populated bound state. Notice that the height of the peak correspond to the transition originating from the upper atom pair state B in Fig. 5.3, gradually decreases in height with the increasing phase. As the potential wells are tilted more and more in Fig. 5.8(a), it is clear that the energy gap between dimer state A and B increases resulting a reduce population of atom pairs in state B (compare the energy gap between state A and B in Figures 5.3 and 5.7). As can be seen in Fig. 5.11(c) the strength of Franck-Condon factors is reduced only slightly compared to $\phi = 0$ case. However, the increasing gap between the initial atom pair state A and B results in a decreased population in atom pairs in state B, making its contribution less and less in the spectrum of Fig. 5.11(c) (see blue dashed line).

5.4.1 Q-dependence of the Spectra

As discussed in Chap. 3, the total quasi-momentum of an atom pair $Q = q_1 + q_2$. So far, I've only considered the spectra evaluated for $Q = 0$ case. For completeness, here we consider the contribution of different Q-components to the overall spectrum. First, for each of 20 Q-values equally spaced in steps of 0.2 from -2.0 to +1.8 (one full period of the total quasi-momentum), we compute a corresponding spectrum in the same way as described above for the $Q = 0$ case. Then, we weight each spectrum using a Boltzmann factor with the total energy of the

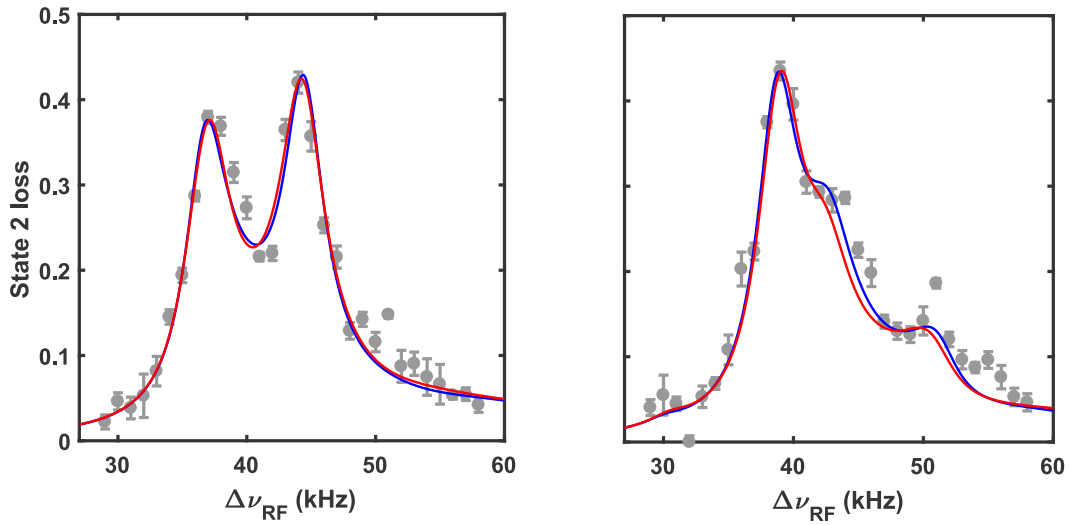

Figure 5.12: Spectra for $B = 800.6$ G calculated for $Q = 0$ only (blue) versus spectra for Boltzmann-factor-weighted sum over Q (red) compared to data (gray dots). (a) $\phi = 0$; (b) $\phi = \pi/35$.

corresponding Q-component given by eq. 3.54 and referenced to the lowest total energy, i.e., that of two atoms in the ground band with $Q = 0$, defined as $E = 0$ above. Finally, we sum all of the spectral components and fit the result to the data using two parameters, the overall amplitude and a Boltzmann temperature $k_B T$. Fig. 5.12 compares the fits to the data for $s_1 = 7.0$ and $s_2 = 16.5$ using only the $Q = 0$ component (blue) with the fit including all of the Q components (red). With all of the Q components included, we find that a single temperature $k_B T = 0.48 E_R = k_B \times 0.34\,\mu K$ fits both the $\phi = 0$ and $\phi = \pi/35$ data, in contrast to the $Q = 0$ fits, where two different temperatures are required.

Chapter 6

Conclusion

6.1 Summary of the Dissertation

This dissertation primarily contains of two pieces of work. First, I described the detailed derivation of a multi-band model to evaluate two-atom pairing energies and states in a 1D optical superlattice potential with finite radial confinement. The theoretical model is implemented by extending the rigorous Green's function method of Orso et al., [Orso et al., 2005] for a 1D bichromatic lattice with non-zero radial confinement. Next, I provided the quantitative measurements of radio-frequency spectra of atom pair states in a 1D bichromatic optical superlattice that creates a series of double-well potentials, revealing the co-existance of two types of pairing states with different symmetries. I find that the described multi-band model is in excellent agreement with our observed spectral structure for different symmeteries of the double-well potential providing the first understanding of how elementary two-body pairng works in 1D optical superlattices. We believe that this model can be used to test the validity of analytic approximations and to characterize the states and populations of atom pairs in general optical lattices, providing a foundation for new experiments with strongly interacting fermions.

6.2 Outook

As mentioned in Chapter. 1, with magnetically tunable two-body interactions and wide control of the dispersion relation, we believe that ultracold atomic gases in superlattices provides a broad platform for studies of many-body physics, including entanglement, nonequilibrium dynamics, and exotic new states of matter. This includes studies of new superfluids and new models of quantum magnetism with interactions, where the left-right atom pair states of the asymmetric double-well potential serve as a two state effective spin half system as described in ref [Li et al., 2016]. Also, cyclic variation of the phase and corresponding double-well symmetry

has been used to observe topological (Thouless) pumping for weakly interacting systems [Lohse et al., 2016,Nakajima et al., 2016], where as our system enables exploring these dynamic in the strongly interacting regime. However, it is important for us to be able to dynamically vary the relative phase between the two lattices.

So as the next step of our experiment, an electro optic modulator will be added to the Babinet path in Fig. 4.1 enabling the dynamic control of the phase. Note that by shifting the

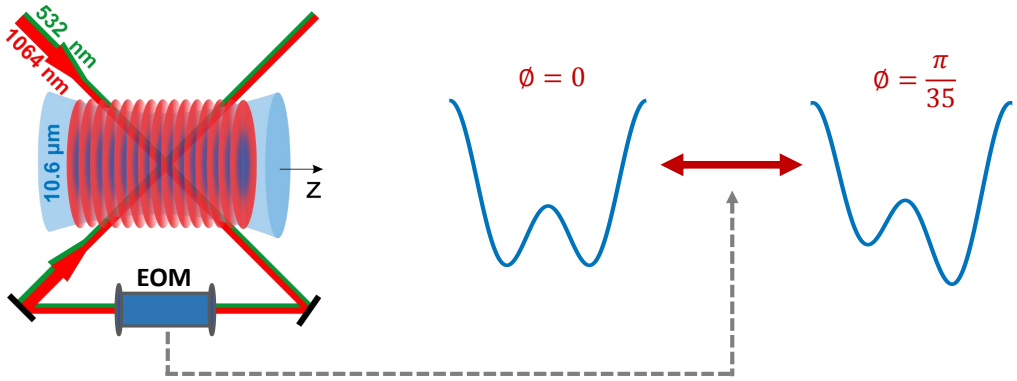

Figure 6.1: Added Electro-optic modulator(EOM) allows the dynamical variation of the relaitve phase ϕ. Phase can be changed from symmetric dpuble-well to an asymmetric double-well potential by changing the voltage applied to the EOM.

relative energy of the left or right states or by shifting the wells from symmetric to left-right symmetry one can rapidly change the types of atom pairs that can exist, allowing the studies of non-equilibrium dynamics of the system. Also, combined control of lattice intesity and phase enables the real-time control of the dispersion of atoms and may lead to dynamical control of Dirac points of the system.

REFERENCES

[Bartenstein et al., 2005] Bartenstein, M., Altmeyer, A., Riedl, S., Geursen, R., Jochim, S., Chin, C., Denschlag, J. H., Grimm, R., Simoni, A., Tiesinga, E., Williams, C. J., and Julienne, P. S. (2005). Precise Determination of 6Li Cold Collision Parameters by Radio-Frequency Spectroscopy on Weakly Bound Molecules. *Phys. Rev. Lett.*, 94(10):103201.

[Bloch et al., 2008] Bloch, I., Dalibard, J., and Zwerger, W. (2008). Many-body physics with ultracold gases. *Rev. Mod. Phys.*, 80(3):885–964.

[Butov et al., 2002] Butov, L. V., Gossard, A. C., and Chemla, D. S. (2002). Macroscopically ordered state in an exciton system. *Nature*, 418(6899):751–754.

[Cheng, 2016] Cheng, C. (2016). *Ultracold Fermi Gases in a Bichromatic Optical Superlattice*. PhD thesis, Duke University.

[Cheng et al., 2016] Cheng, C., Kangara, J., Arakelyan, I., and Thomas, J. E. (2016). Fermi gases in the two-dimensional to quasi-two-dimensional crossover. *Phys. Rev. A*, 94(3):031606.

[Huang, 1987] Huang, K. (1987). *Statistical Mechanics, 2nd Edition*.

[Idziaszek and Calarco, 2006] Idziaszek, Z. and Calarco, T. (2006). Analytical solutions for the dynamics of two trapped interacting ultracold atoms. *Phys. Rev. A*, 74(2):022712.

[Jo et al., 2012] Jo, G.-B., Guzman, J., Thomas, C. K., Hosur, P., Vishwanath, A., and Stamper-Kurn, D. M. (2012). Ultracold Atoms in a Tunable Optical Kagome Lattice. *Phys. Rev. Lett.*, 108(4):045305.

[Kanász-Nagy et al., 2015] Kanász-Nagy, M., Demler, E. A., and Zaránd, G. (2015). Confinement-induced interlayer molecules: A route to strong interatomic interactions. *Phys. Rev. A*, 91(3):032704.

[Li et al., 2016] Li, J., Huang, W., Shteynas, B., Burchesky, S., Top, F. Ç., Su, E., Lee, J., Jamison, A. O., and Ketterle, W. (2016). Spin-Orbit Coupling and Spin Textures in Optical Superlattices. *Phys. Rev. Lett.*, 117(18):185301.

[Lohse et al., 2016] Lohse, M., Schweizer, C., Zilberberg, O., Aidelsburger, M., and Bloch, I. (2016). A Thouless quantum pump with ultracold bosonic atoms in an optical superlattice. *Nat. Phys.*, 12(4):350–354.

[Mayorov et al., 2011] Mayorov, A. S., Elias, D. C., Mucha-Kruczynski, M., Gorbachev, R. V., Tudorovskiy, T., Zhukov, A., Morozov, S. V., Katsnelson, M. I., Geim, A. K., and Novoselov, K. S. (2011). Interaction-Driven Spectrum Reconstruction in Bilayer Graphene. *Science (80-.).*, 333(6044):860–863.

[Nakajima et al., 2016] Nakajima, S., Tomita, T., Taie, S., Ichinose, T., Ozawa, H., Wang, L., Troyer, M., and Takahashi, Y. (2016). Topological Thouless pumping of ultracold fermions. *Nat. Phys.*, 12(4):296–300.

[O'Hara, 2002] O'Hara, K. M. (2002). Observation of a Strongly Interacting Degenerate Fermi Gas of Atoms. *Science (80-.).*, 298(5601):2179–2182.

[Orso et al., 2005] Orso, G., Pitaevskii, L. P., Stringari, S., and Wouters, M. (2005). Formation of Molecules near a Feshbach Resonance in a 1D Optical Lattice. *Phys. Rev. Lett.*, 95:60402.

[Pertot et al., 2014] Pertot, D., Sheikhan, A., Cocchi, E., Miller, L. A., Bohn, J. E., Koschorreck, M., Köhl, M., and Kollath, C. (2014). Relaxation Dynamics of a Fermi Gas in an Optical Superlattice. *Phys. Rev. Lett.*, 113(17):170403.

[Salger et al., 2011] Salger, T., Grossert, C., Kling, S., and Weitz, M. (2011). Klein Tunneling of a Quasirelativistic Bose-Einstein Condensate in an Optical Lattice. *Phys. Rev. Lett.*, 107(24):240401.

[Seamons et al., 2009] Seamons, J. A., Morath, C. P., Reno, J. L., and Lilly, M. P. (2009). Coulomb Drag in the Exciton Regime in Electron-Hole Bilayers. *Phys. Rev. Lett.*, 102(2):026804.

[Sommer et al., 2012] Sommer, A. T., Cheuk, L. W., Ku, M. J. H., Bakr, W. S., and Zwierlein, M. W. (2012). Evolution of Fermion Pairing from Three to Two Dimensions. *Phys. Rev. Lett.*, 108(4):045302.

[Velasco et al., 2012] Velasco, J., Jing, L., Bao, W., Lee, Y., Kratz, P., Aji, V., Bockrath, M., Lau, C. N., Varma, C., Stillwell, R., Smirnov, D., Zhang, F., Jung, J., and MacDonald, A. H. (2012). Transport spectroscopy of symmetry-broken insulating states in bilayer graphene. *Nat. Nanotechnol.*, 7(3):156–160.

[Weitz et al., 2010] Weitz, R. T., Allen, M. T., Feldman, B. E., Martin, J., and Yacoby, A. (2010). Broken-Symmetry States in Doubly Gated Suspended Bilayer Graphene. *Science (80-.).*, 330(6005):812–816.

[Witthaut et al., 2011] Witthaut, D., Salger, T., Kling, S., Grossert, C., and Weitz, M. (2011). Effective Dirac dynamics of ultracold atoms in bichromatic optical lattices. *Phys. Rev. A*, 84(3):033601.

[Zhang et al., 2012] Zhang, Y., Ong, W., Arakelyan, I., and Thomas, J. E. (2012). Polaron-to-Polaron Transitions in the Radio-Frequency Spectrum of a Quasi-Two-Dimensional Fermi Gas. *Phys. Rev. Lett.*, 108(23):235302.

[Zürn et al., 2013] Zürn, G., Lompe, T., Wenz, A. N., Jochim, S., Julienne, P. S., and Hutson, J. M. (2013). Precise Characterization of 6Li Feshbach Resonances Using Trap-Sideband-Resolved RF Spectroscopy of Weakly Bound Molecules. *Phys. Rev. Lett.*, 110(13):135301.

APPENDIX

Appendix A

Matlab Program for Evaluating the Eigenstates and Energies in a Bichromatic Superlattice.

A.1 Evaluating Single Particle Band Energies

Following MATLAB code is used to evaluate the energy eigenvalues and eigenvectors of a single atom in a bichromatic lattice potential. Function Inputs are:

- M = number of bands used for the calculation (ex: for 9 band model, N=9)
- N = number of lattice sites used for the calculation (ex: to use 20 sites, M=20)
- Q = total quasi-momentum of the atom pair ($Q = q_1 + q_2$)
- phi = relative phase between the two lattices given in radians
- s1 = red lattice depth in units of E_R
- s2 = greened lattice depth in units of E_R

The function Outputs a structure containing the energy eigenvalues for atom1 and atom2 saved with field names as E1 and E2. Eigenvectors are saved under the field names Evect1 and Evect2.

```
function MB=LatticeBandsWithQ_SymV(s1,s2,phi,M,N,Q)
v1=-s1/4;
v2=s2/4;

q=(-N/2:1:N/2)*2/N;% in units of k
```

```
6
7  q1=Q/2+q;
8  q2=Q/2-q;
9
10 G1=-(M-1):2:(M-1); % in units of k
11
12 H=zeros(M);
13 MB.q1=q1;
14 MB.q2=q2;
15 MB.q=q;
16 MB.Q=Q;
17 MB.sites=N;
18 MB.s1=s1;
19 MB.s2=s2;
20 MB.phi=phi;
21 MB.bands=M;
22
23 for q1_j=1:numel(q1)
24     H(1:M+1:end)= ( q1(q1_j) + G1 ).^2;
25     H(2:M+1:(M-1)*(M+1)+1)= v1;
26     H(3:M+1:(M-2)*(M+1)+2)= v2*exp(1i*phi);
27     H(M+1:M+1:(end-1))= v1;
28     H(2*M+1:M+1:(end-2))= v2*exp(-1i*phi);
29
30     MB.Hamil1{q1_j}=H;
31     %[MB.Evect1{q1_j},Eval]=eig(H);
32     [Coeff,Value]=eig(H);
33     [sorted_Value,I]=sort(real(diag(Value)));
34     MB.E1(q1_j,:)=sorted_Value;
35     MB.Evect1{q1_j}=Coeff(:,I);
36
37 end
38
39 for q2_j=1:numel(q2)
40     H(1:M+1:end)= ( q2(q2_j) + G1 ).^2;
41     H(2:M+1:(M-1)*(M+1)+1)= v1;
42     H(3:M+1:(M-2)*(M+1)+2)= v2*exp(1i*phi);
```

```
43        H(M+1:M+1:(end-1))= v1;
44        H(2*M+1:M+1:(end-2))= v2*exp(-1i*phi);
45
46        MB.Hamil2{q2_j}=H;
47        [Coeff,Value]=eig(H);
48        [sorted_Value,I]=sort(real(diag(Value)));
49        MB.E2(q2_j,:)=sorted_Value;
50        MB.Evect2{q2_j}=Coeff(:,I);
51    end
52
53
54  % figure;plot(MB.q1,MB.E1,'o');
55  % figure;plot(MB.q1,MB.E(:,1),MB.q1,MB.E(:,2));
56  % ylim([0  2]);
57
58  end
```

A.2 Evaluating Two Particle Energies

Follwing MATLAB code is used to diagonalize $M_{GG'}(E,Q)$ (seeEq. 3.53). Note for each value of input energy Eb, N number of d/a eigenvalue solutions are evaluted by the function. Function Inputs are:

- MB = structure containing single particle eigenvalues and eigenvectors for atom1 and atom2 (Output given by the Code. A.1)
- bta = β in units of E_R
- d_over_a_ref = $\left(\frac{d}{a}\right)_{ref}$ (see Code.**??**)
- Eb_ref = ϵ_b^{ref}
- Eb = Energy of the atom pair state in units of E_R

The function Output is a MATLAB strucure containing the energy eigenvalues and eigenvectors of matrix $M_{GG'}(E,Q)$.

```
1  function y=LatticeBindingV24_SymV(MB,bta,Eb_ref,d_over_a_ref,Eb)
2  % matrix version,q1 is not symmetrized in this version but q2 is
       introduced,
```

```
% q1 sum is done on the range N/2<q<N/2-1
N=MB.sites;
q1=MB.q1;% in units of k
q2=MB.q2;% in units of k
q=MB.q;
M=MB.bands;
Q=MB.Q;

G1=-(M-1):2:(M-1); % in units of k
G1p=-(M-1):2:(M-1); % in units of k

G=-(M-1):2:(M-1); % in units of k
Gp=-(M-1):2:(M-1); % in units of k

M1_GGp=zeros(M);
M0_GGp=zeros(M);
M00_GGp=zeros(M);

Etot=MB.E1(q1==Q/2,1)+MB.E2(q2==Q/2,1)-Eb;

Eigen.Eb=Eb;
Eigen.Q=Q;
Eigen.bta=bta;
Eigen.Ebref=d_over_a_ref;
Eigen.dovera_ref=Eb_ref;


for G_i=1:1:M
    G1_i=restrictG(G1,G(G_i));

    for Gp_i=G_i:1:M
        G1p_i=restrictG(G1p,Gp(Gp_i));
        G1G1p_alpha2_alpha1_sum=zeros(1,(numel(q)-1)/2+1);

        for q_j=1:(numel(q)-1)/2+1

            Cq1=MB.Evect1{1,q_j};
```

```
40              Cq2=MB.Evect2{1,q_j};
41
42              Cq1_new=Cq1(G1_i,:);
43              Cq2_new=Cq2(G1_i,:);
44              Cq2_new=fliplr(Cq2_new.').';
45              G1_sum=Cq1_new.'*Cq2_new;
46
47              Cq1_new=Cq1(G1p_i,:);
48              Cq2_new=Cq2(G1p_i,:);
49              Cq2_new=fliplr(Cq2_new.').';
50              G1p_sum=conj(Cq1_new.')*conj(Cq2_new);
51
52              G1G1p_sum=G1_sum.*G1p_sum;
53
54              poly_arg=(MB.E1(q_j,:).' + MB.E2(q_j,:) - Etot)/2/bta;
55              sz=size(poly_arg);
56              poly_arg_pos=poly_arg>0;
57              poly_arg_neg=poly_arg<0;
58              poly_arg_zero=poly_arg==0;
59              poly_zero=zeros(sz(1));
60
61              polygamma_pos=psi(poly_arg.*poly_arg_pos);
62              polygamma_pos(polygamma_pos==-Inf)=0;
63
64              polygamma_neg=psi(1-poly_arg.*poly_arg_neg)-pi*cot(pi*
                    poly_arg.*poly_arg_neg);
65              polygamma_neg(polygamma_neg==-Inf)=0;
66
67              poly_zero(poly_arg_zero==1)=-Inf;
68
69              polygamma=polygamma_pos+polygamma_neg+poly_zero;
70
71              G1G1p_alpha2_alpha1_sum(q_j)=sum(sum(G1G1p_sum.*
                    polygamma));
72          end
73          M1_GGp(G_i,Gp_i)=(1/(N))*(2*sum(G1G1p_alpha2_alpha1_sum(2:
                end-1)) + G1G1p_alpha2_alpha1_sum(end) +
```

```
                G1G1p_alpha2_alpha1_sum(1));
74          M1_GGp(Gp_i,G_i)=conj(M1_GGp(G_i,Gp_i));
75
76      end
77      E0=((G(G_i)+Q).^2)/2 - Eb_ref;
78  %       E0=-Eb;%to check for zero lattice  M1_GGp = M0_GGp
79      M0_GGp(G_i,G_i)=(1/(N))*sum( sum( psi( ( (Q/2 + q(1:end-1)+G1(
            G1_i).').^2 + (Q/2-q(1:end-1)-G1(G1_i).'+G(G_i)).^2 - E0 )/2/
            bta ) ) );
80
81  end
82
83  M00_GGp(1:M+1:end)=d_over_a_ref;
84
85  M_GGp=M1_GGp-M0_GGp+M00_GGp;
86
87  [Coeff,Value]=eig(M_GGp);
88  [sorted_Value,I]=sort(real(diag(Value)));
89  Eigen.Value=sorted_Value;
90  Eigen.Coeff=Coeff(:,I);
91
92  y=Eigen;
93
94
95  function y1=restrictG(G1,Gith)
96      G2=Gith-G1;
97      G1_notallowed= G2>max(G1);
98      G1_restr=G1;
99      G1_restr(G1_notallowed)=[];
100     G1_notallowed= G2<min(G1);
101     G1_restr(G1_notallowed)=[];
102
103     b1=find(G1==min(G1_restr));
104     e1=find(G1==max(G1_restr));
105
106     G1_i=b1:1:e1;
107
```

```
y1=G1_i;
```

A.3 Evaluating $\left(\frac{d}{a}\right)_{ref}$

The function evaluates $\left(\frac{d}{a}\right)_{ref}$ according to Eq.3.50 for any input energy Eb given in units of E_R

```
function d_over_a=calculate_dovera(Eb)
fun=@(v,C)(1-(2*v).*exp(-C*v)./(1-exp(-2*v)))./sqrt(4*pi*v.^3);
% vp=0:0.1:1e4;
% fun(1e-7,2)
% figure;plot(vp,fun(vp,1));
% d_over_a=integral(@(v)fun(v,Eb),1e-7,1e4);
d_over_a=integral(@(v)fun(v,Eb),1e-7,1e4);
```